UNIVERSITY OF CALIFORNIA SAN DIEGO

SAN DIEGO STATE UNIVERSITY

Application-Oriented Coil Design in Wireless Charging Systems

A dissertation submitted in partial satisfaction of the
requirements for the degree
Doctor of Philosophy

In

Engineering Science (Electrical and Computer Engineering)

by

Tianze Kan

Committee in charge:

University of California San Diego
- Professor Patrick Mercier, Co-Chair
- Professor Peter Asbeck
- Professor Gert Cauwenburghs

San Diego State University
- Professor Chris Mi, Co-Chair
- Professor Madhu Gupta

2018

The dissertation of Tianze Kan is approved, and it is acceptable in quality and form for publication on microfilm and electronically:

_____

_____

_____

_____

Co-Chair

_____

Co-Chair

University of California San Diego

2018

DEDICATION

To my parents and my cousin.

TABLE OF CONTENTS

LIST OF FIGURES

LIST OF TABLES

LIST OF ABBREVIATIONS

AC	Alternating current
AUV	Autonomous underwater vehicle
CC	Constant current
CR	Constant resistance
DC	Direct current
EMI	Electromagnetic interface
ESR	Equivalent series resistance
EV	Electric vehicle
FHA	First harmonic analysis
FEA	Finite element analysis
RMS	Root mean square
WPT	Wireless power transfer
ZPA	Zero phase angle
ZVS	Zero voltage switching

ACKNOWLEDGEMENTS

My Ph.D. study was full of blessings. I met my advisor Professor Chris Mi in his seminar at EEB 248 of USC on April 1st, 2013 and started my Ph.D. study since then. I would like to express my deepest appreciation to Professor Mi for teaching me independent thinking, offering me with guidance in research, pushing me to improve my ability to learn innovative techniques.

I was extremely fortunate to be co-advised by Professor Patrick Mercier after I transferred to San Diego. I would like to express my sincerest gratitude to Professor Mercier for his invaluable supervisions and comments on my research. I would also like to show my greatest appreciation to my committee members Professor Peter Asbeck, Professor Gert Cauwenburghs, and Professor Madhu Gupta for their support and contributions.

None of the entire work would have been possible without the sponsors. I would like to thank DOE GATE Center, U.S.-China Clean Energy Research Center, DENSO North America, Inc., San Diego State University, and ANSYS Inc. for providing me with fellowship, assistantship, and technical support.

I have greatly benefited from my collaborators in my Ph.D. study: Trong-Duy Nguyen – I was deeply grateful to you and our discussions on the integrated coil design have been illuminating. Wei Zhang – thank you for teaching me to use ANSYS MAXWELL and MathCAD, which turned out to be the two most important tools in my Ph.D. Study. Fei Lu and Jiyuan Fu – we spent days and nights together removing the enamels from litz wires, winding innovative coils, and conducting exciting experiment; thank you for your companion. Zicheng Bi – It was an honor to co-authorize the review paper, and our insightful discussions on well arranging the paper and wisely responding to reviewers' comments paid off. Professor Ruikun Mai – it was my pleasure working with you and I learnt a lot from you in theoretically

understanding wireless charging systems. Yiming Zhang and Zhengchao Yan – It was never too late to have such excellent coworkers as you and it was great working with you to successfully deliver the rotation-resilient coil. I would also like to thank my co-authors Jeff White and Rajesh Malhan from DENSO North America Inc., Professor Zhengming Zhao from Tsinghua University, and Professor Greg Keoleian from University of Michigan for their help and support.

Past and present members from Mi-Group played an important role in my Ph.D. study. I would like to thank Bing Xia, Xianzhi Gong, Alessandro Pevere, Zeyu Ma, Weihan Li, Junjun Deng, Xiaohang Yu, Hang Dai, Bowen Zhang, Yunlong Shang, Jufeng Yang, Jiaxue Wang, Chong Zhu, Hua Zhang, Haili Cai, Chenwen You, Professor Chung-Ming Young, and Yuhong Fu for all the help, support, and encouragement. I would like to offer my special thanks to Bing Xia - I have learned an incredible amount from you as a junior coworker, as a roommate, and as a sports teammate.

Last, but definitely not the least, I would like to thank my family. I would like to thank my parents for their unconditional love and endless support. This was my seventh year studying aboard and I owed them too much. I would also like to thank my cousin's family for providing me such a cozy home at San Diego. I felt particularly grateful to my cousin who had a significant impact on my personal and professional development. As a Ph.D. in control theory, she taught me how to well balance life and research, and efficiently perform multitask in a stable way with a small overshoot and a short settling time.

In this dissertation, Chapter 1 is based on the following published paper. As the co-first author, I led and drafted the technical analysis of the paper.

Z. Bi[*], T. Kan[*], C. C. Mi, Y. Zhang, Z. Zhao, and G. A. Keoleian, "A review of wireless power transfer for electric vehicles: Prospects to enhance sustainable mobility," *Applied Energy*, vol. 179, pp. 413–425, Oct. 2016.[*equal contribution]

Chapter 2 is based on the following published paper. As the first author, I proposed and analyzed the coil structure, developed the design procedures, conducted the experiment, and drafted the paper.

T. Kan, T. D. Nguyen, J. C. White, R. K. Malhan, and C. Mi, "A new integration method for an electric vehicle wireless charging system using LCC compensation Topology: Analysis and Design," *IEEE Trans. Power Electron*., vol. 32, no.2, pp. 1638–1650, Feb. 2017.

Chapter 3 is based on the following accepted paper. As the first author, I proposed and analyzed the coil structure, performed simulations, conducted the experiment and the discussions, and drafted the paper.

T. Kan, F. Lu, T. D. Nguyen, P.P. Mercier, and C. Mi, "Integrated coil design for EV wireless charging systems using LCC compensation topology," *IEEE Trans. Power Electron*., 2018. [in press]

Chapter 4 is based on the following accepted paper. As the first author, I proposed the coil structure, performed finite element analysis, conducted the experiment, and drafted the paper.

T. Kan, R. Mai, P. P. Mercier, and C. Mi, "Design and Analysis of a Three-Phase Wireless Charging System for Lightweight Autonomous Underwater Vehicles," . *IEEE Trans. Power Electron*., 2017. [in press]

Chapter 5 is based on the following accepted paper. As the first author, I proposed the coil structure, performed finite element analysis, conducted the experiment, and drafted the paper.

T. Kan, Y. Zhang, Z. Yan, P. P. Mercier, and C. Mi, "A Rotation-Resilient Wireless Charging System for Lightweight AUVs," *IEEE Trans. Veh. Technol*., 2018. [accepted]

VITA

2007-2011	B.Eng., Huazhong University of Science and Technology, Wuhan
2011-2013	M.S., University of Southern California, Los Angeles
2013-2015	Ph.D. Student, University of Michigan, Dearborn
2015-2018	Ph.D., University of California San Diego/San Diego State University

PUBLICATIONS

Journal Publications

T. Kan, F. Lu, T. D. Nguyen, P.P. Mercier, and C. Mi, "Integrated coil design for EV wireless charging systems using LCC compensation topology," *IEEE Trans. Power Electron*., 2018. [in press]

T. Kan, R. Mai, P. P. Mercier, and C. Mi, "Design and Analysis of a Three-Phase Wireless Charging System for Lightweight Autonomous Underwater Vehicles," *IEEE Trans. Power Electron*., 2017. [in press]

T. Kan, T. D. Nguyen, J. C. White, R. K. Malhan, and C. Mi, "A new integration method for an electric vehicle wireless charging system using LCC compensation Topology: Analysis and Design," *IEEE Trans. Power Electron*., vol. 32, no.2, pp. 1638–1650, Feb. 2017.

X. Zhang, T. Kan, C. You, and C. Mi, "Modeling and analysis of AC output power factor for wireless Chargers in electric vehicles, "*IEEE Trans. Power Electron*., vol. 32, no. 2, pp. 1481–1492, Feb. 2017.

Z. Bi[*], T. Kan[*], C. C. Mi, Y. Zhang, Z. Zhao, and G. A. Keoleian, "A review of wireless power transfer for electric vehicles: Prospects to enhance sustainable mobility," *Applied Energy*, vol. 179, pp. 413–425, Oct. 2016. [[*] equal contribution]

W. Li, H. Zhao, S. Li, J. Deng, T. Kan, and C. C. Mi, "Integrated LCC compensation topology for wireless charger in electric and plug-in electric vehicles," *IEEE Trans. Ind. Electron.*, vol. 62, no. 7, pp. 4215–4225, July. 2015.

Conference Publications

T. Kan, R. Mai, P. P. Mercier, and C. Mi, "A Three-Phase Wireless Charging System for Lightweight Autonomous Underwater Vehicles," in Proc. *Applied Power Electronics Conference (APEC)*, Mar. 2017.

F. Lu, H. Zhang, T. Kan, H. Hofmann, Y. Mei, L. Cai, and C. Mi, “A high efficiency and compact inductive power transfer system compatible with both 3.3kW and 7.7kW receivers,” in Proc. *Applied Power Electronics Conference (APEC)*, Mar. 2017.

W. Li, H. Zhao, T. Kan, and C. Mi, “Inter-operability considerations of the double-sided LCC compensated wireless charger for electric vehicle and plug-in hybrid electric vehicle applications,“ in *Proc. IEEE PELS Workshop Emerging Technol. : Wireless Power*, 2015, pp. 1-6

ABSTRACT OF THE DISSERTATION

Application-Oriented Coil Design in Wireless Charging Systems

By

Tianze Kan

Doctor of Philosophy in Engineering Science (Electrical and Computer Engineering)

University of California San Diego, 2018

San Diego State University, 2018

Professor Chris Mi, Co-Chair

Professor Patrick Mercier, Co-Chair

The concept of wireless power is originated from Heinrich Hertz and well known by the work of Nikola Tesla. Magnetic resonance-based wireless power transfer has been widely applied in charging biomedical implants, consumer electronics, electric vehicles, and lightweight autonomous underwater vehicles due to its convenience and reliability. As a core part of a wireless charging system, coil design is of great importance. This dissertation will introduce four coil designs based on the applications of wirelessly charging electric vehicles and lightweight autonomous underwater vehicles.

Chapter 2 proposes an integrated coil design for bipolar coils in EV wireless chargers using LCC compensation topology, which simplifies the design, makes the system more compact,

and increases the system power density. Finite element analysis by ANSYS MAXWELL is conducted to verify the proposed idea. In addition, a design method on improving system efficiency is given and experimental results demonstrate that wireless charging system with the proposed integrated coil design can transfer 3.0 kW at a DC-DC efficiency of 95.5%.

Chapter 3 extends the work of Chapter 2 and presents another integrated coil design which is compatible with unipolar coils in EV wireless chargers using LCC compensation topology. The aspect ratios of the compensated coils are study in ANSYS MAXWELL to minimize the extra cross-side coupling coefficient. A wireless charging with the proposed integrated coil design is built to achieve 3.0 kW power transfer at a DC-DC efficiency of 95.5%. Furthermore, a comparative study of the two wireless charging systems in Chapters 2 and 3 are conducted, and the results show the wireless charging system in Chapter 3 has competitive performance in fully aligned and door-to-door misaligned cases, and superior performance in vertical and front-to-rear misaligned cases.

Chapter 4 puts forward a three-phase coil design for lightweight autonomous underwater vehicles. Finite element analysis shows the proposed coil structure has concentrated magnetic fields, which have less adverse effects on the instrumentations within the AUV. A compensation method is presented and a three-phase wireless charging system is built to transfer 1.0 kW at a DC-DC efficiency of 92.41%.

Chapter 5 proposes a rotation-resilient coil design with a two-part reversely wound receiver for lightweight autonomous underwater vehicles in order to achieve a constant power transfer over rotational misalignment. Finite element analysis is performed to verify the proposed coil design and a mesh-current method is applied in analyzing the circuit. A wireless charging

system is built to deliver 745 W at a DC-DC efficiency of 86.19% when the system is fully aligned, and efficient under worst-case rotational misalignment.

Chapter 1

Introduction

1.1 Background

The idea of wireless power originates from German physicist Heinrich Hertz. In late 1880s Dr. Hertz succeeded in receiving radio waves wirelessly from his spark gap transmitter [1]. The concept of wireless power transfer (WPT) is popularized by Nikola Tesla, who proposed the idea of using the wardenclyffe tower to transfer electrical energy with no wires around the world [2]. Though his experiment was later abandoned, his thought of transmitting power wirelessly was of far-reaching influence. In 1964, William C. Brown invented the first microwave-based WPT system, powering an unmanned aerial vehicle [3]. The WPT application on long-distance power transmission gained large popularity in late 1970s. However, long-distance power transmission requires large space-based apparatus and high electromagnetic field strength, which is of high cost and danger [4]. The topic of WPT gradually transferred from far field applications to near field applications. Recently, the interest of wireless power is peaked again by a research team from Massachusetts Institute of Technology, who demonstrated a WPT system to transfer 60 watts with 40% efficiency over a distance of 2 meters [5]. Nowadays, WPT is widely used in charging biomedical implants, tooth brushes, cell phones, laptops, electric vehicles (EVs), and even autonomous underwater vehicles (AUVs) [6-53]. The amount of power transferred ranges from several milliwatts to hundreds of kilowatts and the frequency of interest covers from hundreds of kHz to hundreds of MHz. As the application differs, the required power level and operating frequency of the wireless charging system vary. In this dissertation, we focus on

wirelessly charging EVs and lightweight AUVs. The output power is in kW level and the frequency is 85 kHz in EV applications and 500 kHz for lightweight AUV applications.

EVs, propelled by electric motors, are now very popular in people's life. There are two charging options: conductive charging and wireless charging. Compared to conductive charging, wireless charging has three advantages:

(1). It is convenient. As the EV is parked, it can be charged wirelessly and automatically. There is no further action required.

(2). It is safe. The power relies on the generated magnetic field to be transferred; therefore, it does not generate any electric shock.

(3). It is reliable. As the generated magnetic field does not interfere with water or dust, it can be employed in harsh environment.

Due to the three main advantages, wireless charging is an important charging option for EV customers. Further research is needed and required in this application.

Lightweight AUVs, powered by rechargeable batteries, are widely deployed in inshore surveying, environmental monitoring, and mine countermeasures. While providing valuable information in locations humans have difficulty accessing, limited battery capacity of such systems prevents extended mission times. AUVs are thus required to go back to their base station, get charged, and return to its mission afterwards. There are two conventional charging options: conductive charging and battery swapping. Conductive charging, in which a physical connection between the charging station and the AUV is established, is efficient and straightforward. However, it is necessary to provide a hermetic seal along the connection electrodes, which can be difficult when making connections in seawater. Battery swapping, in which a discharged battery is replaced by a fully charged one, effectively shortens the charging time and the AUV

could be back to mission immediately. However, it requires complex battery insertion and retrieval mechanisms [33]. Moreover, frequent battery swapping results in problems on AUV's airtightness. In order to provide a convenient, safe, and reliable charging option, wireless charging appears. The AUVs can be charged wirelessly at its underwater docking station via the generated magnetic field with no physical connection.

1.2 Research Areas

Figure 1.1 shows a kW-level wireless charging system through near-field magnetic coupling. The alternating current (AC) utility power first goes through the electromagnetic interface (EMI) stage, and then gets rectified and boosted to direct current (DC) power with a power factor of nearly 1.0 (0.95 to 0.98 in most cases), which is similar to the rectifier/PFC circuit in a conductive charging system [44]. The voltage of the DC power is decreased by an optional BUCK stage. The BUCK stage can tune its output voltage to range from 0.03 to 0.97 of its input voltage, which achieves "soft" start/stop of the charger and continuous tuning of its output power. Here, the buck stage is optional since a pre-charge circuit, which is composed of two contactor relays and one resistor, is able to help achieve "soft" start of the charger and phase-shift method can be used in the inverter stage to ensure the low power operation and "soft" stop of the charger. This combination of a pre-charge circuit and phase-shift method instead of a buck stage may reduce the system efficiency, but it will save the total cost and volume of a wireless charging system. In the inverter stage, the DC power is converted to high frequency AC power, which then resonates in the primary compensation network and the primary coil, with the resonant frequency adjusted to the switching frequency of the inverter. The secondary coil receives the high frequency AC power wirelessly through the mutual inductance between the primary and secondary coils. The secondary compensation network, together with the secondary

coil, is required to be tuned to have the same resonant frequency in order to maximize the transfer efficiency. The high frequency AC power is then rectified to DC power through the rectifier stage and filtered by the filter network. Finally, the DC power is available to charge the battery pack.

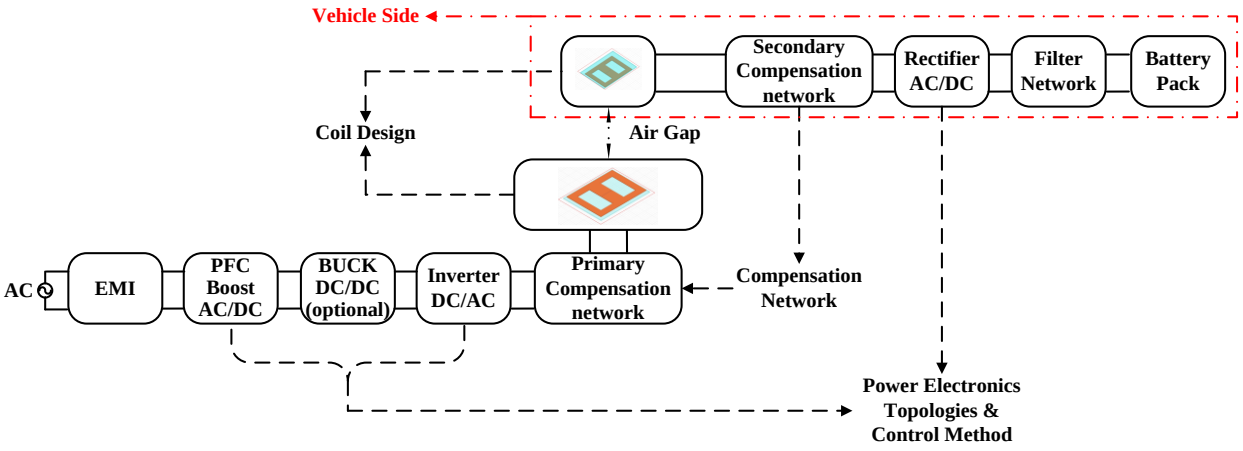

Figure 1.1: A kW-level wireless charging system. AC = alternating current; EMI = electromagnetic interface; PFC = power factor correction; DC = direct current.

Research into wireless charging systems is mainly focused on three areas: (1) coil design; (2) compensation topologies; and (3) power electronics converters and control methods.

1.2.1 Coil design

The coil is one of the most significant parts in a wireless charging system. The coils convert energy between its electric form and its magnetic form, making WPT possible, while also determining the amount of power transferred and the system efficiency. In the literature, a coil system is generally classified as either a four-coil or a two-coil system. A four-coil system [45-47] offers the advantage of two degrees of freedom that the source coil can be mounted and coupled with the sending coil to adjust the system input impedance, and the load coil can be mounted and coupled with the receiving coil to adjust the equivalent load resistance seen from the receiving coil to match the load condition. A four-coil system is suitable for mid-range

applications while a two-coil system gives better performance in short-range applications [48]. In [48], applications are considered short-range or mid-range based on whether the transmission distance is smaller or larger than the coil dimension. In EV applications, the transmission distance, also known as air gap, ranges typically from 100 mm to 300 mm [23], and the coil dimension is always larger than the transmission distance. So are the AUV applications. Therefore, a two-coil system is preferable and will be reviewed in detail in this chapter. In addition, ferrite bars or plates are always employed in coil systems to guide magnetic flux and provide magnetic shielding. Aluminum shields are often built into a coil system and serve as magnetic shields.

Basic coil systems for stationary charging systems are shown in Figure 1.2 (a) to (c). Circular coil structures were studied and optimized in [8]. With the proposed coil structure, the system was able to transfer 2–5 kW wirelessly at a relatively high efficiency [8, 49]. However, the height of magnetic flux generated by the circular coil is limited. In order to solve this problem, Budhia et al. [50] developed the solenoid coil structure, which improved the magnetic flux path. It was reported in [9] that a 3 kW wireless charging system using solenoid coil structure was built and a DC-DC efficiency of 90% was achieved with an air gap of 200 mm. In addition, the solenoid coil structure performs well in wireless power transmission with a large air gap. Park et al. [51] optimized the solenoid coil shapes and demonstrated a wireless charging system that delivered 1.403 kW power at an air gap of 3 meters. The performance of the solenoid structure is fairly good, but there is a severe drawback. It generates double-sided flux and half of the flux is not used in transferring power. In addition, the unused flux may couple with the chassis of the vehicle and steel buried in the ground, which will greatly decrease the system efficiency. Therefore, this coil structure is not widely used in EV charging applications. However,

it is suitable in AUV charging application. In order to have a single-sided flux path and a larger charging zone than the circular coil structure, a bipolar coil structure known as a DD coil structure was developed in [10]. The bipolar coil structure shows excellent system efficiency at the desired power level with good tolerance to horizontal misalignment. Nguyen et al. [11] simulated the bipolar coil structure with the same size but different aspect ratios (ratio of width and length of a rectangular geometry). They built a wireless charging system employing the bipolar coil structure with the optimized aspect ratio to transfer 8 kW with a DC-DC efficiency of 95.66% at an air gap of 200 mm. Even when the horizontal misalignment increased to 300 mm, the system DC-DC efficiency was still as high as 95.39% [52].

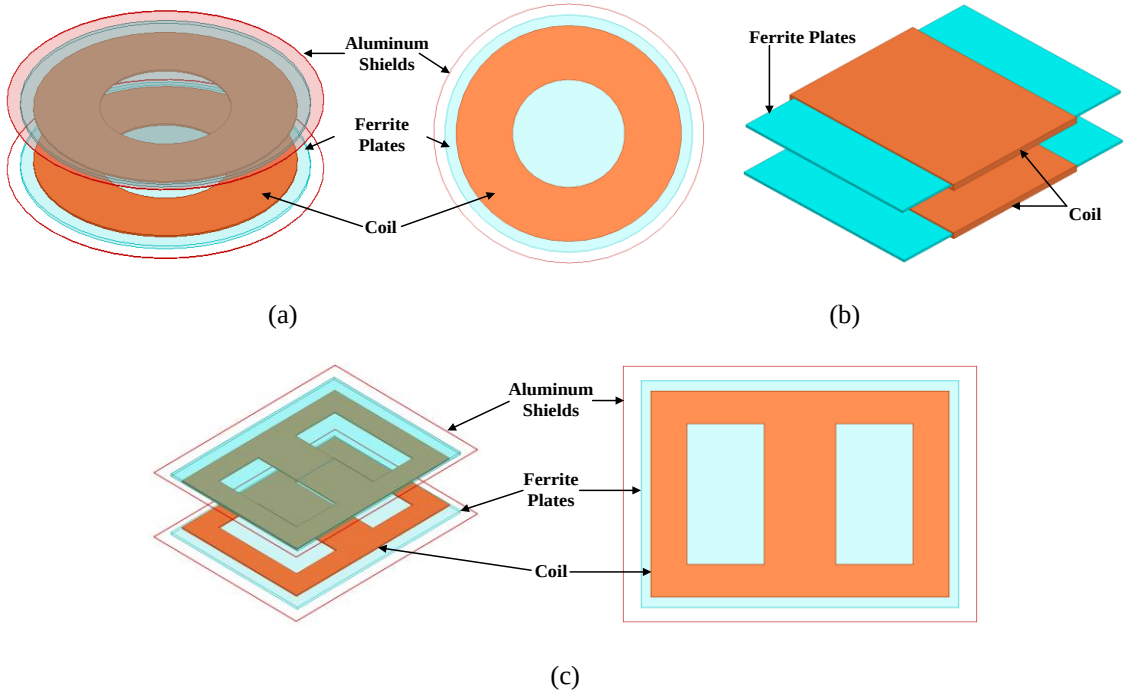

Figure 1.2: Coil systems: (a) Circular structure (b) Solenoid structure (c) Bipolar structure.

A more advanced coil design can be found in [41]. Figure 1.3 shows the proposed coil structure, where intermediate L_{int} is embedded into the primary coil structure L_1. L_{int} and its resonant capacitor form a passive resonant circuit, which is energized through coupling effect between L_{int} and L_1. Since there is also a coupling effect between L_{int} and the secondary coil

structure L_2, the coupling of the whole coil system is improved. This design claims a higher efficiency than that of a circular coil system, though in terms of tuning it is more complicated.

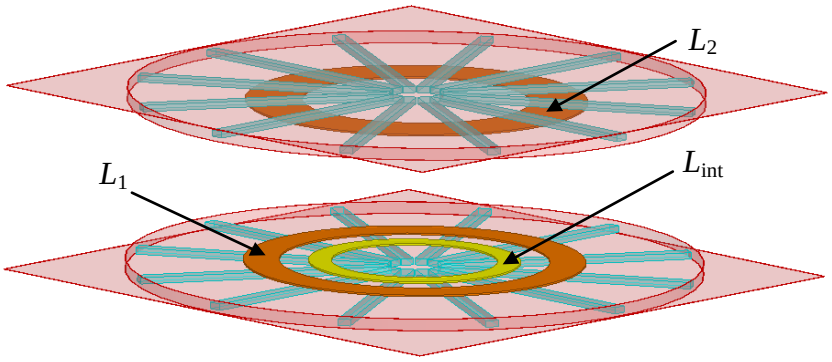

Figure 1.3: Advanced coil structure. L_{int} = intermediate structure; L_1 = primary coil structure; L_2 = secondary coil structure. [41]

1.2.2 Compensation topologies

A two-coil system is a loosely coupled transformer [27] with leakage inductances that require the use of compensation topologies. On the primary (or transmitter) side the compensation topology is employed to minimize the VA rating of the power supply and achieve zero phase angle (ZPA), which means there is no need for the power supply to provide reactive power so the apparent power equals the real power. On the secondary (or receiver) side the compensation topology tunes the circuit to have the same resonant frequency as the transmitter side to maximize power transfer [42]. In addition, compensation topologies help soft switching of power transistors and reduce switching losses. Another benefit of compensation topologies is to achieve constant current or constant voltage charging, which means when the root mean square value of the input voltage is fixed, then either output DC current or DC voltage is fixed. Four basic compensation topologies, named SS, SP, PS, and PP, are presented in Figure1.4. Here, "S" or "P" stands for series or parallel, indicating how the compensation capacitors are connected to the coils. The first letter represents the transmitter side and the second letter

represents the receiver side. First harmonic analysis (FHA) is a basic analysis method used to analyze the circuits and v_{ac} is the fundamental component of the input voltage of the inverter stage. Although the battery is a voltage-source-based load and the battery voltage varies with its state of charge, the battery voltage value needs to be fixed as a criterion for designing a wireless charging system at the rated power level. Therefore, the battery is considered as a resistive load and R_{eq} is the equivalent resistance at the input side of the rectifier stage.

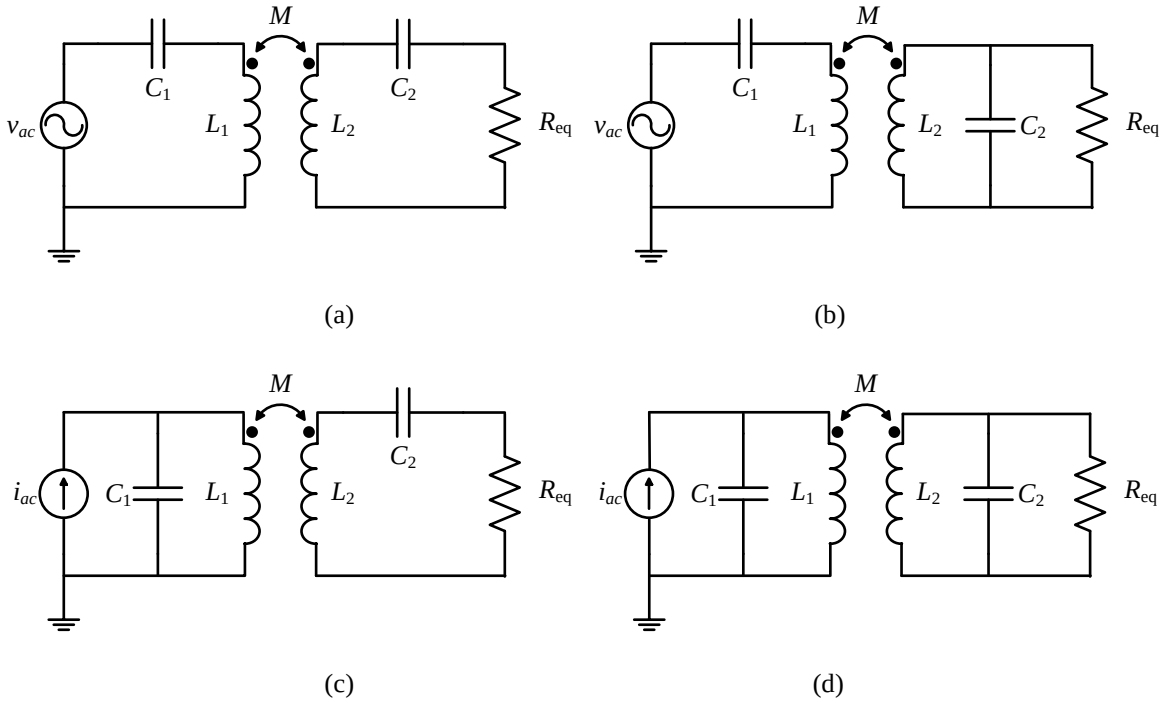

Figure1.4: Basic compensation topologies: (a) SS, (b) SP, (c) PS, and (d) PP. C_1, C_2 = capacitors; L_1, L_2 = coils; v_{ac} = alternating voltage; i_{ac} = alternating current; M = mutual inductance between the primary and secondary coils; R_{eq} = equivalent resistance.

The four basic compensation topologies were analyzed in [28, 54, 55, 56]. SS and SP are more economically suitable for high power transmission [56]. Wang et al. [54] introduced the bifurcation phenomenon and studied the four basic compensation topologies. They demonstrated that the primary capacitance C_1 in PS and PP compensation topologies depends on the load condition while in SS and SP compensation topologies it does not. Therefore, SS and SP

compensation topologies are more suitable for variable load conditions since the resonance is guaranteed.

A more recent compensation topology, known as the double-sided *LCC* compensation topology, was proposed by researchers from the University of Michigan, Dearborn (UM-Dearborn) [13]. As shown in Figure 1.5, the compensated coil L_{f1} resonates with the capacitor C_{f1}; therefore, i_1 is a constant current once v_{ac} is fixed and the induced voltage source $j\omega M i_1$ is constant (ω is angular frequency in radians per second). On the receiver side, L_2 and C_2 are combined together to resonate with C_{f2} and as a result, the resonant frequency is independent of the load condition and coupling coefficient. The output current is constant, which is desirable for battery charging. Due to the symmetry of the double-sided compensation topology, L_{f2} resonates with C_{f2} while L_1 and C_1 are combined to resonate with C_{f1}. The expressions for output current i_{f2}, output power P, and coupling coefficient k are given in (1.1), (1.2), and (1.3) below, respectively:

$$i_{f2} = \frac{k\sqrt{L_1 L_2}v_{ac}}{j\omega L_{f1} L_{f2}} = \frac{2\sqrt{2}}{\pi} \cdot \frac{k\sqrt{L_1 L_2}V_{in}}{\omega L_{f1} L_{f2}} \angle -90^{\circ} \tag{1.1}$$

$$P = \frac{8k\sqrt{L_1 L_2}V_{in}V_{out}}{\pi^2 \omega L_{f1} L_{f2}} \tag{1.2}$$

$$k = \frac{M}{\sqrt{L_1 L_2}} \tag{1.3}$$

where V_{in} is the input voltage of the inverter stage, V_{out} is the battery pack voltage, and M is mutual inductance of primary (L_1) and secondary (L_2) coils. As can be seen from (1.1) and (1.2), the output current is constant when V_{in} is fixed and the output power is linearly related to the coupling coefficient k in the two-coil system.

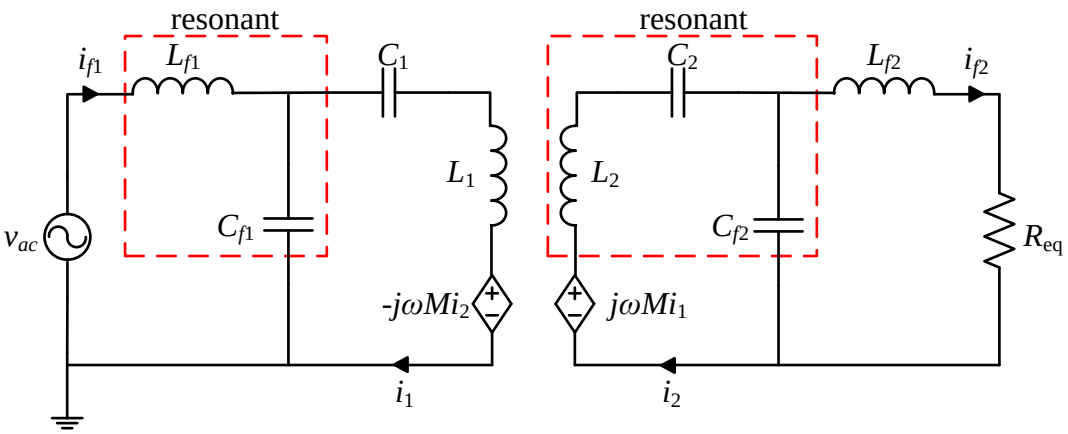

Figure 1.5: A double-sided *LCC* compensation topology. v_{ac} = alternating voltage; L_1, L_2, L_{f1}, L_{f2} = coils; C_1, C_2, C_{f1}, C_{f2} = capacitors; i_1, i_2, i_{f1}, i_{f2} = current; R_{eq} = equivalent resistance; $j\omega Mi_1$ = induced voltage source; $-j\omega Mi_2$ = the voltage induced by the secondary coil. [52]

1.2.3 Power electronics converters and control methods

On the transmitter side, power electronics converters transform 60 Hz utility AC power into high frequency AC power on the desired power level. There are two methods to achieve the conversion: (1) The dominant method is the indirect two-stage power conversion, with the 60 Hz utility power first rectified into DC power, then inverted into high frequency AC power using a full-bridge inverter; (2) The other less commonly used method is the direct power conversion from 60 Hz utility AC power to high frequency AC power utilizing AC/AC converters. On the receiver side, the high frequency AC power is rectified to DC power using a full-bridge rectifier in order to charge battery packs. The resonant frequency is set by the compensation networks and realized by the inverter. The resonant frequency or the switching frequency of the inverter ranges from 20 kHz to 100 kHz in wireless charging systems for EVs. However, with the advent of new silicon carbide MOSFETs, the resonant frequency can be as high as 1 MHz [20]. Higher frequencies make the wireless charging system more compact, but other issues introduced by high frequency AC, such as EMF emissions, need to be further studied.

The control method of a wireless charging system is an important topic closely related to power electronics converters. Many control methods have been developed in wireless charging systems [32, 49, 57-60]. In the stationary charging applications, the control methods are designed to achieve high system efficiency, desired outputs, and bidirectional power transfer between grid and battery packs. In [21], the authors proposed a new dual side control method and established a 5.0 kW wireless charging system with over 90% grid-to-battery efficiency. Zahid et al. [57] studied the small-signal model of a wireless charging system and controlled the switching frequency of the inverter on the transmitter side to achieve the desired output voltage. Researchers from ORNL employed a semi-bridgeless active rectifier on the receiver side and proposed a control strategy to phase-shift tune the switches in order to adjust the output voltage. Furthermore, they pointed out that the proposed control method was suitable for multiple secondary coil applications [58]. Control methods to realize bidirectional power flow were given in [32, 49]. Bidirectional WPT for EVs can achieve interactions between mass EVs and the power grid. EVs can be regarded as controllable power source and load at the same time, which is beneficial for the power balance of the grid. Ref. [61] presented an optimized phase-shift modulation strategy to minimize the coil losses of a series-series WPT system. In dynamic charging applications, control methods were studied for fast turn-on in the tracking circuit without overshoot in a no-load condition [32] and for energizing the primary coils to control the amount of power received by the secondary coil [60].

1.3 Contributions of the Dissertation

This dissertation separately addresses four coil designs based on applications of wirelessly charging EVs and light AUVs. For EV wireless charging systems, the proposed coil designs make the systems more compact and as a result, the power densities are increased. For

AUV wireless charging systems, the proposed coil designs generate concentrated magnetic fields with less adverse effects on the instrumentation within the AUVs and have superior performance over rotational misalignments. The main contributions of this dissertation are given in the following chapters:

Chapter 2 presents an integrated coil design for EV wireless chargers using the LCC compensation topology, which is compatible with bipolar coils. With the proposed integration method, the system is more compact, and the extra coupling effects are eliminated or minimized to a negligible level. Additionally, the detailed design procedures on improving system efficiency are developed. A prototype with the proposed integrated coil design is built and experimental results show the system is able to deliver 3.0 kW at a DC-DC efficiency of 95.5%.

Chapter 3 extends the work of Chapter 2 by analyzing and demonstrating a different integrated coil design that is compact and efficient, and importantly, compatible with unipolar coils in EV wireless charging systems using the LCC compensation topology. Aspect ratios are defined and studied to minimize the extra cross-side coupling effects after coils' integration. A wireless charging system with the proposed integration method is built to transfer 3.09 kW with a DC-DC efficiency of 95.49%. Furthermore, experimental results in Chapter 3 and Chapter 2 are compared, and results show that the wireless charging system with the integration method in Chapter 3 has a competitive performance in fully-aligned condition and door-to-door misalignment, while achieving superior performance under front-to-rear and vertical misalignments.

Chapter 4 proposes a three-phase coil structure consisting of three transmitters and three receivers for wirelessly charging lightweight AUVs. The generated magnetic field is more

concentrated in the coil structure or out of the AUV's hull, causing less adverse effects on the instrumentations within the AUV.

Chapter 5 further proposes a rotation-resilient coil structure with a reversely wound receiver for lightweight AUVs to improve the system performance over rotational misalignments. With a two-part reversely wound receiver, the system output power is relatively constant during rotational misalignment.

Chapters 2, 3, 4, and 5 are respectively based on the four papers below:

[1]. T. Kan, T. D. Nguyen, J. C. White, R. K. Malhan, and C. Mi, "A new integration method for an electric vehicle wireless charging system using LCC compensation Topology: Analysis and Design," *IEEE Trans. Power Electron*., vol. 32, no. 2, pp. 1638–1650, Feb. 2017.

[2]. T. Kan, F. Lu, T. D. Nguyen, P.P. Mercier, and C. Mi, "Integrated coil design for EV wireless charging systems using LCC compensation topology," *IEEE Trans. Power Electron*., vol. PP, no. 99, pp. 1-11, Jan. 2018.[in press].

[3]. T. Kan, R. Mai, P. P. Mercier, and C. C. Mi, "Design and analysis of a three-phase wireless charging system for lightweight autonomous underwater vehicles," *IEEE Trans. Power Electron* vol. PP, no. 99, pp. 1-11, Sep. 2017.[in press]

[4]. T. Kan, Y. Zhang, Z. Yan, P. P. Mercier, and C. C. Mi, "A rotation-resilient wireless charging system for lightweight autonomous underwater vehicles," *IEEE Trans. Veh. Technol.* 2018.[accepted]

Chapter 2

Integrated Coil Design in EV Bipolar Coils

2.1 Introduction

An important application of magnetic-resonance based wireless power transfer is to charge EVs. In an EV wireless charging system, it consists of coils, compensation networks, power converters, filtering banks, and other circuits and components for communication and protections. Coils are the essence as they set the theoretically achievable power transfer rate and efficiency. In general, it is desired to maximize their quality factor by geometrical arrangement: the higher quality factor and the coupling coefficient, the higher the system efficiency. In stationary EV wireless charging systems, there are mainly three coil structures [24]: (1) solenoid coil structures [9], (2) unipolar coil structures [8], and (3) bipolar coil structures (also referred to as DD coil structures) [10]. Since solenoid coils generate a double-sided magnetic flux pattern, half of which does not couple the receiver, they are not commonly adopted in EV charging applications. Instead, unipolar and bipolar coils are more popular. Unipolar coils, in which one pair of magnetic polarities is generated once the coils are excited, give a relatively higher coupling coefficient and generate vertical magnetic flux. Bipolar coils, in which two pairs of magnetic polarities are generated once the coils are excited, present a relatively lower coupling coefficient and develop horizontal magnetic flux. Experimental results in [11] show that bipolar coils have a better performance when horizontal misalignment occurs in the direction vertical to magnetic flux conduction path, which is the door-to-door direction. This chapter will focus on employing bipolar coils to transfer power in EV wireless chargers.

To minimize the VA-rating of the power supply and maximize transferred power, coils in EV wireless charging systems are typically not driven directly, but instead, are compensated with a collection of capacitors and inductors [42]. Compensation in this manner can help achieve soft switching, thereby improving the efficiency of the corresponding power converters. It can also help deliver a constant current or constant voltage output, which may be advantageous in various applications [42, 13]. Among the four basic compensation topologies (i.e. SS, SP, PS, and PP), SS is more widely used in EV wireless charging systems since the resulting resonance is independent of the coupling coefficient and load condition. However, it is not strictly necessary to employ only a single reactive compensation element per coil – for example, the double-sided LCC topology, proposed in [13], includes an inductor and two capacitors on each side of the circuit. The LCC topology inherits the advantages of the SS compensation topology while offering more flexibility to optimize the system efficiency and achieve zero voltage switching. However, compared to SS, the double-sided LCC topology has an obvious drawback: the two compensated inductors occupy a large volume.

In order to address the large volume increase, Li et al [14] proposed integrating the compensated inductors into the bipolar main coils. The integration method can effectively make an LCC wireless charging system more compact; however, three additional types of coupling coefficients manifest as illustrated in Figure 2.1: same-side coupling coefficients k_{1f1} and k_{2f2}, cross-side coupling coefficients k_{1f2} and k_{2f1}, and extra cross-side coupling coefficient k_{f1f2}. Li et al analyzed the extra coupling coefficients and built a wireless charging system to transfer 6.0 kW with a DC-DC efficiency of 95.3%. It successfully makes the system more compact and highly efficient; however, the method of integration complicates the design of a wireless charging system using double-sided LCC compensation topologies.

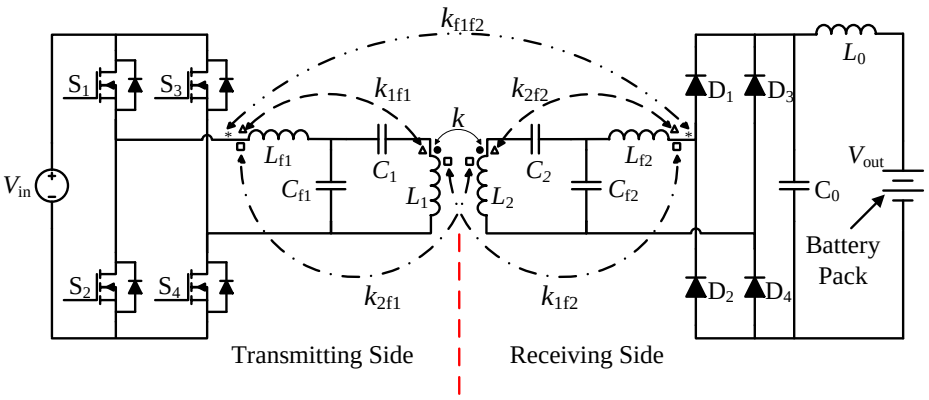

Figure 2.1: Couplings among coils in double-sided LCC compensation topology after integration.

In order to simplify the design and analysis while keep the advantages of compactness and high efficiency, this chapter proposes a new integration method for bipolar coils in an EV wireless charging system using LCC compensation topology. In this method, the five extra coupling effects are either eliminated or minimized to a negligible level, which greatly simplifies the design and analysis. Additionally, a new method of improving system efficiency is given. Consequently, the system keeps outstanding performance and is able to deliver 3.0 kW power with 95.5% DC-DC efficiency at an air gap of 150 mm.

2.2 Analysis

The double-sided LCC compensation topology is proven to be highly efficient for WPT applications in electric vehicles and plug-in electric vehicles [13-16]. As shown in Figure 2.1, the DC input is transformed to a high frequency AC power by a full-bridge inverter, which is formed by MOSFET switches S_1~S_4. On the transmitting side, also known as the primary side, L_{f1}, C_{f1}, C_1, and L_1 constitute the primary resonant tank, which is tuned to have a resonant frequency the same with the switching frequency of the full-bridge inverter. The high frequency AC power resonates in the primary resonant tank. On the receiving side, which is also called the secondary side, L_{f2}, C_{f2}, C_2, and L_2 make up the secondary resonant tank. In order to receive power from the

transmitting side, the secondary resonant tank also has the same resonant frequency. Since there is no wire connection between the transmitting side and the receiving side, the high frequency AC power is transmitted wirelessly through the main coupling between the main coils L_1 and L_2. Afterwards, it is converted back to DC by the rectifier consist of four diodes D_1~D_4. After being further filtered by the CL-filter, the power is qualified to charge the battery packs.

As can be seen from Figure 2.1, the double-sided LCC compensation topology involves four magnetic components: L_{f1}, L_1, L_2, and L_{f2} where L_1 and L_2 are the main coils while L_{f1} and L_{f2} are the compensated coils. L_{f1} and L_{f2} are air-core inductors; however, the large dimension of air-core inductors is not practical in reality. In order to make the system more compact, we propose to integrate the compensated coils into the main coil system. Once they are integrated, extra couplings appear. As shown in Figure 2.1, six couplings exist and the coupling coefficients are chosen to represent their coupling effects, where k stands for the coupling coefficient between the main coils L_1 and L_2 while k_{f1f2} represents the coupling coefficient between compensated coils L_{f1} and L_{f2}; k_{1f1} is the coupling coefficient between L_1 and L_{f1} and similarly, k_{2f2} is the coupling coefficient between L_2 and L_{f2}, k_{1f1} and k_{2f2} refer to the same-side coupling coefficients; k_{1f2} and k_{2f1} are the coupling coefficient between L_1 and L_{f2}, the coupling coefficient between L_2 and L_{f1}, respectively, and k_{1f2} and k_{2f1} are also known as cross-side coupling coefficients. Moreover, in Figure 2.1 the main coupling coefficient k is represented by a solid line while the other five is in dashed or dash-dot lines. WPT relies on the main coupling to transmit power wirelessly between the transmitting side and the receiving side; therefore, the main coupling between L_1 and L_2 is of great significance and the other five couplings are redundant. The goal is to maximize the main coupling and eliminate the five extra couplings or minimize their coupling effects to a negligible level.

Figure 2.2 presents the proposed integrated coil structure. The main coils L_1 and L_2 are in bipolar. Due to the onboard space limitation, the size of the coil structure on secondary side is smaller than that on primary side. Unipolar coils are chosen for compensated coils L_{f1} and L_{f2}. Since both the primary side and the secondary side have similar coil structures, analysis will be first focused on one side. On the primary side, the bipolar coil L_1 performs as a magnetic dipole and the magnetic flux excited by L_1 passes through the compensated coil L_{f1}. The amount of the magnetic flux can be expressed as ψ_{1f1}.

$$\psi_{1f1} = \iint \vec{B_1} \cdot d\vec{S}_{f1} \tag{2.1}$$

where B_1 stands for the magnetic flux density and S_{f1} represents the area of the primary compensated coil L_{f1}. The compensated coil is placed in the center of the coil structure in a different layer. As a main characteristic of a magnetic dipole, the magnetic flux it excites is symmetrical in space; therefore, the amount of the magnetic flux flows into the compensated coil equals to that flows out of it. As a result, the net magnetic flux passing through L_{f1} is zero. Since ψ_{1f1} is zero, the coupling coefficient is zero so the coupling effect is eliminated.

$$k_{1f1} = \sqrt{\frac{\psi_{1f1}\psi_{f11}}{\psi_{11}\psi_{f1f1}}} = 0 \tag{2.2}$$

where ψ_{f11} is the amount of magnetic flux excited by L_{f1} passes through L_1, ψ_{11} and ψ_{f1f1} represent the amounts of their self-magnetic flux. Similarly, the net amount of magnetic flux which is excited by L_2 and passes through L_{f2} is zero so the coupling coefficient k_{2f2} is zero. Moreover, the net amount of magnetic flux which is excited by L_1 and passes through L_{f2} is zero and the net amount of magnetic flux which is excited by L_2 and passes through L_{f1} is also zero. The coupling coefficients of extra-side coils k_{1f2} and k_{2f2} are both zero. When fully aligned, the four coupling effects are eliminated. Furthermore, when misalignment between the primary side coil structure

and the secondary side coil structure occurs, the four inductance values almost do not change. Since the relative positions of the same-side coils are fixed, the same-side coupling coefficients k_{1f1} and k_{2f2} are still zero. Though the relative positions of the extra-side coils change, the extra-side coupling effects can be neglected. It is because the compensated coil inductance values are multiple times smaller than the main coil inductance values and the air gap between the main coil and compensated coil is considered large when compared with the coil dimensions. Additionally, the coupling coefficient k_{f1f2} can be minimized to a negligible level by three-dimensional FEA tool when fully aligned, which will be discussed in the next section. When misalignment occurs, k_{f1f2} will be further decreased because the relative positions of the compensated coils change.

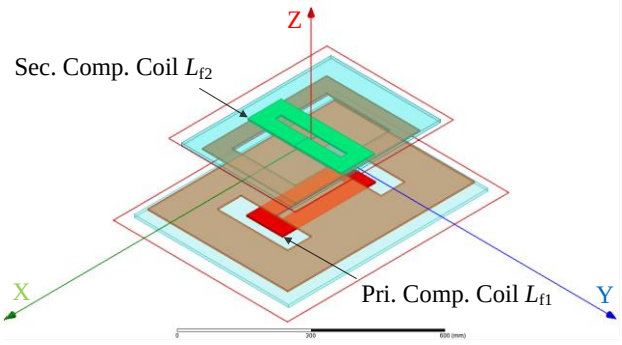

(a) Overview.

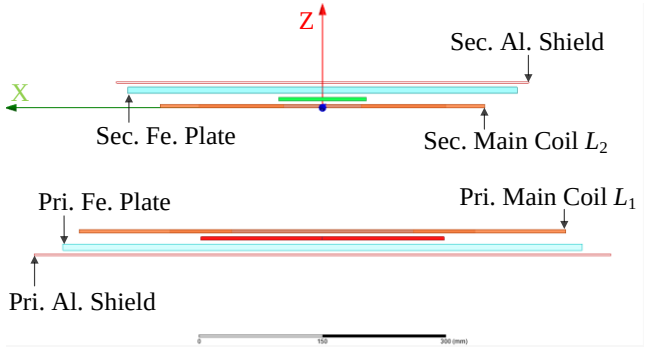

(b) Side view.

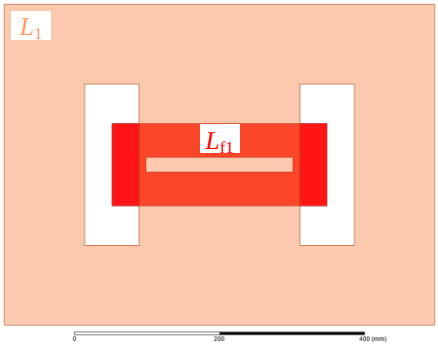

(c) Primary coils.

Figure 2.2: Proposed Coil Structures.

The five extra coupling coefficients are either eliminated or minimized to a negligible level, so the following analysis will be only based on the main coupling coefficient k between L_1 and L_2. The input DC voltage is converted to a square wave voltage of a designed frequency and enters into the primary resonant tank, where the voltage and its resulting current resonate at the resonant frequency. The resonant tank also serves as a filter and almost all high-frequency components are filtered out. Therefore, first harmonic analysis (FHA) is applied in analyzing the double-sided LCC compensation topology. Here v_{ac} in (2.3) refers to the fundamental component of the square wave voltage. Furthermore, the battery pack is considered to be a constant voltage source when designing the circuit. Since the output power is constant, the battery pack is modeled as a load resistor R_L in (2.4). The root mean square (rms) output current of the double-sided LCC compensation topology is constant once the input voltage is fixed. Therefore, the load resistor can be converted equivalently to R_{eq} at the input side of the rectifier [17].

$$v_{ac} = \frac{2\sqrt{2}}{\pi} V_{in} \angle 0^{\circ} \tag{2.3}$$

$$R_L = \frac{V_{out}^2}{P_{out}} \tag{2.4}$$

$$R_{eq} = \frac{8}{\pi^2} R_L = \frac{8}{\pi^2} \cdot \frac{V_{out}^2}{P_{out}} \tag{2.5}$$

In Figure 2.3, L_{f1} resonates with C_{f1} and as a result, i_1 is constant once v_{ac} is fixed. The induced voltage $j\omega M i_1$ can be treated as a constant voltage source for the secondary resonant tank. C_2 is chosen to compensate L_2 such that the series impedance of L_2 and C_2 is equal to that of L_{f2}. L_2 and C_2 resonate with C_{f2}. Therefore, the output current i_{f2} is also constant, which is desired for battery charging.

$$\omega L_{f1} - \frac{1}{\omega C_{f1}} = 0 \tag{2.6}$$

$$\omega L_2 - \frac{1}{\omega C_2} - \frac{1}{\omega C_{f2}} = 0 \tag{2.7}$$

$$i_{f2} = \frac{k\sqrt{L_1 L_2}v_{ac}}{j\omega L_{f1} L_{f2}} = \frac{2\sqrt{2}}{\pi} \cdot \frac{k\sqrt{L_1 L_2}V_{in}}{\omega L_{f1} L_{f2}} \angle -90^{\circ} \tag{2.8}$$

$$i_1 = \frac{v_{ac}}{j\omega L_{f1}} = \frac{2\sqrt{2}}{\pi} \cdot \frac{V_{in}}{\omega L_{f1}} \angle -90^{\circ} \tag{2.9}$$

As can be seen from equation (2.9), the output current i_{f2} lags the input voltage v_{ac} by 90°. Therefore, the voltage v_o in Figure 2.3, which is defined as the voltage at the input side of the rectifier also lags v_{ac} by 90°. Due to the symmetry of the double-sided LCC compensation network, L_{f2} resonates with C_{f2} while L_1 and C_1 are combined to resonate with C_{f1}.

$$\omega L_{f2} - \frac{1}{\omega C_{f2}} = 0 \tag{2.10}$$

$$\omega L_1 - \frac{1}{\omega C_1} - \frac{1}{\omega C_{f1}} = 0 \tag{2.11}$$

By substituting equations (2.6), (2.7), (2.10), and (2.11) into the impedance equations, the secondary side impedance Z_{sec}, the reflected impedance Z_{refl}, and the input impedance Z_{in} can be simplified as:

$$Z_{sec} = j\omega L_2 + \frac{1}{j\omega C_2} + \frac{1}{j\omega C_{f2}} \| \left(j\omega L_{f2} + R_{eq} \right) = \frac{\omega^2 L_{f2}^2}{R_{eq}} \tag{2.12}$$

$$Z_{refl} = \frac{-j\omega M i_2}{i_1} = \frac{\omega^2 M^2}{Z_{sec}}, M = k\sqrt{L_1 L_2} \tag{2.13}$$

$$Z_{in} = j\omega L_{f1} + \frac{1}{j\omega C_{f1}} \| \left(j\omega L_1 + \frac{1}{j\omega C_1} + Z_{refl} \right) = \frac{\omega^2 L_{f1}^2 L_{f2}^2}{M^2 R_{eq}} \tag{2.14}$$

where M in equation (2.13) represents the mutual inductance between L_1 and L_2. In this lossless analysis, the input power equals to the output power. Therefore, the expression of the system power is given by

$$P_{\text{in}} = P_{\text{out}} = \left|\frac{V_{\text{AC,RMS}}}{Z_{\text{in}}}\right| \cdot V_{\text{AC,RMS}} = \frac{8k\sqrt{L_1 L_2}V_{\text{in}}V_{\text{out}}}{\pi^2 \omega L_{\text{f1}} L_{\text{f2}}} \tag{2.15}$$

The voltage at the input side of the rectifier v_o, the input current i_{f1}, and the current in the secondary main coil i_2 can be written as

$$v_{\text{o}} = i_{\text{f2}} \times R_{\text{eq}} = \frac{2\sqrt{2}}{\pi} V_{\text{out}} \angle -90^{\circ} \tag{2.16}$$

$$i_{\text{f1}} = -\frac{k\sqrt{L_1 L_2}v_{\text{o}}}{\text{j}\omega L_{\text{f1}} L_{\text{f2}}} = \frac{2\sqrt{2}}{\pi} \cdot \frac{k\sqrt{L_1 L_2}V_{\text{out}}}{j\omega L_{\text{f1}} L_{\text{f2}}} \angle 0^{\circ} \tag{2.17}$$

$$i_2 = -\frac{v_o}{\text{j}\omega L_{\text{f2}}} = \frac{2\sqrt{2}}{\pi} \cdot \frac{V_{\text{out}}}{\omega L_{\text{f2}}} \angle 0^{\circ} \tag{2.18}$$

From equations (2.3), (2.9), (2.16), and (2.17), it is obvious that v_{ac} is in phase with i_{f1} and v_o is in phase with i_{f2}. Zero phase angle (ZPA) is achieved and no reactive power is needed from the power source. Moreover, v_{ac} leads v_{o} by 90° and the energy resonates between the primary side and secondary side back and forth.

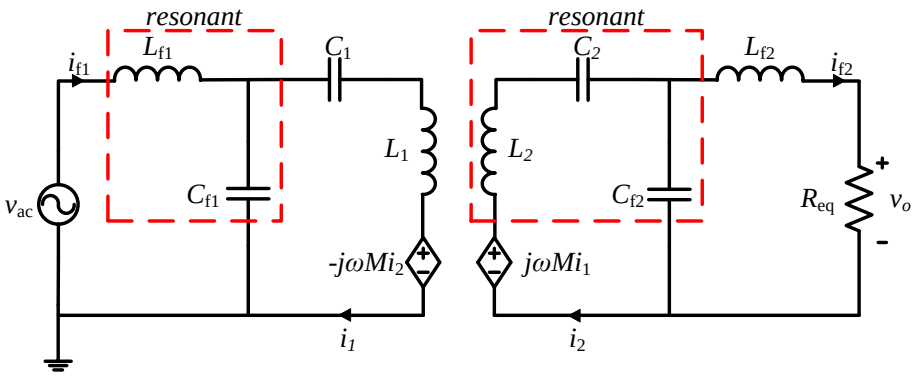

Figure 2.3: Resonant conditions in double-sided LCC compensation topology.

2.3 Design Procedures

1. Main Coil Simulation

Based on equation (2.15), the coupling coefficient k between the main coils L_1 and L_2 is closely related to the power transfer ability of a wireless power transfer system with the double-sided LCC compensation topology. The value of k depends on the coil geometry. Therefore, once the dimensions of the coils are fixed, it is preferred to maximize k by changing the coil widths in both the primary and the secondary sides. Since the application is for passenger electric vehicles, the space is quite limited on the vehicle. So, the receiving coil installed on the car is better to be smaller than the transmitting coil placed on the ground. Figure 2.4(a) shows the overview of the proposed main coil structure. We decide to choose the dimension of the transmitting coil at the primary side as "600 mm*450 mm*4 mm" and that of the receiving coil at the secondary side as "400 mm*300 mm*4 mm". Ferrite plates and aluminum shields are used for magnetic shielding. They are also made successively larger to provide the needed shielding effects. The primary side ferrite plate has a dimension of "640 mm*496 mm*8 mm" while the secondary is "480 mm*352 mm*8 mm". Aluminum shields are modelled with a primary dimension of "711.2 mm*558.8 mm*2 mm" and a secondary dimension of "508 mm*406 mm*2 mm". As shown in Figure 2.4(a), there are two design variables: the primary coil width and secondary coil width. By varying the two variables, the coupling coefficient k can be maximized. In our case, k_{max} is 0.1764 with the primary coil width of 112 mm and the secondary coil width of 48 mm. Figure 2.4(b) shows the simulation results.

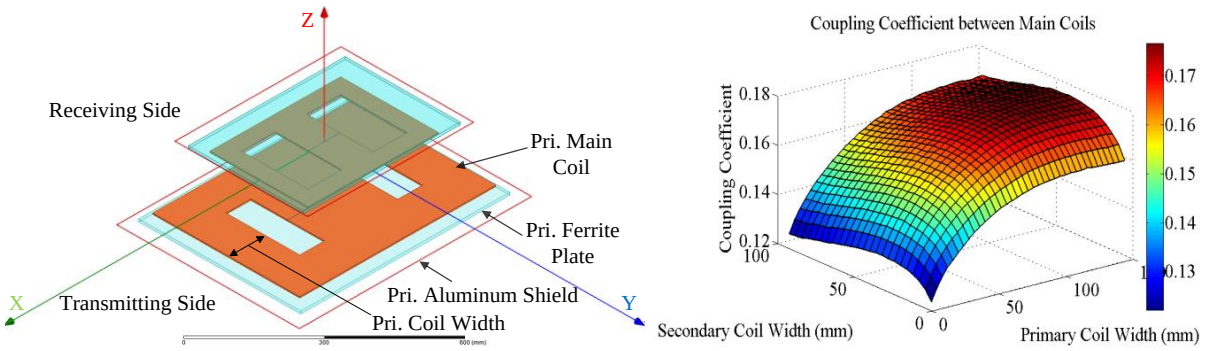

(a) (b)

Figure 2.4: (a) Overview of the main coil structure (b) Coupling coefficient *k* with different coil widths.

2. Main Coil Winding and Measurement

Two design requirements must be met: (1) the designed resonant frequency is 85 kHz and (2) the maximum efficiency is achieved at the desired output power. Additionally, there are eight components in the double-sided compensation topology. If each component has a little variance from the designed value, it will be hard to meet the two requirements at the same time. Therefore, it is highly desirable to build and measure each component right after simulation

3. Optimization of L_{f1} and L_{f2} at Maximum Efficiency

According to equation (2.15), once the resonant frequency, the system power, the main coupling coefficient, and the inductance values of the main coils are determined, the product of the compensated coil inductance values is fixed. A number of combinations could contribute to the same product and it is desired to optimize the values based on the efficiency curve of the system. The system is required to achieve the highest efficiency at the desired output power and the compensated inductance values can be optimized at that point. Once the output power is fixed, the system efficiency is determined by the power loss, which is closely related to the equivalent series resistance (ESR) of each component. The ESRs of the inductors can be

calculated by their quality factors and inductance values and the ESRs of the capacitors rest with their dissipation factors. We can write expressions for the ESRs as

$$R_1 = \frac{\omega L_1}{Q_1}, R_2 = \frac{\omega L_2}{Q_2}, R_{f1} = \frac{\omega L_{f1}}{Q_{f1}}, R_{f2} = \frac{\omega L_{f2}}{Q_{f2}} \tag{2.19}$$

$$R_{C1} = DF \cdot \left|\frac{1}{j\omega C_1}\right|, R_{C2} = DF \cdot \left|\frac{1}{j\omega C_2}\right|, R_{Cf1} = DF \cdot \left|\frac{1}{j\omega C_{f1}}\right|, R_{Cf2} = DF \cdot \left|\frac{1}{j\omega C_{f2}}\right| \tag{2.20}$$

where Q_1, Q_2, Q_{f1}, and Q_{f2} stand for the quality factors of L_1, L_2, L_{f1}, and L_{f2} respectively.Q_1 and Q_2 can be measured by LCR meters since they have already been built in the last step. Q_{f1} and Q_{f2} can be approximated at 200 based on their inductance values, which are multiple times smaller than the main coil inductance values. *DF* is the dissipation factor of the capacitors. Once the compensated inductance values are given, the capacitance values can be calculated by equations (2.6), (2.7), (2.10), and (2.11). In this chapter, 5PT series polypropylene and foil resonant power supply capacitors from Electronic Concepts are used and its *DF* is claimed to be 0.05%.

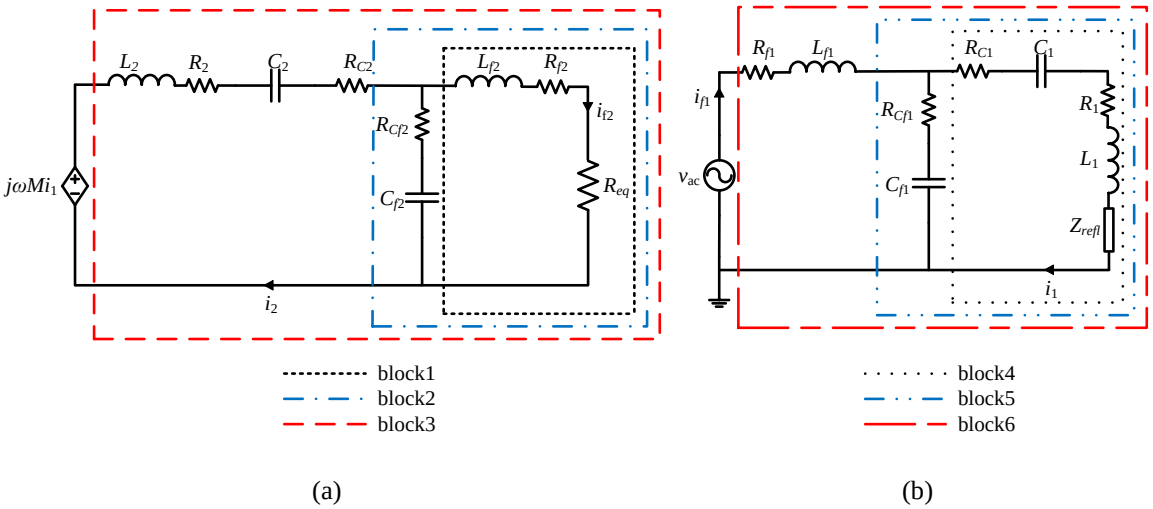

Figure 2.5: Circuit diagrams with ESRs: (a) Secondary side and (b) Primary side.

Figure 2.5(a) and (b) gives the circuit diagram with ESRs added into the system. The system is divided into primary side circuit and the secondary side circuit. Therefore, the efficiency analysis can be done separately. The overall efficiency is the product of primary side circuit efficiency η_{pri} and secondary side efficiency η_{sec}. On the secondary side, η_{sec} is the product of η_{s1}, η_{s2}, and η_{s3}. As shown in Figure 2.5(a), η_{s1} refers to efficiency of block 1, which is the ratio of the real power obtained by the load over the real power entering into block 1; η_{s2} is defined as the efficiency of block 2, which is the ratio of the real power entering into block 1 over the real power absorbed by block 2; η_{s3} is efficiency of block 3, which is the ratio of the real power absorbed by block 2 over the real power transferred from the primary side of the circuit. The expressions of η_{s1}, η_{s2}, and η_{s3} are given by

$$\begin{aligned}
\eta_{\text{s1}} &= \frac{R_{\text{eq}}}{R_{\text{eq}} + R_{\text{f2}}} \\
\eta_{\text{s2}} &= \frac{\left| R_{\text{Cf2}} + \dfrac{1}{j\omega C_{\text{f2}}} \right|^2 \cdot \left(R_{\text{eq}} + R_{\text{f2}} \right)}{\left| R_{\text{Cf2}} + \dfrac{1}{j\omega C_{\text{f2}}} \right|^2 \cdot \left(R_{\text{eq}} + R_{\text{f2}} \right) + \left| R_{\text{eq}} + R_{\text{f2}} + j\omega L_{\text{f2}} \right|^2 \cdot R_{\text{Cf2}}} \\
\eta_{\text{s3}} &= \frac{\text{Re}(Z_{\text{block2}})}{\text{Re}(Z_{\text{block2}}) + R_2 + R_{\text{C2}}}
\end{aligned} \tag{2.21}$$

where Z_{block2} and Z_{sec} are the impedances of block 2 and the secondary side circuit. Similarly, on the primary side, η_{pri} equals to the product of η_{p1}, η_{p2}, and η_{p3}. In Figure 2.5(b), η_{p1} is efficiency of block 4 and is given by the ratio of the real power transferred to the secondary side circuit over the real power going through block 4; η_{p2} is the efficiency of block 5 and expressed as the ratio of the real power going through block 4 over the real power received by block 5; η_{p3} is the efficiency of block 6 and described as the ratio of the real power received by block 5 over the real power sent by the power source. We derive expressions of η_{p1}, η_{p2}, and η_{p3} as

$$\eta_{p1} = \frac{\mathrm{Re}\left(Z_{\mathrm{refl}}\right)}{\mathrm{Re}\left(Z_{\mathrm{refl}}\right) + R_{C1} + R_1}$$

$$\eta_{p2} = \frac{\left|R_{Cf1} + \frac{1}{j\omega C_{f1}}\right|^2 \cdot \left[R_{C1} + R_1 + \mathrm{Re}\left(Z_{\mathrm{refl}}\right)\right]}{\left|R_{Cf1} + \frac{1}{j\omega C_{f1}}\right|^2 \cdot \left[R_{C1} + R_1 + \mathrm{Re}\left(Z_{\mathrm{refl}}\right)\right] + \left|R_1 + R_{C1} + j\omega L_1 + \frac{1}{j\omega C_1} + Z_{\mathrm{refl}}\right|^2 \cdot R_{Cf1}} \quad (2.22)$$

$$\eta_{p3} = \frac{\mathrm{Re}\left(Z_{\mathrm{block5}}\right)}{\mathrm{Re}\left(Z_{\mathrm{block5}}\right) + R_{f1}}$$

where Z_{refl} is the reflected impedance from the secondary side circuit and Z_{block5} is the impedance of block 5. We can plot the efficiency over equivalent resistance curve by applying equations (2.21) and (2.22) in MathCAD. By adjusting the inductance values of L_{f1} and L_{f2}, the efficiency can be maximized at the desired equivalent resistance. For our case, the desired output power is 3.0 kW and the battery pack is 300 volts, therefore, the efficiency is maximized at 24.32 ohms. Figure 2.6 gives the efficiency curve obtained from MathCAD and the desired inductance values are determined as L_{f1}= 46μH and L_{f2}= 38μH.

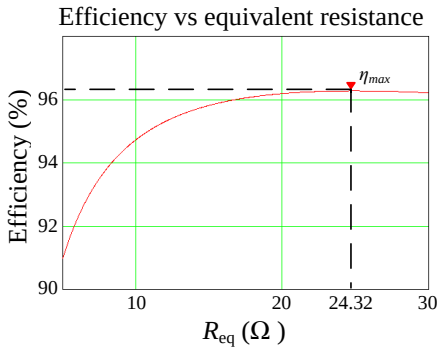

Figure 2.6: Efficiency over equivalent resistance curve.

4. Maxwell Simulation for L_{f1} and L_{f2}

As analyzed in the previous section, a unipolar compensated coil is preferred in a coil structure with bipolar main coils. In order to further decrease the coupling effects between the main coil and the compensated coil, it is more desired to place the compensated coil in the region

with weaker magnetic field densities. By substituting L_{f1} and L_{f2} into (2.8) and (2.18), the currents flowing through L_1 and L_2 can be determined and set as the excitation currents in the Maxwell model. Vacuum boxes are built up at the expected positions of the compensated coils, which are shown in Figure 2.7(a). Figure 2.7(b) gives the simulation results of magnetic flux densities in the vacuum boxes. Clearly, the magnetic field is weaker in the central areas of the two main coils, which are circled by the dashed lines in Figure 2.7(b). The compensated coils should be placed in those areas. With the desired inductance values, the compensated coils are built and simulated in ANSYS MAXWELL.

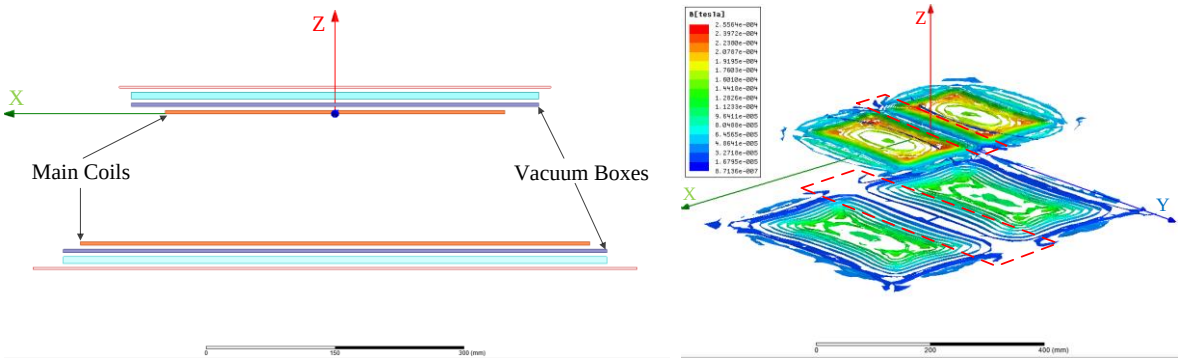

(a) (b)

Figure 2.7: (a) Side view of the coil structure with vacuum boxes; (b) Magnetic field densities of the vacuum boxes.

The compensated coils with the desired values are placed in the system as shown in Figure 2.8(a) and the coupling coefficient k_{f1f2} is 0.05, which is good enough for the experiment. However, it can be further optimized. Since Figure 2.7(b) indicates a larger area with weaker magnetic flux density on the primary side, so the primary compensated coil has enough area to be placed. By rotating the primary compensated coil from 0° to 180° as shown in Figure 2.8(b), the lowest coupling case is achieved.

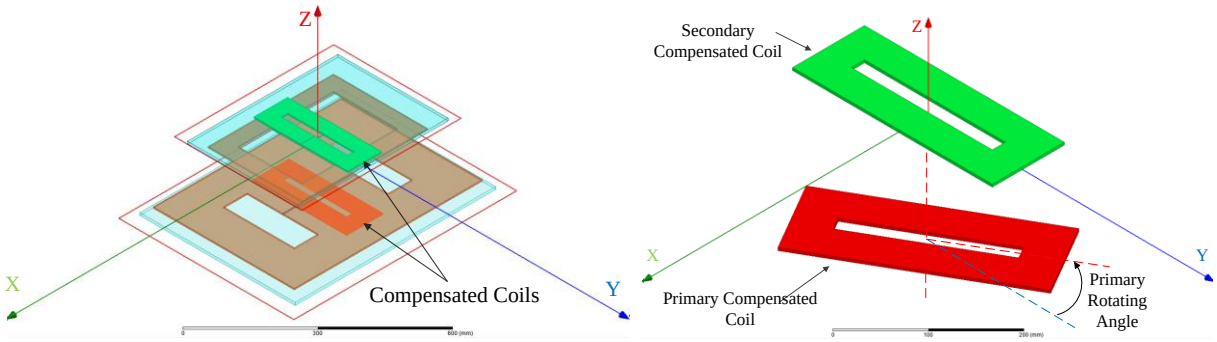

(a) (b)

Figure 2.8: (a) Coil structure with compensated coil integrated into the system and (b) Rotating the primary compensated coil.

Figure 2.9(a) shows the coupling coefficient k_{f1f2} of the compensated coils and the same-side coupling coefficients k_{1f1} and k_{2f2}. It is obvious that k_{f1f2} is minimized as 0.04 at 90° rotating angle while the same-side coupling coefficients are almost equal to zero with the angle rotating. Figure 2.9(b) demonstrates that the self-inductance values of the two compensated coils keep almost constant with the angle rotating.

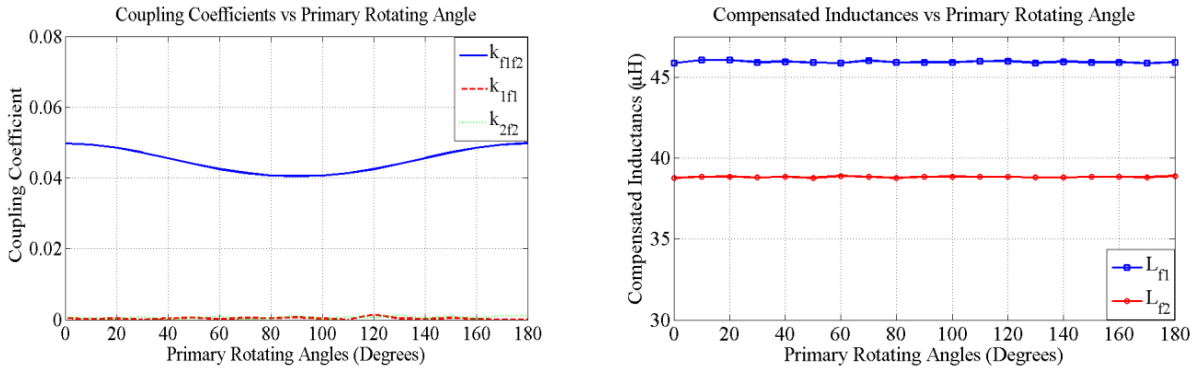

(a) (b)

Figure 2.9: (a) Coupling coefficients with rotating angles (b) Compensated inductance values with rotating angles.

5. Compensated Coil Winding and Measurement

With the parameters provided by MAXWELL simulation, the compensated coils are wound and measured. Again, in order to make the resonate frequency at 85 kHz and the efficiency maximized at the desired output power, capacitance values need to be recalculated

with the measured results of L_1, L_2, L_{f1}, and L_{f2} through equations (2.6) , (2.7), (2.10), and (2.11). The capacitance values calculated in this step only slightly vary from those calculated in step 3. Therefore, the efficiency will not be affected.

6. Capacitor Tuning for Zero Voltage Switching

Another inherent characteristic of the double-sided LCC compensation topology is to help with zero voltage switching (ZVS) of the power electronic devices, which are the four MOSFETs of the full-bridge converter in this chapter. ZVS not only reduces the switching noise of the MOSFETs, but also helps minimize the switching losses. In this chapter, zero voltage turning on of the MOSFETs is achieved. We define the instantaneous current value when MOSFETs S_1 and S_4 are turned off as I_{OFF}. I_{OFF} must

$$I_{OFF} > \frac{2C_{OSS}V_{in,max}}{t_{dead}} \tag{2.23}$$

so that the current value is large enough to charge the parasitic output capacitors of S_1 and S_4 and discharge the parasitic output capacitors of S_2 and S_3 [14]. In equation (2.23), C_{oss} is the parasitic output capacitance of the MOSFET, $V_{in,max}$ is the maximum value of the input voltage, and t_{dead} is the dead time. In this chapter, 1200 V C2M0025120D Silicon Carbide (SiC) Power MOSFETs from CREE are used. Its output parasitic capacitance is approximately 400 pF, $V_{in,max}$ is 330 volts, and t_{dead} is 200 ns. Therefore, I_{OFF} should be larger than 1.32 A. During the dead time, the body diodes of the MOSFETs clamp the voltages over the parasitic output capacitors. Therefore, the parasitic output capacitors of S_1 and S_4 are charged to input voltage value and the parasitic output capacitors of S_2 and S_3 are discharged to almost 0 V. So, when S_2 and S_3 are turned on right after the dead time, the voltages across them are almost zero and zero voltage turning on of S_2 and S_3 is achieved. Similarly, zero voltage turning on of S_1 and S_4 is achieved after one half cycle. Based on [14], capacitor C_2 is the best choice to tune in order to achieve ZVS. It is demonstrated

that C_2 is tuned to be 8%~11% larger than the calculated value of C_2 in the last step. Once the above six steps are done, it is ready to build the wireless charging system and conduct experiments. The design procedures can be summarized in the flowchart as shown in Figure 2.10. In particular, the two design criterions of $k_{\max}$ and k_{f1f2} are the authors' experienced values, which are the worst cases to make the system work as well.

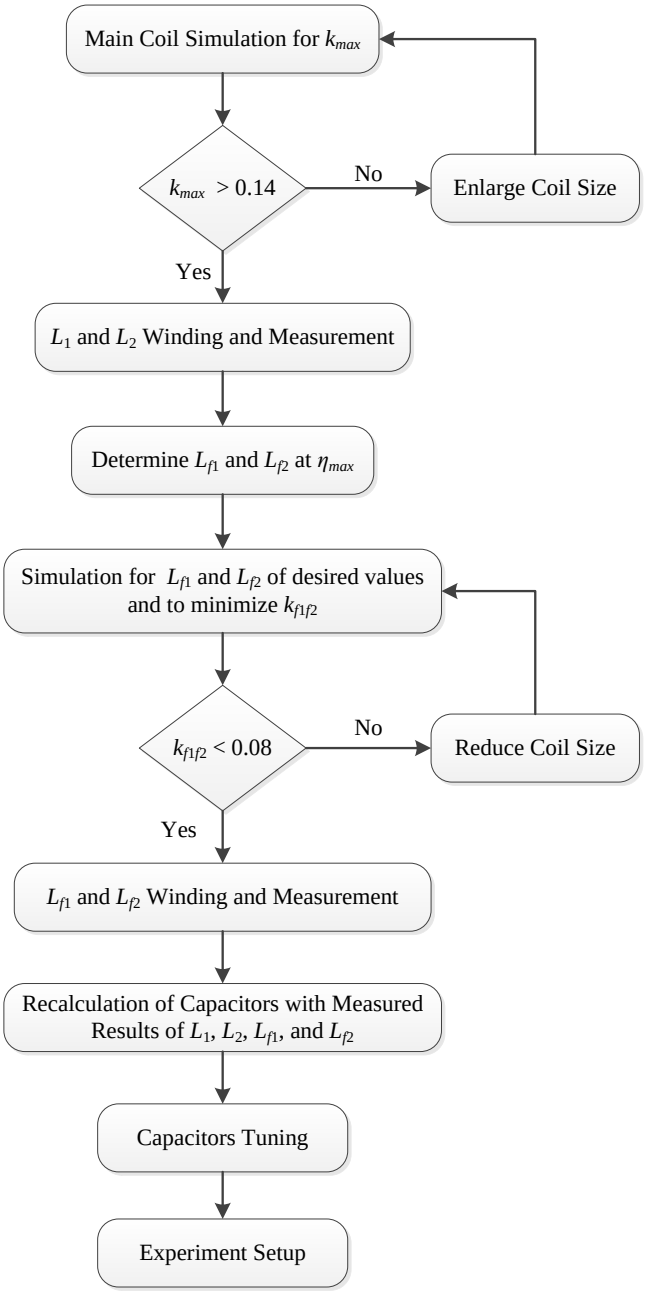

Figure 2.10: Design flowchart.

2.4 Experiment

The system specifications are given in Table 2.1. Since the resonant frequency is fixed at 85 kHz, AWG-38 copper wires are selected to minimize the skin effect. The input voltage is 330 V, the output battery pack voltage is 300 V, and the output power is 3.0 kW. Therefore, 800-strand AWG-38 litz wires are used. The ferrite is Ferroxcube 3C95, which has outstanding performance at frequencies below 500 kHz. Aluminum plates serve as the electric shielding. The air gap is 150 mm due to the ground clearance of passenger cars. Based on simulations results, the main coils are built and compensated coils are integrated, which are shown in Figure 2.11(a) and (b). Figure 2.11(c) presents the whole wireless charging system. It shows that it is highly compact with the compensated coil integrated into the system. The circuit parameters are given in Table 2.2. It is convinced that there are only slight differences between the design values and the measured values.

Table 2.1: System Specifications.

Spec/Parameters	Design Value
Input Voltage	330 V
Battery Pack Voltage	300 V
Primary Main Coil Dimension	600 mm × 450 mm × 4 mm
Secondary Main Coil Dimension	400 mm × 300 mm × 4 mm
Primary Ferrite Plate Dimension	640 mm × 496 mm × 8 mm
Secondary Ferrite Plate Dimension	480 mm × 352 mm × 8 mm
Primary Shield Dimension	711 mm × 559 mm × 2 mm
Primary Shield Dimension	508 mm × 406 mm × 2 mm
Air Gap	150 mm
Main Coupling Coefficient	0.1877
Resonant Frequency	85 kHz
Maximum Output Power	3.0 kW

Table 2.2: Circuit Parameters.

Parameters	Design Value	Measured Value
Primary main coil inductance L_1	225.35 μH	222.98 μH
Secondary mail coil inductance L_2	159.45 μH	157.55 μH
Primary compensated coil inductance L_{f1}	46 μH	44.059 μH
Secondary compensated coil inductance L_{f2}	38 μH	38.04 μH
Primary resonant capacitor C_1	19.59 nF	19.853 nF
Secondary resonant capacitor C_2	31.39 nF	32.71 nF
Primary compensated capacitor C_{f1}	79.68 nF	79.69 nF
Secondary compensated C_{f2}	92.16 nF	92.36 nF

(a) (b)

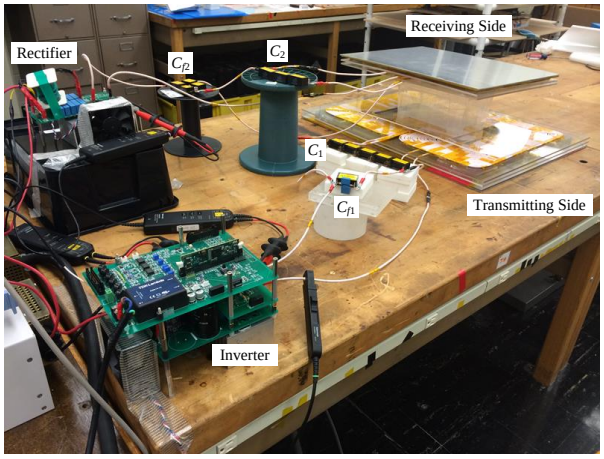

(c)

Figure 2.11: Experiment setup of (a) coils on primary side, (b) coils on secondary side, and (c) wireless charging system.

Table 2.3 compares the simulated results and measured results of the six coupling coefficients in the wireless charging system. Clearly, the measured results prove that not only are the same-side coupling coefficients k_{1f1} and k_{2f2} eliminated, but also the cross-side coupling coefficients k_{1f2} and k_{2f1}, the coupling coefficient of compensated coil k_{f1f2} are minimized to negligible levels. The maximum main coupling coefficient k is achieved at 0.1877. The measured results of k and k_{f1f2} match their simulated results since they are relatively large when compared to k_{1f1}, k_{2f2}, k_{1f2}, and k_{2f1}. The percentages of the errors between the simulated results and the measured results for k_{1f1}, k_{2f2}, k_{1f2}, and k_{2f1} are large. It is because their values are very small and only a slight misalignment will result in a big difference in results. Figure 2.12 further demonstrates that the center of the compensated coil should be aligned with the center of the main coil so that the same-side coupling coefficient is eliminated. Figure 2.13 shows how the measured coupling coefficients k_{f1f2}, k_{1f1}, and k_{2f2} vary with the compensated coils rotating. As shown in Figure 2.13(a), k_{f1f2} is minimized when the primary rotating angle equals 90° and secondary rotating angle is 0°, which verifies the simulation result in Figure 2.9(a). The measured results in Figure 2.13(b) and (c) indicate that k_{1f1} and k_{2f2} are small enough to be neglected, further confirming the proposed idea. Figure 2.14 presents the measured results of the two compensated coils. The inductance values keep constant at the designed values with the angles rotating, which also confirms the simulation results in Figure 2.9(b).

Table 2.3: Coupling Coefficients.

Coupling Coefficients	Simulated Value	Measured Value
Main Coupling Coefficient k	0.1746	0.1877
Coupling Coefficient k_{1f1} between L_1 and L_{f1}	0.00068	0.005826
Coupling Coefficient k_{2f2} between L_2 and L_{f2}	0.001118	0.012368
Coupling Coefficient k_{1f2} between L_1 and L_{f2}	≈ 0	0.006135
Coupling Coefficient k_{2f1} between L_2 and L_{f1}	≈ 0	0.002941
Coupling Coefficient k_{f1f2} between L_{f1} and L_{f2}	0.04053	0.0483

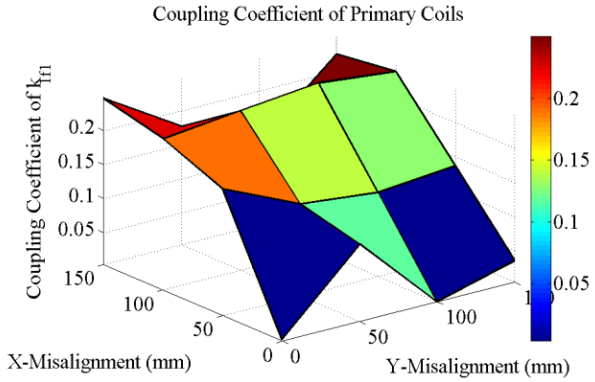

Figure 2.12: Horizontal misalignment effects on k_{1f1}.

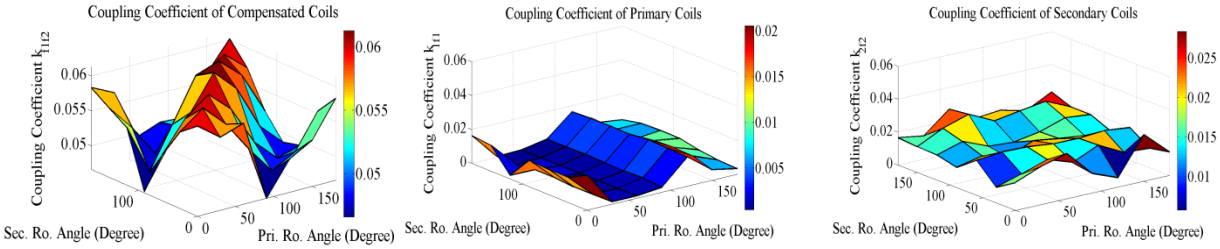

(a) (b) (c)

Figure 2.13: Coupling coefficients (a) k_{f1f2}, (b) k_{1f1}, and (c) k_{2f2} with compensated coils rotating.

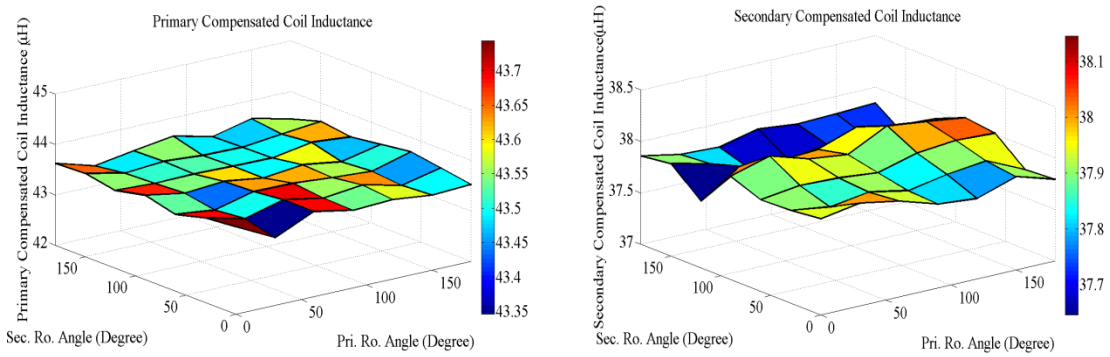

(a) (b)

Figure 2.14: Compensated inductances values (a) L_{f1} and (b) L_{f2} with the compensated coils rotating.

Figure 2.15(a) represents the waveforms of the primary resonant tank's input voltage v_{ac} and input current i_{f1}, the secondary resonant tank's output voltage v_o, and MOSFET gate-to-source voltage V_{drive}. In this chapter, the purpose of observing V_{drive} is to ensure that the gate-to-source voltage is in its maximum rating all the time since noises may appear during the experiment. Here, v_{ac} leads i_{f1} by 13.4° and the turn-off current I_{OFF} is approximately 4.5 A, which is much larger than 1.32 A and sufficient for charging and discharging the parasitic output capacitors. Figure 2.15(b) gives the power characteristics of the wireless charging system at the maximum output power. When fully aligned, the system is able to deliver 3.0 kW output power at DC-DC efficiency as high as 95.5%. Further experiments on misalignments are also conducted in the Y-direction, X-direction, and Z-direction separately. Figure 2.16 give the respective waveforms. Since the input voltage and the battery pack voltage are fixed at 330 V and 300 V, respectively, the waveforms of v_{ac} and v_o remain the same. However, the waveform of i_{f1} gradually deviates from its original waveform as shown in Figure 2.15(a). When misalignments in different directions occur, the main coupling coefficient k decreases and the output power goes down, as indicated by equation (2.15). Therefore, the rms value of i_{f1} becomes smaller. Moreover, the mutual inductance M between the main coils decreases and as a result, both the reflected impedance Z_{refl} and input impedance Z_{in} change. The input phase angle between v_{ac} and i_{f1}

increases, which causes the turn-off current I_{OFF} to increase and the high-order harmonics components in i_{f1} to rise. The decreased rms value of i_{f1}, the increased turn-off current value, and high-order harmonics components in i_{f1} result in the waveform distortions when misalignments occur. Figure 2.16(a) shows the waveforms when the Y-direction misalignment is 150 mm. Since k and M are still comparable to their original values when fully aligned, the waveform distortion of i_{f1} is low. However, when k and M further decreases, the waveform distortion turns high, as shown in Figure 2.16(b) and (c). Here, Z-direction misalignment is 50 mm means air gap is increased from 150 mm to 200 mm.

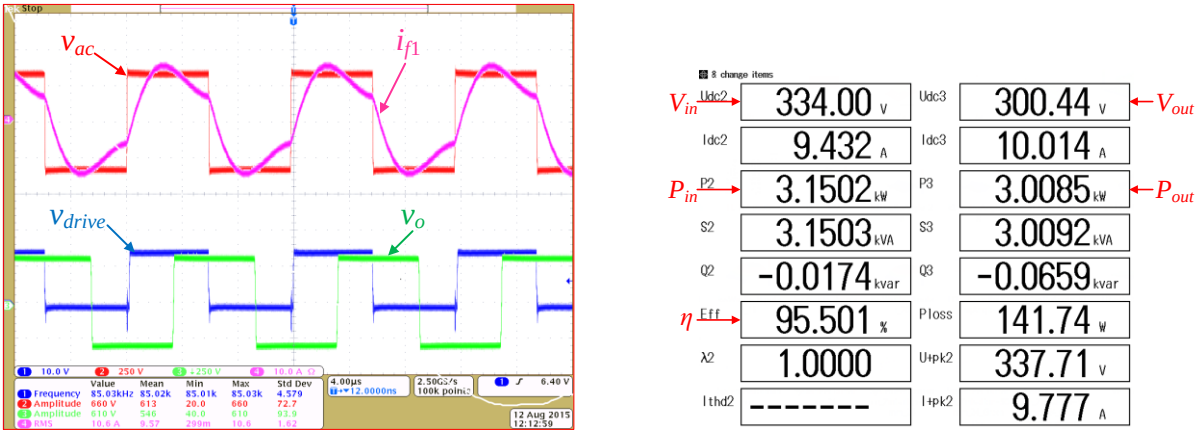

(a) (b)

Figure 2.15: (a) Waveforms when fully aligned; (b) System power characteristics with V_{in} = 334 V, V_{out} = 300V, P_{in} =3.15 kW, P_{out} =3.01 kW, and η = 95.5%.

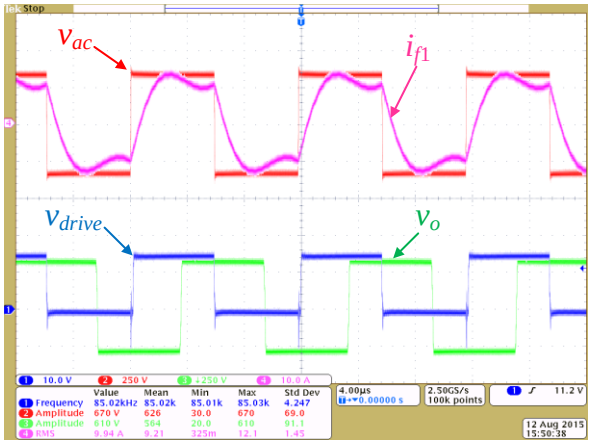

(a)

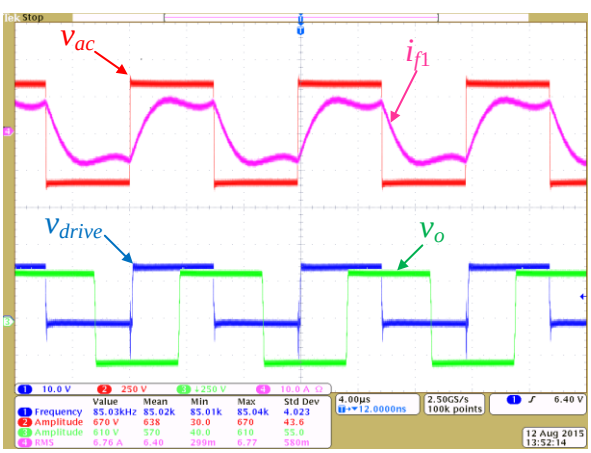

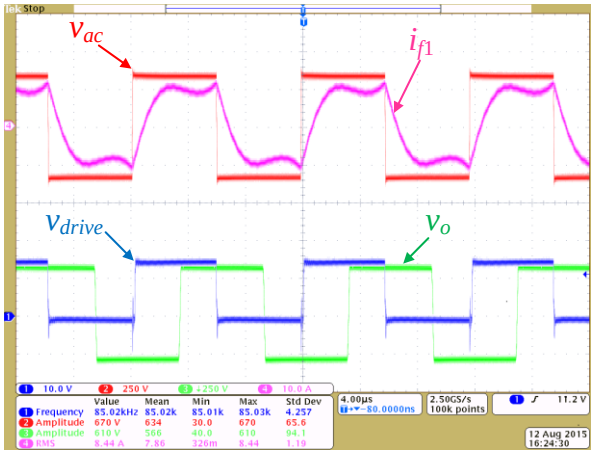

(b) (c)

Figure 2.16: Waveforms when misalignment in different directions occurs: (a) Y-direction misalignment is 150 mm; (b) Z-direction misalignment is 50 mm; (c) X-direction misalignment is 100mm.

All the experimental results are given by Figure 2.17. The solid line in Figure 2.17(a) shows the experimental result when the system is fully aligned. It shows great consistency with the simulated efficiency curve in Figure 2.6 and the system efficiency is peaked at the maximum output power. The dash-dot line presents the result of the experiment on Z-direction misalignment. The system can transfer 1.76 kW at efficiency of 94.4% when the air gap increases to 200 mm. The solid line with circles gives the system performance in X-direction misalignment. The system delivers 1.57 kW power at an efficiency of 93.8% when the X-

direction misalignment increases to 100 mm. The performance is a little weaker and as a result, it is highly recommended to make X-direction compliant with the front-rear direction of the car since it is more convenient for the driver to adjust when the car is parked. The dashed and dotted lines show the system performance in the Y-direction. The system performs much better in this direction. When the misalignment even increases to 150 mm, the system can still deliver approximately 2.0 kW at an efficiency of 94.8%. This direction is better to be door-to-door direction since it is hard for drivers to adjust when the car is parked. Figure 2.17(a) indicates that when misalignment in different directions occurs, the output power drops 33.33% from the maximum output power in Y-direction, 41.33% in Z-direction, and 47.69% in X-direction. It is because the main coupling coefficient *k* decreases and other component values remain almost the same, as it is indicated by equation (2.15). Figure 2.17(b) shows how the measured main coupling coefficient *k* decreases as misalignment occurs. When the misalignment increases to 150 mm in Y-direction, *k* decreases to 0.1244, or 33.72% drop from its original value (*k* = 0.1877); when the misalignment increases to 50 mm in Z-direction, *k* goes down to 0.1045, or 44.33% drop; when the misalignment increases to 100 mm in X-direction, *k* declines to 0.1, or 46.72% drop. The differences in the respective dropped percentages between the output power and the main coupling coefficient are caused by the differences in inductance values when misalignment occurs. However, the differences are within 3%, indicating the inductance values only slightly change. Figure 2.17(a) and (b) not only verify equation (2.15), but also validate that extra coupling coefficients are eliminated or minimized to a negligible level. Figure 2.17(c) describes how the efficiency varies with misalignments in different directions. It turns out that the efficiency decreases as the misalignment increases. Furthermore, the efficiency curve in Figure 2.17(c) shows fairly good consistency with the main coupling coefficient curve in Figure

2.17(b). Experimental results demonstrate the wireless charging system with the new integration method not only has the dual advantage of compactness and high efficiency, but also eliminates the extra coupling effects or minimize them to a negligible level, which greatly simplifies the system analysis and design.

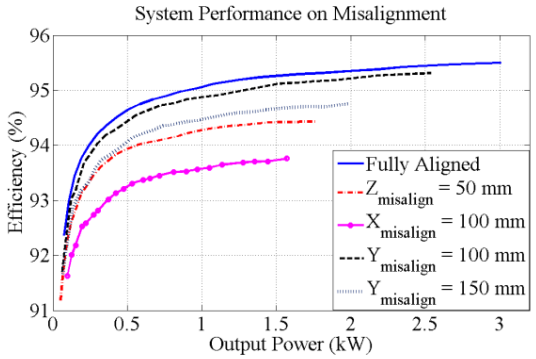

(a)

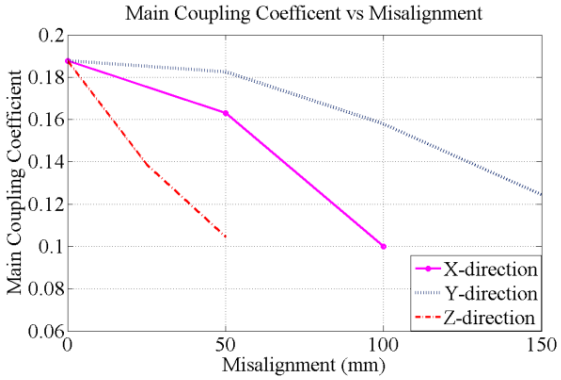

(b)

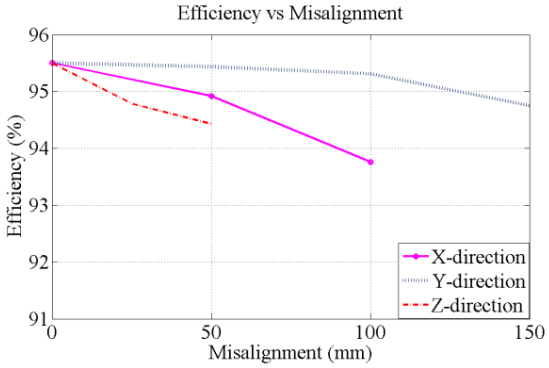

(c)

Figure 2.17: Experimental results on misalignments in different directions: (a) Efficiency vs output power; (b) Main coupling coefficient vs misalignment; and (c) Efficiency vs misalignment.

2.5 Conclusions

This chapter proposes a new integrated method of a wireless charging system using double-sided LCC compensation topology. With the compensated coils integrated into the main coil structure, the system becomes much more compact. The proposed compensated coil design further eliminate or minimize the extra coupling effects to a negligible level, making it more

straightforward to design a wireless charging system using the double-sided LCC compensation topology. The detailed design procedures to improve system efficiency are also introduced. Both the 3D FEA simulation results and the experimental results verify the proposed method. The compact and highly efficient wireless charging system is able to deliver 3.0 kW at a DC-DC efficiency of 95.5% with an air gap of 150 mm when fully aligned.

This chapter is based on the following published paper. As the first author, I proposed and analyzed the coil structure, developed the design procedures, conducted the experiment, and drafted the paper.

T. Kan, T. D. Nguyen, J. C. White, R. K. Malhan, and C. Mi, "A new integration method for an electric vehicle wireless charging system using LCC compensation Topology: Analysis and Design," *IEEE Trans. Power Electron*., vol. 32, no.2, pp. 1638–1650, Feb. 2017

Chapter 3

Integrated Coil Design in EV Unipolar Coils

3.1 Introduction

This chapter extends the work of Chapter 2 by analyzing and demonstrating an LCC compensation topology that is compact and efficient, and importantly, compatible with unipolar coil structures. Here, the coil structures are studied through ANSYS MAXWELL, in which the aspect ratio of the compensated coil is used as an important design specification to minimize the extra cross-side coupling coefficient. A wireless charging system with the proposed integration method is built to transfer 3.09 kW power with a DC-DC efficiency of 95.49%. Furthermore, the experimental results in Chapter 2 and this chapter are compared, and the results show that the wireless charging system with the proposed integration method has a competitive performance in fully-aligned condition and under door-to-door misalignment, while achieving superior performance under front-to-rear and vertical misalignment.

3.2 Analysis

Integration makes the wireless charging system using LCC compensation topology more compact and the design of the system simpler. Figure 3.1 gives the overview and cross-sectional side view of a coil structure with integrated compensated coils. On each side of the coil structures, there are four orderly arranged layers: the main coil, the compensated coil, a ferrite plate, and an aluminum shield. In particular, the main coils are unipolar and the compensated coils are bipolar. The power is transferred wirelessly from the primary side to the secondary side via the magnetic field generated by the two main coils. The ferrite plates and the aluminum

shields provide sufficient magnetic shielding so that the generated magnetic field is concentrated within the coil structures. The compensated coils are not designed to transfer power, but tune the magnitudes of currents in the main coils so that a high efficiency will be achieved. Thus, the two compensated coils are preferred to have the lowest coupling effect between themselves and minimal interference with the two main coils.

In the newly proposed method, a bipolar compensated coil is integrated into a unipolar main coil, which is shown in Figure 3.1. We take primary coils as an example. The net magnetic flux Ψ_{f11}, which is generated by the primary compensated coil L_{f1} and passing through the main coil L_1, can be expressed as

$$\Psi_{f11} = \iint \overrightarrow{B_{f1}} \cdot d\vec{S}_1 \tag{3.1}$$

where, B_{f1} is magnetic flux density and dS_1 is the surface element at the primary main coil. The magnetic flux, generated by a bipolar coil, flows from one of its magnetic dipoles to the other. The net magnetic flux is zero since the amount of magnetic flux enters into L_1 equals to the amount of magnetic flux flows out of it. Therefore, the coupling effect between L_1 and L_{f1} is eliminated and the coupling coefficient k_{1f1} is zero. Similarly, the net magnetic flux Ψ_{f12}, generated by L_{f1} and passing through L_2 is zero and the coupling coefficient k_{2f1} between L_2 and L_{f1} is zero. The integration eliminates the same-side coupling coefficients and the cross-side coupling effects when fully aligned. Since the relative positions of the same-side coils do not change when misalignment occurs, the same-side coupling coefficients are still zero on both sides during misalignment. The relative positions of every two cross-side coils change and the cross-side coupling coefficients appear. Fortunately, the gap between every two cross-side coils is considerably large. The respective coupling coefficients are small and can be neglected at the frequency of interest, which will be verified by the experimental results in Section 3.4. The extra

cross-side coupling coefficient exists all the time and it can be minimized to a negligible level, which will be studied and verified in the later sections.

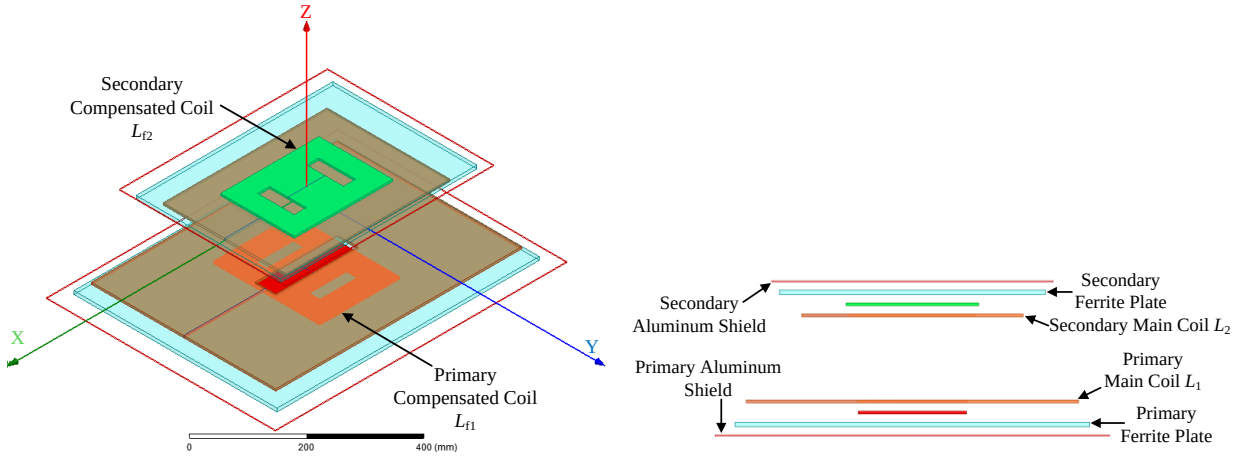

(a) (b)

Figure 3.1: (a) Overview and (b) cross-sectional view of coil structures with proposed integration method

3.3 System Design

A wireless charging system from the DC input to DC battery mainly consists of three parts: an inverter, a rectifier, and coils with compensation networks. The power loss of the wireless charging system originates from the three parts. The SiC MOSFETs are selected for the inverter while the diodes are chosen for the rectifier. Since zero voltage switching is achieved in the inverter stage, most of the power loss in the inverter and rectifier is the conduction loss of the MOSFETs and diodes, which is approximately 31W in a 3.0 kW wireless charging system. This contributes to 1% efficiency drop. Therefore, the majority of the system power loss is from the coils and compensation networks. In a wireless charging system with a double-sided LCC compensation topology, there are eight circuit components: four inductors (i.e. coils) and four capacitors. The power loss in the circuit components is determined by their equivalent series resistances (ESRs). The ESR of an inductor is determined by its quality factor, frequency, and inductance value while the ESR of a capacitor depends on its dissipation factor, frequency, and

capacitance. In resonant condition, the frequency is fixed and based on (2.6), (2.7), (2.10), and (2.11), the capacitor values are determined by the inductor values. Therefore, the design is focused on optimizing the values of the four inductors so that the system is able to achieve the highest efficiency at the desired output power. Since the power transfer replies on the coupling between the two main coils, the maximum coupling coefficient is desired within the main coil dimensions. The dimensions of the primary and secondary main coils are "600mm×450mm×4mm" and "400mm×300mm×4mm". The secondary is relatively smaller since it is installed on the vehicle. Here, the dimensions of the main coils remain the same with those in Chapter 2 for fair comparison in Section 3.5. The air gap between the two main coils is 150 mm. The coupling coefficient is closely related to the coil geometry and varies with the primary and secondary coil widths in Figure 3.2(a). It is maximized at 0.2305 when the primary coil width is 200 mm and secondary coil width is 90 mm, which is shown in Figure 3.2(b).

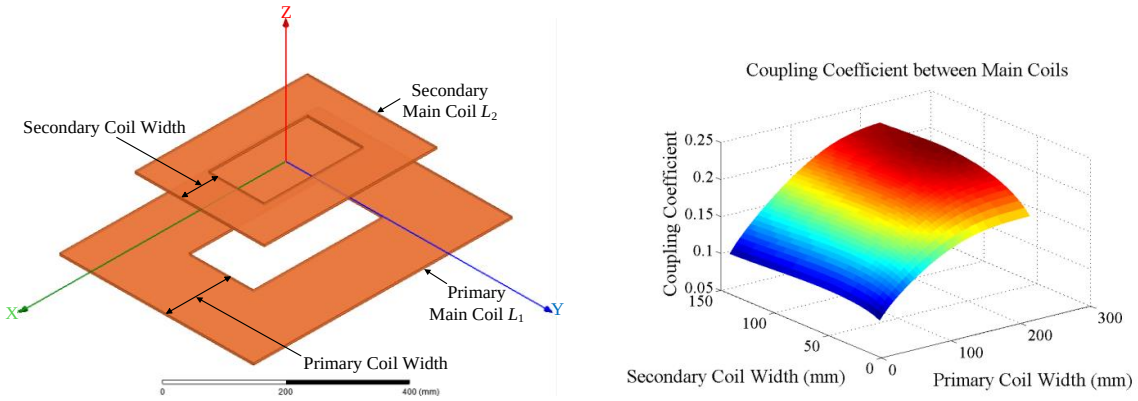

(a) (b)

Figure 3.2: (a) Design variables in main coil simulation model and (b) simulation results on main coupling coefficient.

The two main coils are wound by the same type of litz wires. The required coil widths are achieved and the turn numbers are different. The self-inductances of the main coils are determined. Based on Chapter 2, the efficiency of a wireless charging system using the double-

sided LCC compensation topology is mainly determined by the ESRs of the inductors and the capacitors. In order to achieve the highest efficiency at the desired output power, the same design procedures as in Chapter 2 are followed and Figure 3.3 presents the calculated results from MathCAD. Based on (2.5), when the output power is 3.0 kW and the battery voltage is 340 V, the equivalent load resistance is 31.23Ω. The efficiency is maximized at 97.0% in Figure 3.3. Here, the power loss from the inverter and rectifier is ignored when calculating the efficiency. The required self-inductances of the primary and secondary compensated coils are 56 μH and 43 μH, respectively.

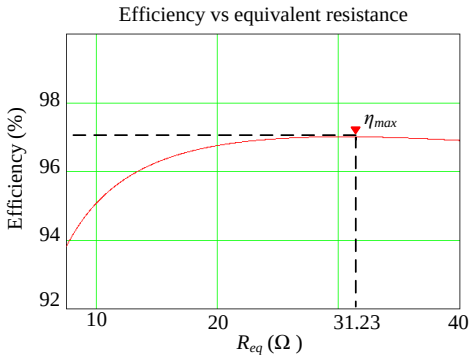

Figure 3.3: Efficiency curve.

With the required values, the compensated coils are designed by employing ANSYS MAXWELL. Since the extra cross-side coupling between the two compensated coils is unexpected from the design point of view in this chapter, the minimum extra cross-side coupling is the goal. As analyzed in Section 3.2, the bipolar coils are selected as the compensated coils and integrated into the unipolar main coil structures. Different aspect ratios of the compensated coils are studied to obtain the minimum coupling. The aspect ratio is defined as "*W*/*L*", where *W* is the length of the compensated coil in Y-direction and *L* is the length in X-direction. The magnetic flux generated by a bipolar coil is single-directional rather than isotropic. Therefore, the placement of the two compensated coils affects the coupling coefficient between them. Two

kinds of placement as shown in Figure 3.4 are studied: (1) placement I, in which the two coils are fully aligned; and (2) placement II, in which the two coils are misaligned with an angle of 90°. In addition, the areas of the primary and secondary compensated coils are approximately fixed at 50,000 mm^2 and 40,000 mm^2 in all simulation cases.

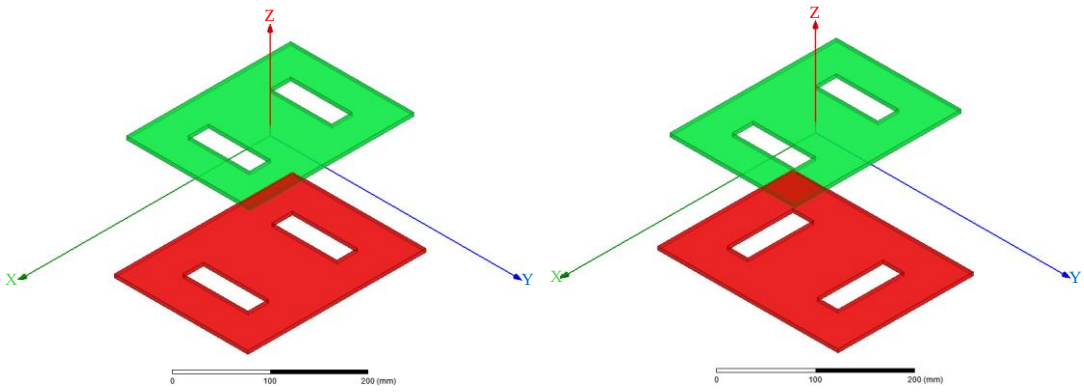

(a) (b)

Figure 3.4: Two placements: (a) Placement I and (b) Placement II.

A. Placement I

For placement I, the studied aspect ratios are “1:2”, “3:4”, “1:1”, and “4:3” for both the primary and secondary compensated coils. Simulation results are given in Figure 3.5(a) and the minimum coupling coefficient is 0.019 with the primary aspect ratio of “4:3” and secondary aspect ratio of “3:4”. Additionally, the inductances of the primary and secondary compensated coils are kept at 56 μH and 43 μH within 3% fluctuations in all simulation cases.

B. Placement II

Placement II is given in Figure 3.4(b) and the same aspect ratios are studied for both the primary and secondary compensated coils. As shown in Figure 3.5(b), the extra cross-side coupling coefficients are close to zero. Also, the compensated inductances remain at the desired values with 3% fluctuations in all simulation cases. The primary aspect ratio of “3:4” and

secondary aspect ratio of "4:3" are selected for the primary and secondary compensated coils for the purpose of winding the coils easily.

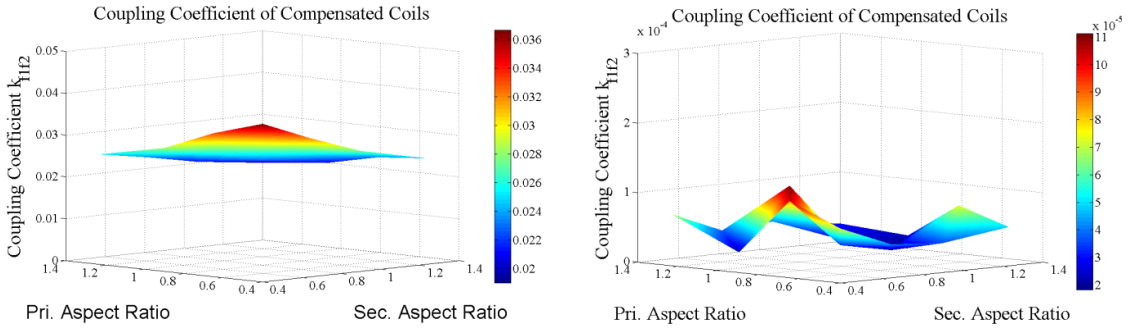

(a) (b)

Figure 3.5: Simulation results of k_{f1f2} at (a) placement I and (b) placement II.

In addition, in order to verify that the compensated coils are the most compact with the proposed integration method, simulation studies of compensated coils in ferrite-core and air-core types are conducted. Figure 3.6 gives the simulation models and in particular, the ferrite-core is made up of two E-cores. The compensated coils in different types are simulated to achieve the desired inductance values and their volumes are compared in Table 3.1. It is obvious that the air-core coils occupy the most space, the ferrite-core coils less, and the integrated coils the least. Furthermore, the integrated coils have two more advantages over the ferrite-core coils: (1) the integrated coils are planar, which is easier for packaging; (2) the integrated coils are more cost beneficial from material's point of view. The integrated coil needs more litz-wire while ferrite-core coils require four E-cores. The price of lite-wire is $1.16 per meter while one E-core costs $18.75. By calculation, the integrated coils save $50.99 per wireless charging system.

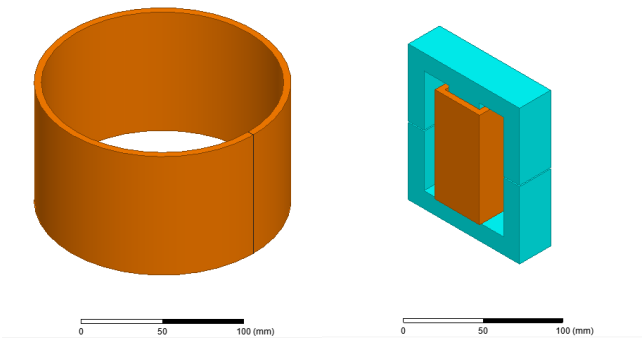

(a) (b)

Figure 3.6: Simulation models of (a) air-core coil and (b) ferrite-core coil.

Table 3.1: Volume for Each Coil.

Coil Type	L_{f1}	L_{f2}
Air Core	1.810×10^{6} mm^3	1.609×10^{6} mm^3
Ferrite Core	3.712×10^{5} mm^3	3.740×10^{5} mm^3
Integrated	2.250×10^{5} mm^3	1.800×10^{5} mm^3

The compensated coils are wound and measured. The resonant frequency is constant at 85 kHz. Once the inductances are determined, the capacitors C_1, C_2, C_{f1}, and C_{f2} can be calculated based on (2). Specifically, as stated in [14], the capacitor C_2 is 8% larger than the calculated value to guarantee zero voltage switching of the MOSFETs.

3.4 Experiment

Experiments were conducted from DC power source to DC electronic load. A full-bridge inverter and a full-bridge rectifier are used for power conversion between AC and DC. Based on our experience, the current densities in coils are desired to be less than 2.5 A/mm^2. Therefore, coils are wound with 800-strand AWG-38 litz wires. Ferrite plates are made of 3C95 ferrite bars. On each side of the wireless charging system, the main coil, the compensated coil, and the ferrite plate are wound or placed in separate plexiglass boards, which provides sufficient insulation and

guarantees safe and reliable operation. The measured circuit parameters are compared with the respective simulation results in Table 3.2. The measured values match well with the simulated values. Based on series-aiding and series-opposing method introduced by [62], different coupling coefficients in the fully aligned condition and four misaligned conditions are measured. Here, in each of the four misaligned conditions, misalignment only occurs in a single direction. For example, when the misalignment in Z-direction is 50 mm, the misalignment in X- and Y-direction is zero. The results on measured inductances and coupling coefficients are listed in Table 3.3 and Table 3.4. It is demonstrated by the measured results that the inductance values remain almost the same, only the main coupling coefficient should be considered, and other five coupling coefficients are negligible at the frequency of interest.

Table 3.2: Circuit Parameters.

Parameters	Simulated Values	Measured Values	Error
Primary main coil inductance L_1	229.47 μH	242.10 μH	5.21%
Primary compensated coil inductance L_{f1}	56.30 μH	60.08 μH	6.29%
Secondary main coil inductance L_2	182.30 μH	191.21 μH	4.66%
Secondary compensated coil inductance L_{f2}	43.61 μH	43.57 μH	0.09%
Primary capacitor C_1	19.70 nF	19.26 nF	2.28%
Primary compensated capacitor C_{f1}	58.38 nF	58.35 nF	0.05%
Secondary capacitor C_2	25.80 nF	25.68 nF	0.47%
Secondary compensated capacitor C_{f2}	79.67 nF	80.47 nF	1.37%

Table 3.3: Measured Inductance Values.

Conditions	L_1	L_2	L_{f1}	L_{f2}
Fully aligned	242.10 μH	191.21 μH	60.08 μH	43.57 μH
$Z_{misalign}$ = 50 mm	242.24 μH	188.82 μH	59.93 μH	43.52 μH
$X_{misalign}$ = 100 mm	244.77 μH	190.61 μH	59.99 μH	43.54 μH
$Y_{misalign}$ = 100 mm	245.81 μH	191.44 μH	60.06 μH	43.50 μH
$Y_{misalign}$ = 150 mm	247.41 μH	191.52 μH	59.84 μH	43.45 μH

Table 3.4: Measured Coupling Coefficients.

Conditions	k	k_{1f1}	k_{2f2}	k_{1f2}	k_{2f1}	k_{f1f2}
Fully aligned	0.2208	0.0028	0.0015	0.0002	0.0029	0.0006
$Z_{misalign}$ = 50 mm	0.1439	0.0026	0.0062	0.0001	0.0011	0.0007
$X_{misalign}$ = 100 mm	0.1886	0.0026	0.0057	0.0205	0.0055	0.0002
$Y_{misalign}$ = 100 mm	0.1426	0.0008	0.0060	0.0010	0.0490	0.0011
$Y_{misalign}$ = 150 mm	0.0869	0.0021	0.0058	0.0014	0.0474	0.0009

The design parameters are given in Table 3.5. The input DC voltage and DC load voltage are both 340 V. The resonant frequency is at 85 kHz and the air gap is 150 mm, which is appropriate for passenger cars. The output power is designed to be 3.0 kW. The experiment setup of the coil structures is shown in Figure 3.7. The bipolar compensated coils are integrated into the unipolar main coils. Moreover, in each turn of primary main coils, there are two litz wires in parallel. This not only ensures the coil width is the same as that in the simulation of Section 3.3 but also guarantees the primary main self-inductance is within the reasonable range.

Table 3.5: System Specifications.

Parameters	Designed Values
Input DC voltage	340V
Output DC voltage	340V
Primary main coil dimension	600 mm × 450 mm × 4 mm
Primary ferrite plate dimension	640 mm × 496 mm × 8 mm
Primary shield dimension	711 mm × 559 mm × 2 mm
Secondary main coil dimension	400 mm × 300 mm × 4 mm
Secondary ferrite plate dimension	480 mm × 352 mm × 8 mm
Secondary shield dimension	508 mm × 406 mm × 2 mm
Air gap	150 mm
Resonant frequency	85 kHz
Maximum output power	3.0 kW

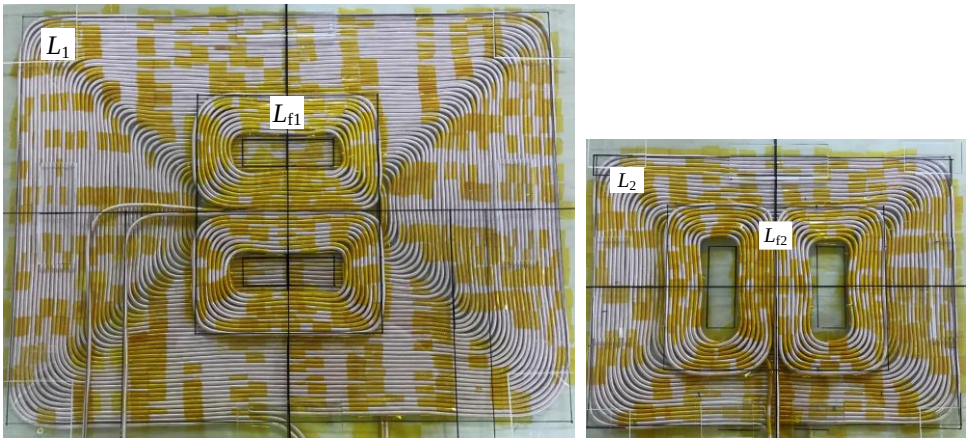

(a) (b)

Figure 3.7: Experiment setup of: (a) primary coils and (b) secondary coils.

The experiment is conducted when the primary and secondary coil structures are fully aligned and the respective waveforms are shown in Figure 3.8. The input and output DC voltages are both 340 V. The input AC current i_{f1} is almost in phase with the input AC voltage v_{ac} and a small phase shift is to guarantee the soft switching of the MOSFETs S_1 ~ S_4. As can be seen from Figure 3.8, when S_1 and S_4 are turned off, the instantaneous value of i_{f1} is approximately 4.0 A, which is larger than zero. Therefore, the drain to source voltages of S_1 an S_4 are zero when they are turned off. In addition, based on Chapter 2, a current value of 4.0 A is sufficient to charge the parasitic capacitors of S_2 and S_3 during the dead time so that the drain to source voltages of both S_2 and S_3 are almost zero when they are turned on. Thus, zero voltage switching is realized.

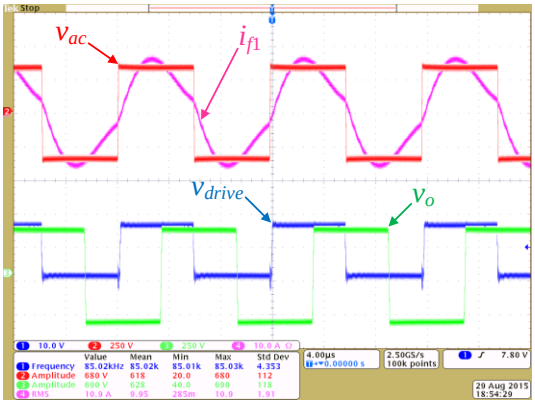

Figure 3.8: Waveforms when coil structures are fully aligned at maximum power.

Experiment on misalignment in different directions is also conducted and all the experimental results are presented in Figure 3.9. When the system is fully aligned, the wireless charging system delivers 3.09 kW power with a DC-DC efficiency of 95.49% at an air gap of 150 mm. When misalignment occurs, the main coupling coefficient k decreases while other parameters remain almost the same and there is almost no other extra coupling coefficient. The output power P_o drops with k when the same DC input voltage and load voltage are applied. Figure 3.10 gives the normalized values for P_o and k. The rated values for P_o and k are 3.09 kW and 0.2208 when the system is fully aligned. In Figure 3.10(a) and (b), P_o drops at the same rate with k when misalignment occurs in Z- or X-direction. The differences are within 2%, which validates (2.15) in Chapter 2. In Figure 3.10(c), when misalignment occurs in Y-direction, the maximum difference is approximately 10%. It is because the cross-side coupling coefficient k_{2f1} arises as the misalignment increases. However, k_{2f1} is under 0.05 in all conditions of misalignments in Y-direction, which is shown in Table 3.4. Therefore, the difference is acceptable and the adverse effect can be ignored. Hence, with the integration method, the extra coupling coefficients are eliminated or minimized to a negligible level and the wireless charging system is more compact. Furthermore, the efficiency of the wireless charging system is kept high. Thus, the experiment verifies the proposed idea.

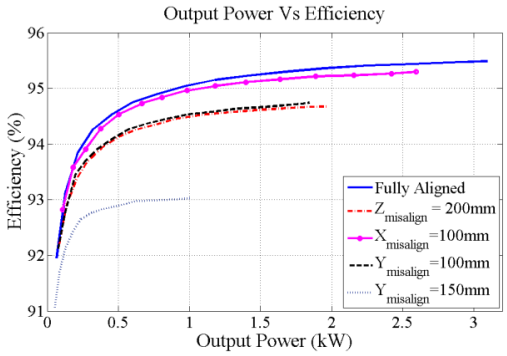

Figure 3.9: Experimental results on output power vs efficiency.

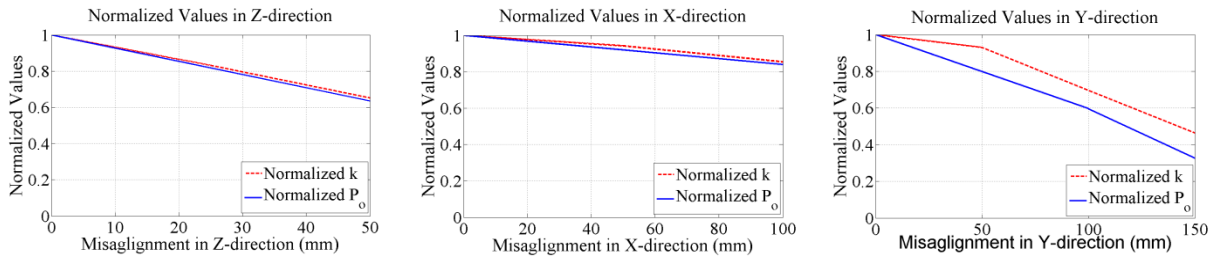

(a) (b) (c)

Figure 3.10: Normalized values in (a) Z-direction, (b) X-direction, and (c) Y-direction

3.5 Discussions

Two integration methods, named as integration into bipolar coils method (IB method) and integration into unipolar coils (IU method), are separately given in Chapter 2 and this chapter for wireless charging systems using the LCC compensation topology. In this section, the physical design parameters and system performance are compared between the two wireless charging systems with the two integration methods. Moreover, in order to make a fair comparison, power converters and the dimensions of the main coils, the ferrite plates, and the aluminum shield are all the same. An interoperability study of the proposed integrated coil structure with bipolar and unipolar coil structures is conducted at the end of this section.

A. Physical Design Parameters

From material's point of view, the two wireless charging systems with the two integration methods employ the same power converters and are controlled by the same microcontroller. Furthermore, the ferrite plates and aluminum shields are the same in the two systems. The difference occurs in the total length of litz-wires used in the two systems and the voltage and current ratings of the capacitors at 3.0 kW output power. Table 3.6 gives the comparison results. The total lengths of the litz-wires used in two systems are almost the same and the voltage and current ratings are similar for respective capacitors.

Table 3.6: Physical Design Comparison.

Quantity	Items	IB Method	IU Method
Total length	Litz-wires	92.92 m	86.58 m
Voltage/Current-rating (RMS)	Primary capacitor C_1	1,205V/12.69A	923V/9.45A
	Primary compensated capacitor C_{f1}	374V/16.60A	439V/13.67A
	Secondary capacitor C_2	803V/13.97A	997V/14.25A
	Secondary compensated capacitor C_{f2}	405V/20.76A	442V/19.70A

B. System Performance

Power and efficiency are the two main indexes in the system performance of a wireless charging system. As indicated by the experimental results on horizontal misalignment (i.e. X-direction and Y-direction) in Chapter 2 and this chapter, the output power of each system is different in X-direction from that in Y-direction even though the same input DC voltage is applied and both misalignments are 100 mm. Moreover, once an EV is parked, it is more difficult for a driver to adjust the EV in the door-to-door direction than in the front-to-rear direction. Therefore, in each system, the direction with a higher output power is aligned with EV's door-to-door direction and the direction with a lower output power is aligned with EV's front-to-rear direction.

Figure 3.11 gives the comparison of the system performance of the systems when the system is fully aligned, door-to-door misalignment is 100 mm, front-to-rear misalignment is 100 mm, and vertical misalignment is 50 mm. Efficiencies are compared when the same amount of output power is delivered by the two systems. The two systems have almost the same efficiency when the output power is the same when the system is fully aligned and door-to-door misalignment is 100 mm. However, the system with IU method has a relatively higher efficiency when front-to-rear misalignment is 100 mm and vertical misalignment is 50 mm. It is because the main coupling coefficient in the system with IU method drops more slowly than that in the

system with IB method as front-to-rear misalignment or vertical misalignment occurs. As shown in Table 3.7, *k* separately drops 30.4% and 34.8% from its original value in the system with IU method when front-to-rear misalignment is 100 mm and vertical misalignment is 50 mm while 44.5% and 44.3% in the system with IB method.

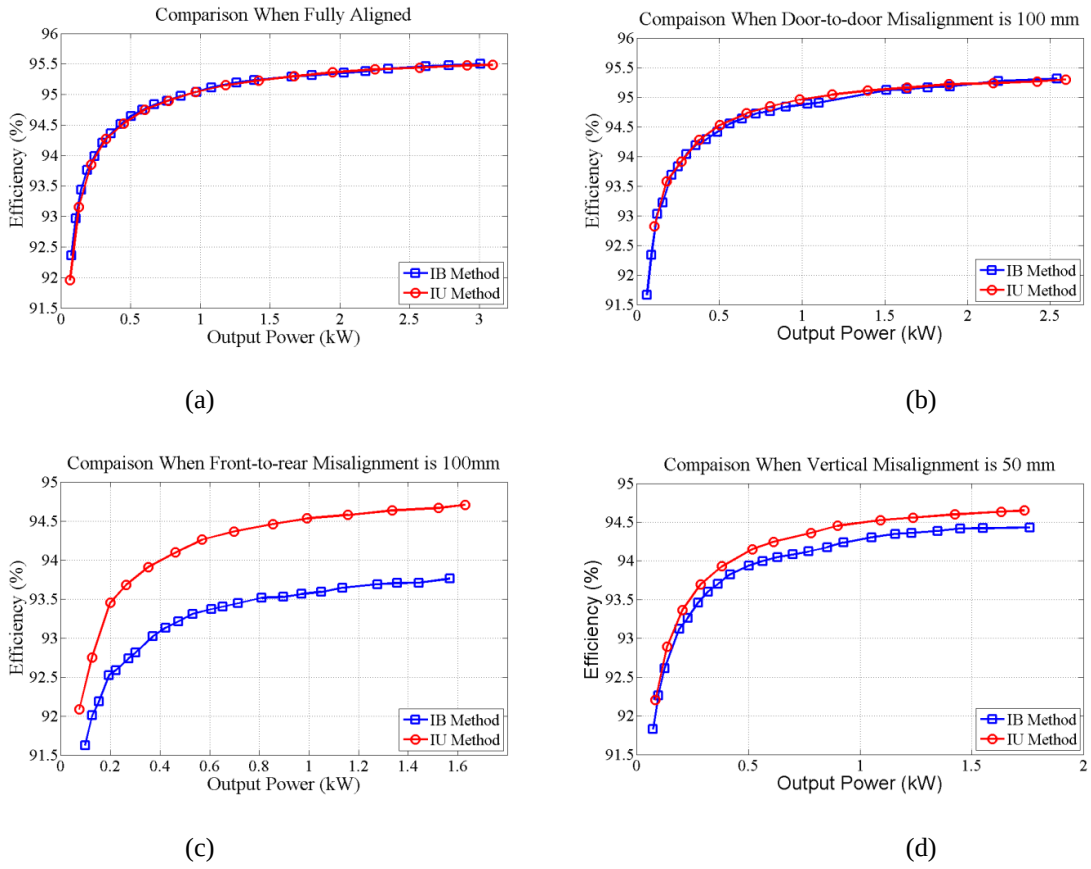

Figure 3.11: Comparison on system performance when: (a) system is fully aligned, (b) door-to-door misalignment is 100 mm, (c) front-to-rear misalignment is 100 mm, and (d) vertical misalignment is 50 mm.

Table 3.7: Main Coupling Coefficient in Different Scenarios.

Scenarios	IB Method		IU Method	
	Value	Dropped %	Value	Dropped %
Fully aligned	0.1877	0	0.2208	0
Door-to-door misalignment = 100 mm	0.1578	15.9%	0.1886	14.6%
Front-to-rear misalignment = 100 mm	0.1042	44.5%	0.1537	30.4%
Vertical misalignment = 50mm	0.1045	44.3%	0.1439	34.8%

Thus, based on the comparison of the physical design parameters and system performance, both systems employ a similar amount of materials and perform well in power and efficiency. The wireless charging system with IU method is comparatively better since it transfers power with a higher efficiency at the same output power level when front-to-rear or vertical misalignment occurs.

C. Interoperability Study

An interoperability study on the proposed coil structure with bipolar and unipolar coil structures has been conducted. The primary coil structure is either bipolar or unipolar while the secondary coil structure employs the proposed integrated coil structure, in which a bipolar compensated coil is integrated into a unipolar main coil. The coupling coefficients in the fully aligned condition are analyzed and measured. In one case, the primary coil is bipolar as shown in Figure 3.12(a), the net amount of magnetic flux generated by L_1 and passing through L_2 is zero. Therefore, the main coupling coefficient is zero. The primary main coil L_1 and secondary compensated coil L_{f2} are both bipolar and fully aligned. The coupling coefficient k_{1f2} exists and a voltage will be induced from L_1 to L_{f2}. However, power still cannot be transferred. It is because that the secondary main coil L_2, together with two capacitors C_2 and C_{f2}, form a parallel resonant circuit, of which the impedance is infinite in resonant condition. In the other case, the primary coil is unipolar as shown in Figure 3.12(b), which is the same as the one in this chapter. The coupling coefficients k is maximized and k_{1f2} is almost zero. The power transfer capability of the two main coils is maximized. Both the simulation and experimental results are summarized in Table 3.8. In order to successfully transfer power, the two main coils in a wireless charging system must be in the same type and fully aligned. Furthermore, for wireless charging systems

using LCC compensation topology, the integration method should be selected based on the main coil type.

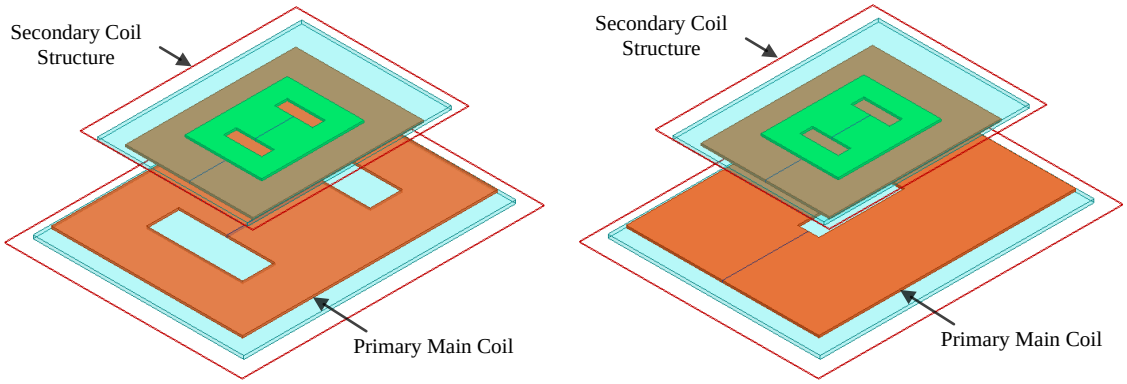

(a) (b)

Figure 3.12: Interoperability study with (a) primary bipolar coil and (b) primary unipolar coil.

Table 3.8: Interoperability Study.

Primary Main Coil Type	k		k_{1f2}	
	Simulation	Measured	Simulation	Measured
Bipolar	6.398×10^{-5}	7.241×10^{-5}	0.0564	0.0619
Unipolar	0.2310	0.2208	0.00014	0.0002

3.6 Conclusions

In this chapter, an integration method for unipolar coil structures in EV wireless charging systems using the LCC compensation topology is proposed. It effectively eliminates the extra coupling coefficients resulted from integration, simplifies the design, makes the system more compact, and keeps the outstanding system performance of a wireless charging system using the double-sided LCC compensation topology. The aspect ratios of compensated coils are analyzed to minimize the respective coupling coefficient through simulations. In addition, a wireless charging system with the proposed integration method is built and the experimental results demonstrate that the system is able to transfer 3.09 kW with a DC-DC efficiency of 95.49% at an

air gap of 150 mm when fully aligned. Furthermore, a comparative study of the physical design parameters and system performance between a wireless charging system with the proposed method and a wireless charging system with the integration into bipolar main coils has been conducted. The results show that the wireless charging system with the proposed integration is better because of its superior performance on EV's front-to-rear misalignment and vertical misalignment. Therefore, the proposed integration method is more applicable.

This Chapter is based on the following accepted paper. As the first author, I proposed and analyzed the coil structure, performed simulations, conducted the experiment and the discussions, and drafted the paper.

T. Kan, F. Lu, T. D. Nguyen, P.P. Mercier, and C. Mi, "Integrated coil design for EV wireless charging systems using LCC compensation topology," *IEEE Trans. Power Electron*., 2018. [in press]

Chapter 4

Three-Phase Coil Design for AUVs

4.1 Introduction

Another important application of magnetic-resonance based wireless power transfer is to charge AUVs. By efficient and high-power wireless charging, the mission tournament time of an AUV can be significantly increased.

Research in this field started with Freezor et al. [34] and has been expanded into multiple directions since. For example, some researchers targeted improving the transferred power level with high efficiency: Kojiya et al. developed a cone-type coil structure and wirelessly delivered 500 W at a coil-to-coil efficiency of 93.1% [38]; Li et al. performed reluctance modeling and conducted experiments on a wireless charger with a planar coil structure, achieving 400 Watts of power transfer at a DC-DC efficiency of 90% [36]; Cheng et al. proposed a semi-closed magnetic core structure, analyzed the power loss, and built an underwater wireless charging system to transfer 10 kW at a DC-DC efficiency of 91% [39]. However, such work did not carefully consider the compatibility of the AUV's hull – the hull resistance in such cases may increase after installation, and, as a result, the AUV's speed might be reduced. As a result, other researchers have aimed at designing hull-compatible coil structure and addressing the AUV's hull resistance increase after coil structure's installation: Shi et al. presented a coaxial coil structure which could be installed around the AUV's hull with few adverse effects and established a prototype to transfer 45 W at 84% efficiency [37]; Lin et al. further studied the coaxial structure, performed the loss analysis, and enhanced the output power to 300 W with an

efficiency of 77% [63]. In general, a coaxial coil arrangement showed good compatibility with the AUV's hull and efficiency was acceptable; however, the generated magnetic field was divergent within the hull, and thus might adversely affect electronic instrumentation within the AUV. Therefore, one of the main challenges in designing a wireless charging system is to design a coil structure to have few adverse effects on the shape of the AUV's hull and the existing electronics devices within the AUV.

Nowadays, composite materials with isolation properties, such as fiberglass, are commonly used as the hull material for AUVs [64], which makes it possible to install the receiver in the AUV without adversely affecting the shape of the AUV's hull. In this chapter, a new three-phase coil structure consisting of three identical transmitters and three identical receivers as shown in Figure 4.1(a), is proposed. To further show the advantages of the proposed three-phase coil structure over a conventional coaxial coil structure in Figure 4.1(b), magnetic field studies have been conducted for both coil structures. Through ANSYS MAXWELL simulations, it is demonstrated that the magnetic field generated by the proposed coil structure is concentrated in the coil structure instead of elsewhere within the AUV's hull. As a result, interference to the existing electronics devices in the AUV will be less, and more space will thus be available within the AUV for instrumentation. The proposed circuit is further analyzed and compensation methods to achieve resonance are introduced. Subsequently, a 1.0 kW three-phase wireless charging system with 92.41% DC-DC efficiency is designed and tested to validate the proposed concept.

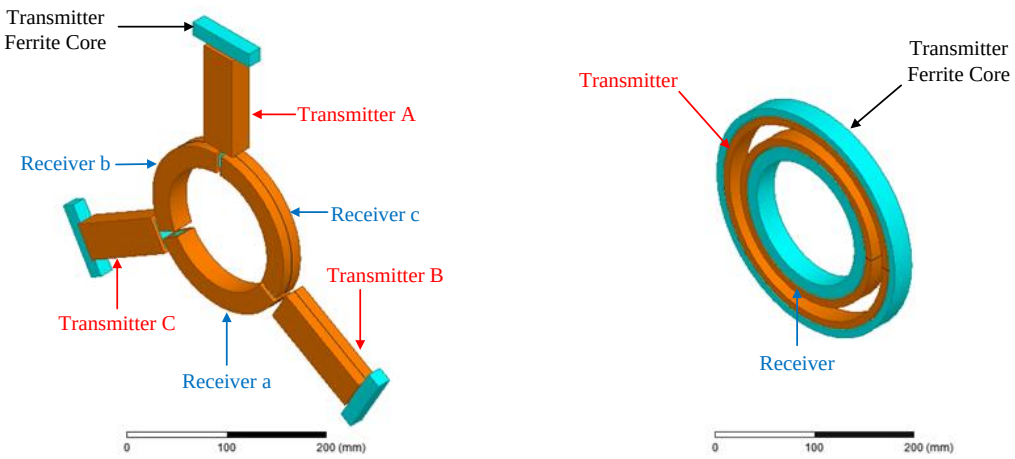

(a) (b)

Figure 4.1: Coil structures in simulation: (a) proposed three-phase coil structure and (b) coaxial coil structure.

4.2 Coil Design

Coil design is important in all wireless power transfer systems, as the geometries and properties of the coils ultimately set limits on power transfer capabilities and power transfer efficiency. In addition, coil design directly determines field patterns, which are important to manage so as to not adversely affect the existing electronics devices in an AUV. This is especially important, since the size of an AUV is compact and space within it is quite limited. As a result, it is desired to concentrate magnetic fields generated by the coil structure within the coil structure itself, and outside of the interior of the AUV's hull so that the existing electronics devices in the AUV are not adversely affected. Figure 4.1(a) shows the proposed coil structure, which consists of three identical transmitters and three identical receivers. The excitation currents in all transmitters have the same magnitude and frequency, but are 120° out of phase. The magnetic flux excited by the current in one transmitter passes through the AUV's hull, couples with its two adjacent receivers, and goes back to that transmitter. In order to demonstrate the advantages of the proposed coil structure over the conventional coaxial one, a three-dimensional (3-D) finite-element analysis (FEA) tool (ANSYS MAXWELL) is employed and

magnetic field studies are conducted in both the three-phase and coaxial coil structures presented in this section. Additionally, the materials used in two wireless charging systems with the two respective coil structures are compared. Furthermore, the parameters of the proposed coil structure in both seawater condition and ambient air condition are investigated.

A. Coil Structures Design

A 3D overview and a cross-sectional front view of the simulation model of the proposed coil structure are shown in Figure 4.2. In this simulation setup, the transmitters with the primary capacitors are packaged with water-resistant materials and immersed in seawater, and the receivers with the secondary capacitors are encapsulated in the AUV's hull. The hull, whose outer diameter is 200mm, is made of fiberglass and filled with air. The simulation model for the coaxial coil structure has the same dimensions of the seawater and AUV's hull; the only difference between the two models is the coil structure.

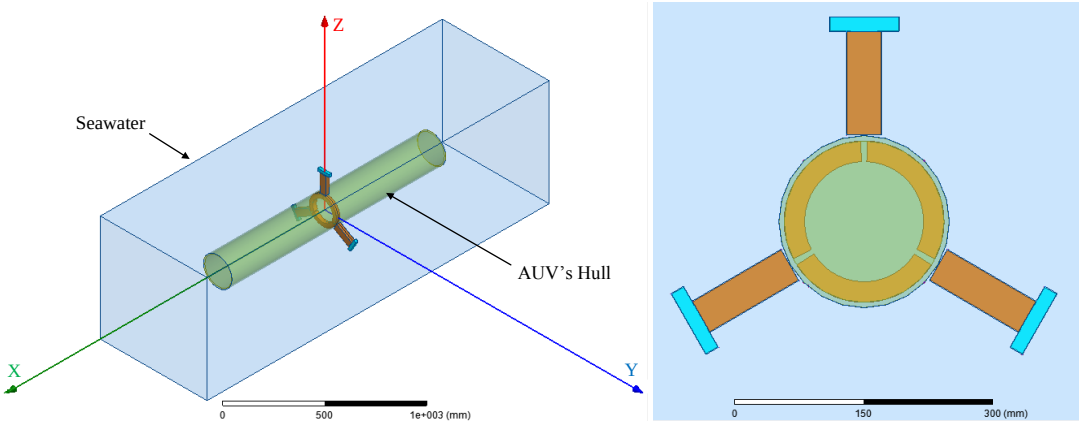

(a) (b)

Figure 4.2: (a) Overview and (b) Front view of MAXWELL simulation model for the proposed coil structure.

Due to the compactness of the AUV, the volume of any coil structure is important. In this study, 1.0 kW power is required to be transferred by both two wireless charging systems to facilitate rapid charging. The frequency is assigned to be 465 kHz, which makes the system compact and ensures sufficient power can be transferred to the load. In order to make a fair

comparison, the receivers of both coil structures are set to occupy the same volume. As shown in Figure 4.3, they are fixed within dimensions of a hollow cylinder with an outer radius of 94 mm, an inner radius of 70 mm, and a height of 24 mm. Though the geometries of the transmitters in the two coil structures are different, the volumes are designed approximately the same at 350,000 mm^3. Figure 4.4 gives the design variables: (1) primary coil length and secondary coil angle for the proposed coil structure and (2) primary coil width and secondary coil width for the coaxial coil structure.

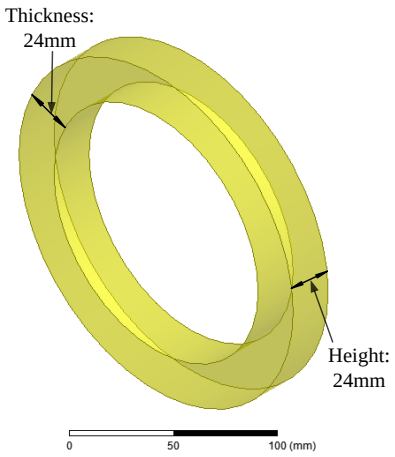

Figure 4.3: A hollow cylinder for receivers.

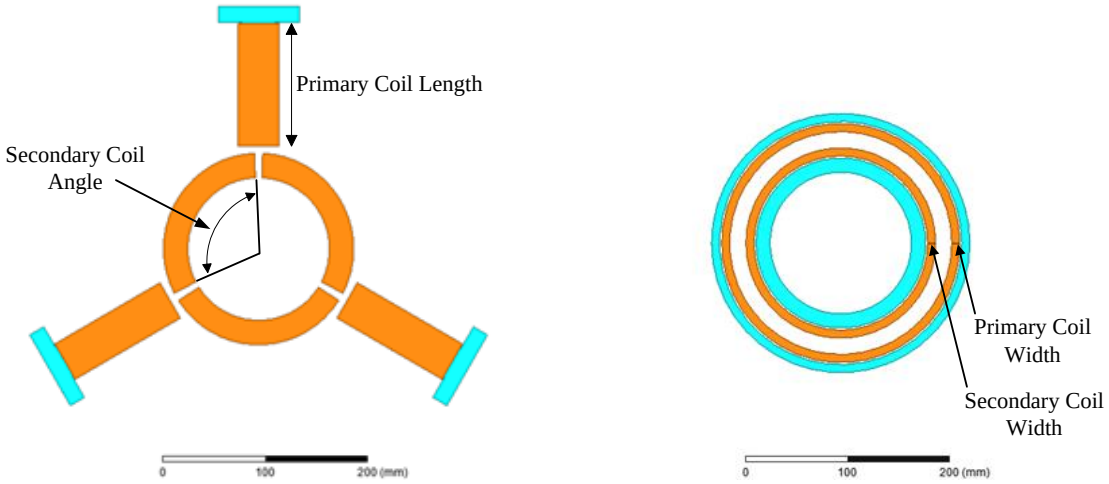

(a) (b)

Figure 4.4: Design variables in (a) proposed coil structure and (b) coaxial coil structure.

Variant mutual inductances can be achieved by sweeping the design variables within the limitations of the coil structure dimensions. The mutual inductance of a coil structure determines its capability of transferring power, and for a 1.0 kW design, a mutual inductance value of 7 μH is desired at the frequencies of interest. Therefore, the sets of design variables to achieve 7 μH mutual inductances are selected for both two coil structures. The simulated parameters are given in Table 4.1. Specifically, the mutual inductance in the proposed coil structure refers to the mutual inductance between one transmitter and one of its adjacent receivers.

Table 4.1: Simulation Results.

Parameters	Proposed Coil	Coaxial Coil
Transmitter's Self-inductance L_t	68.86 μH	13.09 μH
Receiver's Self-inductance L_r	33.67 μH	14.88 μH
Coupling Coefficient k_{tr} between L_t and L_r	0.1385	0.5130
Mutual Inductance M_{tr} between L_t and L_r	6.67 μH	7.16 μH

Simulation studies on rotational misalignment are also conducted for the two coil structures. Figure 4.5(a) shows the rotational angle for the three-phase coil structure, noting that the relative separation between the transmitting coils is fixed during rotation. Figure 4.5(b) shows the coaxial model. The variations in mutual inductance for both models are shown in Figure 4.5(c). As the rotational angle increases from 0° to 25°, the mutual inductance in the proposed three-phase coil structure is competitive or exceeds that of the coaxial coil structure. However, as the rotational angle increases from 25° to 60°, the mutual inductance in the proposed coil structure drops dramatically and ends at zero, while the mutual inductance in the coaxial coil structure remains constant. Therefore, the coaxial coil structure has more stable performance on rotational misalignment than the proposed coil structure. However, rotational misalignment in the proposed coil structure can be eliminated by employing an advanced

mechanical positioning system since three transmitters are separate and flexible to move. Therefore, the following analysis and experiment are conducted in full aligned condition.

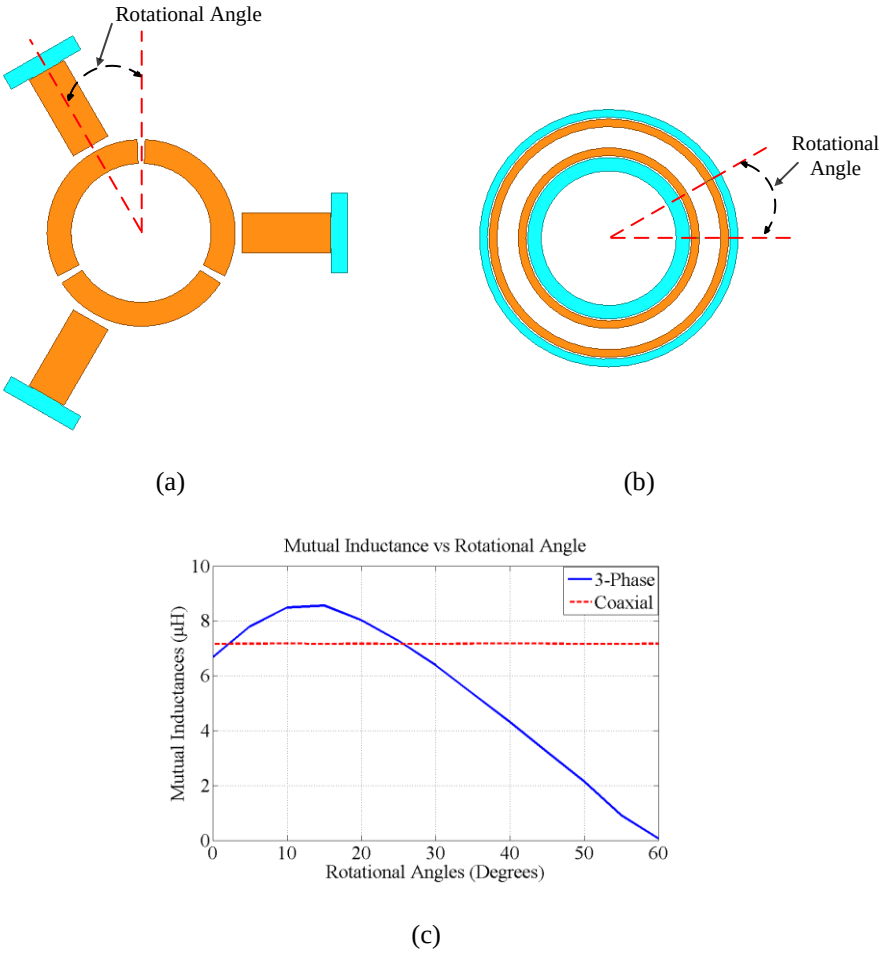

Figure 4.5: (a) Rotational angle in the proposed coil structure, (b) Rotational angle in coaxial coil structure, and (c) Mutual inductances variation with rotational angles.

B. Magnetic Field Studies

The main advantage of the proposed coil structure over the conventional coaxial coil structure is that the generated magnetic field is concentrated within the coil structure itself, which has fewer adverse effects on the existing electronics devices in the AUV. In order to study and compare the magnetic fields, both coil structures are required to transfer 1.0 kW power with the same charging current, which is the root mean square (RMS) value of the alternating current

before the rectifier and fixed at 10A. A series – series compensation topology is applied due to its simplicity, constant-current principle, and ability to deliver high power at reasonable voltage levels [19], [20]. The excitation currents and the turn numbers for transmitters and receivers are given in Table 4.2, where I_t is the transmitter's current, I_r is the receiver's current, and $\omega M_{tr} I_t$ is the equivalent voltage on the receiver's side induced by the transmitter's current. All the voltage and current values in Table 4.2 are RMS values. Furthermore, the ampere-turns in the receivers of the two coil structures are kept the same.

Table 4.2: Excitations in Simulation.

Parameters	Proposed Coil	Coaxial Coil
Transmitter's Current I_t	5.13 A	4.78 A
Receiver's Current I_r	3.33 A	10 A
Turn Number of Transmitter's Coil	22	5
Turn Number of Receiver's Coil	18	6
Induced Voltage $\omega M_{tr} I_t$	100 V	100 V
Total Charging Current	10 A	10 A
Power	1.0 kW	1.0 kW

The two coil structures were implemented in ANSYS MAXWELL, and simulation results of the magnetic flux densities of the two coil structures in YZ-, ZX-, and XY-plane are shown in Figures 4.6 to 4.8 respectively. The scale bars in the figures are all the same: 2.45×10^{-3} T at maximum and 1×10^{-4} T at minimum. Here, the light stripes in Figures 4.7 and 4.8 stand for the AUV's position in simulation. Both the proposed coil structure and the coaxial coil structure perform fairly well in the YZ-plane. The generated magnetic field of the proposed coil structure in the AUV is stronger around the receivers and weaker in the center, while the generated magnetic field of the coaxial structure is weaker around its receiver and stronger in the center.

Even though a ferrite core is employed at receiver's side in the coaxial coil structure, a certain amount of magnetic fluxes still exist in the center. Moreover, Figures 4.7(b) and 4.8(b) indicate the generated magnetic field of the coaxial coil structure is more divergent in ZX- and XY-plane. Instead, Figures 4.7(a) and 4.8(a) show the proposed coil structure gives outstanding performance in ZX- and XY-plane. The generated magnetic field is more concentrated in the coil structure rather than disperses from it. As a result, the existing electronics devices are less affected, meaning that they can be installed closer to the coil structure and more space will be available in the AUV.

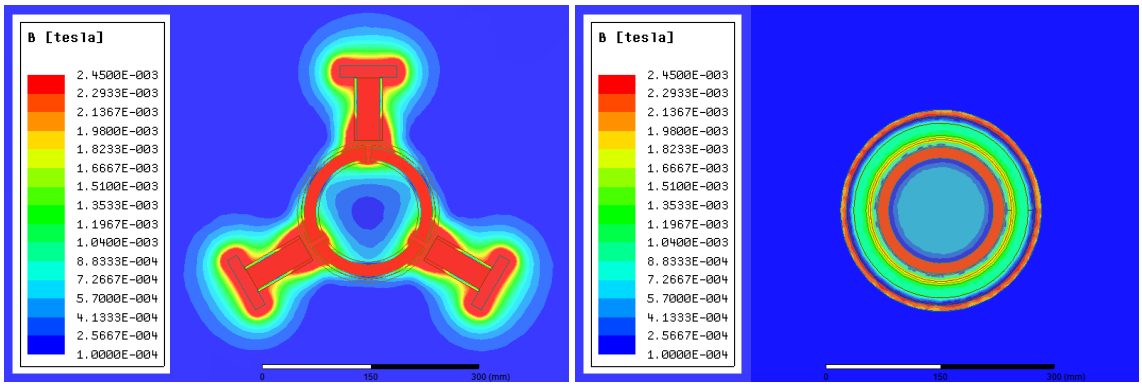

(a) (b)

Figure 4.6: Magnetic flux densities in YZ-plane: (a) proposed coil structure and (b) coaxial coil structure.

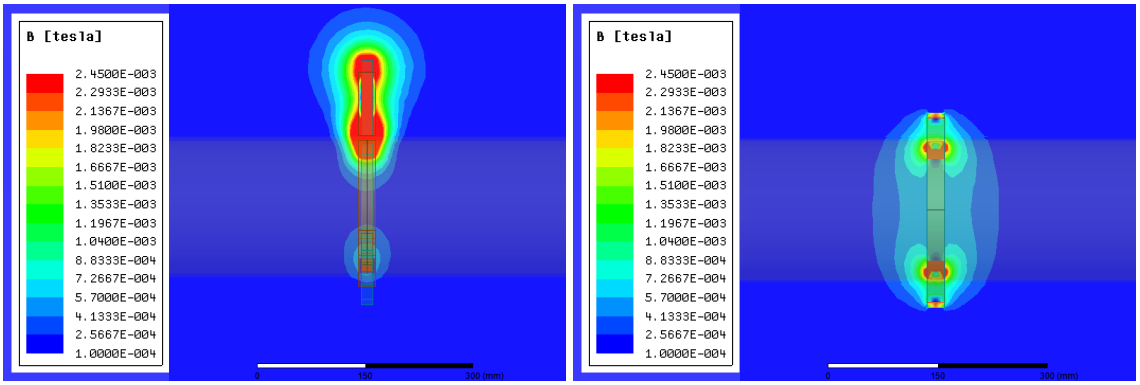

(a) (b)

Figure 4.7: Magnetic flux densities in ZX-plane: (a) proposed coil structure and (b) coaxial coil structure.

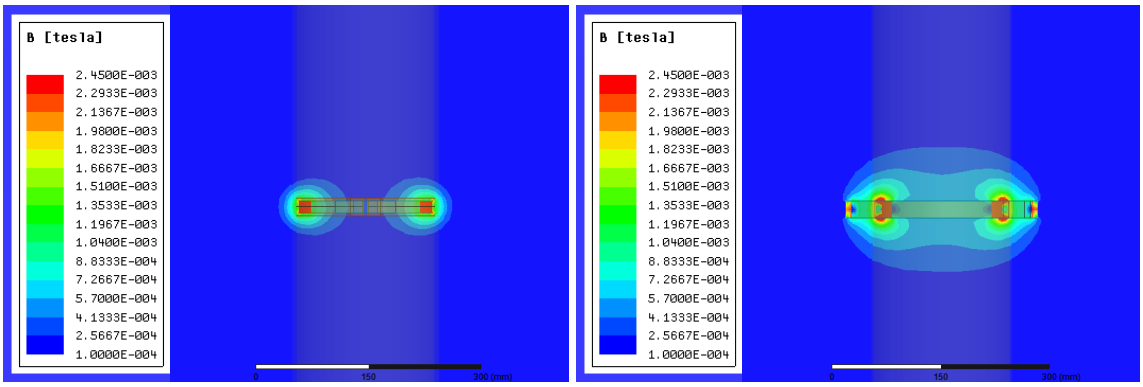

(a) (b)

Figure 4.8: Magnetic flux densities in XY-plane: (a) proposed coil structure and (b) coaxial coil structure.

C. Materials Comparison

To further compare the two coil structures, materials used in building the two wireless charging systems are analyzed. The comparison is focused on materials used in three stages: the inverter stage, the rectifier stage, and the resonant tank stage. In the inverter and rectifier stages, the materials used in the proposed three-phase system are three times of those in the conventional single-phase system. For example, if full-bridge inverters and full-bridge rectifiers are applied for power conversion, three inverters consisting of twelve MOSFETs and three rectifiers with twelve diodes will be employed in the proposed three-phase system while only one inverter with four MOSFETs and one rectifier with four diodes will be used in the conventional single-phase system. The conventional single-phase system with the coaxial coil structure is more cost beneficial in the inverter and rectifier stages. The resonant tank is mainly constituted by the coil structure and the series resonant capacitors. 202,321 mm^3 of copper and 310,724 mm^3 of ferrite are used in the proposed coil structure while the volumes of copper and ferrite in the coaxial coil structure are 229,211 mm^3 and 319,387 mm^3. In the proposed coil structure, three transmitter's capacitors, which are in series with transmitter's coils, and three receiver's capacitors, which are in series with receiver's coils, are employed. The voltage across

each transmitter's capacitor is 1.032 kV and the current passing through it is 5.13 A. The voltage across each receiver's capacitor is 319.7 V and the current passing through it is 3.33 A. In the coaxial coil structure, one transmitter's capacitor and one receiver's capacitor are selected. Each transmitter's capacitor is required to withstand a voltage of 182.8 V and a current of 4.78 A. Each receiver's capacitor is capable of bearing a voltage of 434.8 V and a current of 10 A. All the voltage and current values are in RMS and they are calculated by equations in Section 3.3.

Table 4.3: Materials Comparison.

Items	Proposed Coil	Coaxial Coil
Number of Inverters	3	1
Number of Rectifiers	3	1
Copper	202,321 mm^3	229,211 mm^3
Ferrite	310,724 mm^3	319,387 mm^3
Number of Capacitors	6	2
VA rating of Transmitter's Capacitor	5.295 kVA	0.874 kVA
VA rating of Receiver's Capacitor	1.065 kVA	4.347 kVA

The comparison results on materials are summarized in Table 4.3. The wireless charging system with the coaxial coil structure uses fewer inverters and rectifiers while the wireless charging system with the proposed coil structure uses a smaller amount of copper and ferrite materials. The VA ratings of the capacitors range from several hundred VA to several thousand VA; however, fewer capacitors are applied in the wireless charging system with coaxial coil structure. Thus, despite some disadvantages in copper and ferrite materials, it is estimated that the conventional single-phase coaxial wireless charging system is more cost beneficial from a materials point of view.

D. Investigation on Parameters of the Proposed Coil Structure in Two Conditions

The conductivity of seawater is only 4 Siemens per meter and its relative magnetic permeability is very close to 1. Thus, to the first order the seawater can be considered as air at the frequencies of interest. Specifically, the magnetic fields generated by the coil structure in seawater will be approximately the same with that in air, and the eddy current loss in seawater will be very small. To validate this assumption, a simulation model with neither seawater nor the AUV's hull but only the ambient air is built and the simulated results are contrasted to those with seawater and the AUV's hull. The parameters are illustrated in Figure 4.9 and compared in Table 4.4, where L_t is transmitter's coil inductance, L_r is the receiver's coil inductance, k_{tr} is the coupling coefficient between one transmitter and one of its two adjacent receivers, k_{tr0} is the coupling coefficient between one transmitter and its away receiver, k_{tt} is the coupling coefficient between two transmitters, and k_{rr} is the coupling coefficient between two receivers. The differences in coil parameters between the original model and ambient air model are small. Moreover, a simulation on the magnetic field generated by the proposed coil structure in the ambient air condition is performed and simulation results demonstrate that the generated magnetic field is the same in two conditions. In order to simplify the analysis and experiment, the seawater and the AUV's hull are ignored in later sections.

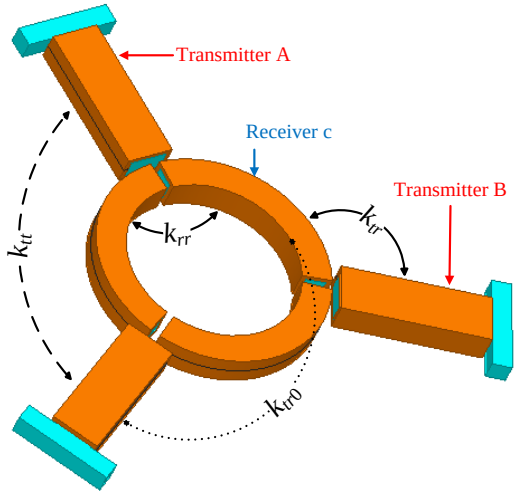

Figure 4.9: Instructions on coil parameters.

Table 4.4: Parameters Comparison.

Parameters	Seawater	Ambient Air	Error
L_t	68.86 μH	69.56 μH	1.02%
L_r	33.67 μH	33.98 μH	0.92%
k_{tr}	0.1385	0.1393	0.58%
k_{rr}	0.2404	0.2399	0.21%
k_{tt}	0.0256	0.0264	3.13%
k_{tr0}	≈ 0	≈ 0	0%

4.3 Circuit Analysis

Analysis is focused on the circuit from DC power supply to DC electronic load. Full-bridge inverters are chosen to convert DC power to high frequency AC power. The AC power flows into the transmitter's resonant tank formed by the transmitter's compensation capacitor C_t in series with the transmitter's coil L_t. It resonates in the transmitter's resonant tank at a single resonant frequency and wirelessly transfers to the receiver's resonant tank through the mutual inductance between the transmitter's coil and the receiver's coil. The receiver's resonant tank has

the same resonant frequency with the transmitter's resonant tank and is constituted by the receiver's compensation capacitor C_r in series with the receiver's coil L_r. The high frequency resonating AC power gets rectified to DC power by full-bridge rectifiers. In the three-phase wireless charging system, three inverters and three rectifiers are employed. The three transmitters are named as A, B, and C. The receiver away from transmitter A is receiver a, and likewise for B and C (b and c). For simplicity, only one inverter at transmitter A and one rectifier at receiver c are shown in Figure 4.10, where U_{in} is the DC voltage of DC power supply, u_A is the AC input voltage of transmitter A's resonant tank, and R_L is the resistance of the DC electronic load. Since a series-series compensation topology is selected, the circuit behaves like a constant voltage source. However, if the input voltage to the inverter is a constant, then its output current is also a constant. Therefore, based on [43], the AC input voltage u_A and the equivalent resistance R_{eq} of load resistance R_L at the rectifier's input side can be expressed as

$$u_A = \frac{2\sqrt{2}}{\pi} U_{in} \angle 0^\circ \tag{4.1}$$

$$R_{eq} = \frac{8}{\pi^2} R_L \tag{4.2}$$

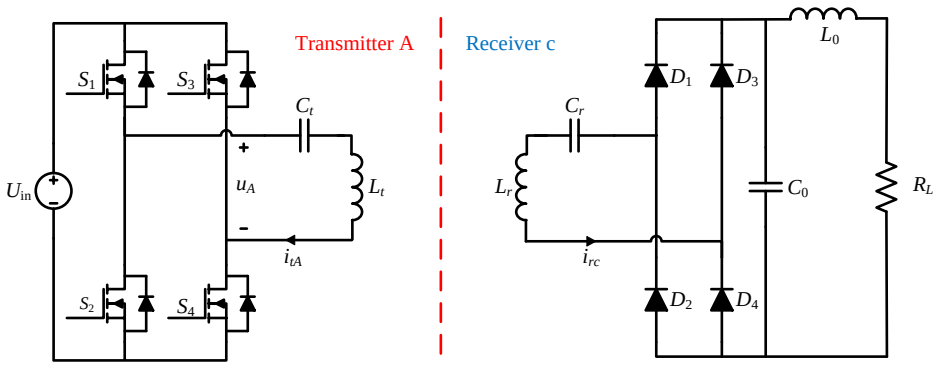

Figure 4.10: Full-bridge inverter at transmitter A and full-bridge rectifier at receiver c.

Three full-bridge inverters convert the DC input voltage to three AC voltages with the same magnitude and frequency, yet at 120° out of phase. Since the initial phase angle of u_A is

assigned to be 0°, the initial phase angles of transmitter B's AC input voltage u_B and transmitter C's input voltage u_C are 120° and 240°. Resonance is achieved on both transmitter's side and receiver's side. Therefore, the current in each transmitter is in phase with the respective input AC voltage and the current in each receiver is in phase with the respective induced voltage. The transmitter's currents i_{tA}, i_{tB}, and i_{tC} have the same magnitude I_t and initial phase angles of 0°, 120°, and 240°, respectively. The induced voltages $j\omega M_{tr}i_{tA}$, $j\omega M_{tr}i_{tB}$, and $j\omega M_{tr}i_{tC}$, from transmitter's side to receiver's side, have initial phase angles of 90°, 210°, and 330°, respectively. Based on the simulation results in Section 4.2, k_{tt} and k_{tr0} are considerably small. The coupling effect between each two transmitters and the coupling effect between each transmitter and its away receiver can be neglected in analysis. The coupling effect between each transmitter and its adjacent receivers and the coupling effect between each two receivers are dominant. The equivalent mutual inductance models for receiver c and transmitter A are shown in Figure 4.11, where M_{rr} is the mutual inductance between two receivers. Here, the full-bridge inverter and rectifier are omitted. Furthermore, the equivalent series resistance of all the capacitors and inductors are ignored in analysis. As can be seen from Figure 4.11(a), the initial phase angle of the receiver c's current i_{rc} is determined by $j\omega M_{tr}i_{tA}$ and $j\omega M_{tr}i_{tB}$. According to the triangle rule, the initial phase angle of i_{rc} is 150°. Similarly, the initial phase angle of the receiver a's current i_{ra} and the receiver b's current i_{rb} are 270° and 30°. Moreover, i_{ra}, i_{rb}, and i_{rc} have the same magnitude I_r.

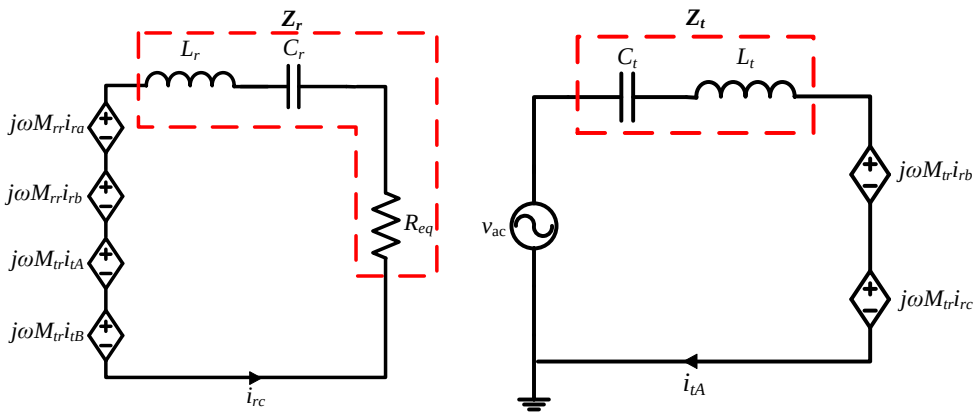

(a) (b)

Figure 4.11: Equivalent mutual inductance models for (a) receiver c and (b) transmitter A.

In the resonance condition, the capacitor C_r on receiver's side is required to compensate the receiver coil's self-inductance as well as the equivalent inductances caused by two induced voltages from the other two receivers. The capacitor C_t on transmitter's side only compensates the transmitter coil's self-inductance since the reflected impedances Z_{refl} from the receiver's side to the transmitter's side are purely resistive.

$$\omega L_r - \frac{1}{\omega C_r} + \frac{\omega M_{rr} i_{ra} + \omega M_{rr} i_{rb}}{i_{rc}} = 0 \tag{4.3}$$

$$\mathrm{Im}\left(Z_{refl}\right) = \mathrm{Im}\left(\frac{j\omega M_{tr} i_{rb} + j\omega M_{tr} i_{rc}}{i_{ta}}\right) = 0 \tag{4.4}$$

$$\omega L_t - \frac{1}{\omega C_t} = 0 \tag{4.5}$$

where ω is angular resonant frequency. The impedances Z_r and Z_t are defined in Figure 4.11 and written as

$$Z_r = j\omega L_r + \frac{1}{j\omega C_r} + R_{eq} \tag{4.6}$$

$$Z_t = j\omega L_t + \frac{1}{j\omega C_t} \tag{4.7}$$

Kirchhoff's voltage law (KVL) is applied and six voltage equations are derived as

$$\begin{bmatrix} u_{\mathrm{A}} \\ u_{\mathrm{B}} \\ u_{\mathrm{C}} \\ 0 \\ 0 \\ 0 \end{bmatrix} = \begin{bmatrix} Z_{\mathrm{t}} & 0 & 0 & 0 & j\omega M_{\mathrm{tr}} & j\omega M_{\mathrm{tr}} \\ 0 & Z_{\mathrm{t}} & 0 & j\omega M_{\mathrm{tr}} & 0 & j\omega M_{\mathrm{tr}} \\ 0 & 0 & Z_{\mathrm{t}} & j\omega M_{\mathrm{tr}} & j\omega M_{\mathrm{tr}} & 0 \\ 0 & j\omega M_{\mathrm{tr}} & j\omega M_{\mathrm{tr}} & Z_{\mathrm{r}} & j\omega M_{\mathrm{rr}} & j\omega M_{\mathrm{rr}} \\ j\omega M_{\mathrm{tr}} & 0 & j\omega M_{\mathrm{tr}} & j\omega M_{\mathrm{rr}} & Z_{\mathrm{r}} & j\omega M_{\mathrm{rr}} \\ j\omega M_{\mathrm{tr}} & j\omega M_{\mathrm{tr}} & 0 & j\omega M_{\mathrm{rr}} & j\omega M_{\mathrm{rr}} & Z_{\mathrm{r}} \end{bmatrix} \cdot \begin{bmatrix} i_{\mathrm{ta}} \\ i_{\mathrm{tb}} \\ i_{\mathrm{tc}} \\ i_{\mathrm{ta}} \\ i_{\mathrm{tb}} \\ i_{\mathrm{tc}} \end{bmatrix} \tag{4.8}$$

By substituting (4.3), (4.5), (4.6) and (4.7) into (4.8), six currents can be solved as

$$\begin{bmatrix} i_{\mathrm{tA}} \\ i_{\mathrm{tB}} \\ i_{\mathrm{tC}} \\ i_{\mathrm{ra}} \\ i_{\mathrm{rb}} \\ i_{\mathrm{rc}} \end{bmatrix} = \begin{bmatrix} \dfrac{u_{\mathrm{A}} R_{\mathrm{eq}}}{\omega^2 M_{\mathrm{tr}}^2} & \dfrac{u_{\mathrm{B}} R_{\mathrm{eq}}}{\omega^2 M_{\mathrm{tr}}^2} & \dfrac{u_{\mathrm{C}} R_{\mathrm{eq}}}{\omega^2 M_{\mathrm{tr}}^2} & j\dfrac{u_{\mathrm{a}}}{\omega M_{\mathrm{tr}}} & j\dfrac{u_{\mathrm{b}}}{\omega M_{\mathrm{tr}}} & j\dfrac{u_{\mathrm{c}}}{\omega M_{\mathrm{tr}}} \end{bmatrix}^{\mathrm{T}} \tag{4.9}$$

The real power transferred from the transmitter's side to the receiver's side is

$$P_{\mathrm{real}} = \mathrm{Re}(u_{\mathrm{A}} \cdot i_{\mathrm{tA}}^{*} + u_{\mathrm{B}} \cdot i_{\mathrm{tB}}^{*} + u_{\mathrm{C}} \cdot i_{\mathrm{tC}}^{*}) = \frac{3U_{\mathrm{A}}^2 R_{\mathrm{eq}}}{\omega^2 M_{\mathrm{tr}}^2} \tag{4.10}$$

Combining (4.1), (4.2) with (4.9), the power equation from DC power supply to DC electronic load is

$$P = \frac{192 \cdot U_{\mathrm{in}}^2 R_{\mathrm{L}}}{\pi^4 \omega^2 M_{\mathrm{tr}}^2} \tag{4.11}$$

4.4 Experiment

A three-phase wireless charging system is designed and tested to verify the proposed concept and compensation method. As indicated by Section 4.2, the seawater and the AUV's hull are reasonably ignored: unless otherwise specified, both simulations and experiments in this section are conducted in ambient air conditions. Unfortunately, it is extremely difficult to find appropriate arc-shape ferrite cores off-the-shelf. Thus, straight ferrite bars are employed for the

receivers for convenience. Moreover, the available ferrite bars are smaller than the arc-shape ferrite cores in the simulation of Section 4.2. Therefore, the turn numbers are slightly different from those in the simulation of Section 4.2. However, the mutual inductance values in both sections are kept nearly the same. The resonant frequency is set to be 465 kHz. The dimensional parameters of the coil structure are given in Table 4.5 and depicted in Figure 4.12(a). The coils are color-coded in orange, and the cores in blue. In this experiment, 3000-strand AWG-46 litz wires and 3C95 ferrite from Ferroxcube are used to build the coil structure, which are shown in Figure 4.12(b).

Table 4.5: Dimensional Parameters.

Parameters	Values
I core size	80 mm*32 mm*16 mm
Wing core size	80 mm*16 mm*16 mm
Number of turns in transmitter's coil L_t	20
Number of turns in receiver's coil L_r	16
Air Gap	21 mm
Wire diameter	4 mm

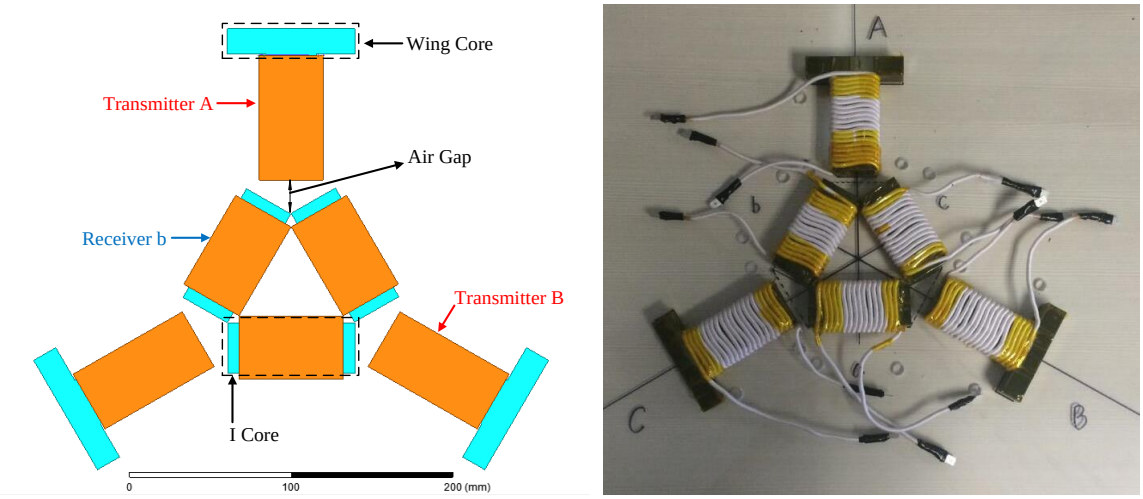

(a) (b)

Figure 4.12: (a) Simulation and (b) Experimental models of the proposed coil structure in Section 4.4.

A comparison of the simulated and measured results is drawn in Table 4.6, where L is the self-inductance and M is the mutual inductance. At the positions of subscripts, uppercase letters A, B, and C accordingly stand for transmitters A, B, and C while lowercase letters a, b, and c successively represent receivers a, b, and c. For example, L_{A} is the self-inductance of transmitter A and M_{Bc} is the mutual inductance between transmitter B and receiver c. As indicated by Table 4.6, the measured self-inductances L and mutual inductances M_{tr} between one transmitter and one of its adjacent receivers closely match the simulated ones, which are desired since the three-phase wireless charging system relies on M_{tr} to transfer power. The measured mutual inductances M_{tt} and M_{tr0} show good agreement with the simulations: the maximum difference among them is only 0.66 μH. However, the difference between the simulated and measured mutual inductances M_{rr} cannot be further ignored for an accurate experiment since its maximum value is approximately 1 μH. Moreover, it is difficult to fix this problem manually because the receivers are close to each other and parameters are correlated. A slight misalignment may lead to an obvious change in all self-inductances and mutual inductances. In order to minimize the effect, the arithmetic mean value of each two mutual inductances is selected as M_{rr} and applied in (4.3) of Section 4.3 to calculate the respective compensation capacitor values on receiver's side. For example, in calculation of the compensation capacitor C_{r} at receiver c, the arithmetic mean value of M_{ca} and M_{bc} are determined and substituted into M_{rr} in (4.3). The compensation capacitor values on transmitter's side are determined based on (4.5).

Table 4.6: Comparison between Simulated and Measured Results.

Para.	Sim.	Mea.	Para.	Sim.	Mea.	Para.	Sim.	Mea.	Para.	Sim.	Mea.
L_A	56.29 μH	56.87 μH	M_{Ab}	6.644 μH	6.815 μH	M_{AB}	2.333 μH	2.893 μH	M_{Aa}	0.0005 μH	0.005 μH
L_B	56.26 μH	56.96 μH	M_{Ac}	6.641 μH	6.685 μH	M_{BC}	2.334 μH	2.540 μH	M_{Bb}	0.001 μH	0.258 μH
L_C	56.30 μH	56.51 μH	M_{Ba}	6.640 μH	6.803 μH	M_{CA}	2.329 μH	2.663 μH	M_{Cc}	0.002 μH	0.510 μH
L_a	31.34 μH	31.64 μH	M_{Bc}	6.639 μH	6.610 μH	M_{ab}	4.433 μH	3.450 μH			
L_b	31.34 μH	31.70 μH	M_{Ca}	6.636 μH	6.610 μH	M_{bc}	4.434 μH	4.570 μH			
L_c	31.28 μH	31.40 μH	M_{Cb}	6.641 μH	6.663 μH	M_{ca}	4.426 μH	3.538 μH			

Simulations on air gap variation are conducted and the results are shown in Figure 4.13. The transmitter's and receiver's self-inductances L_t, L_r, and the mutual inductance M_{rr} are kept almost the same as air gap varies. Therefore, based on (4.3) to (4.5), the resonance remains. However, the mutual inductance M_{tr} decreases. Since power transfer relies on mutual inductance, the input voltage is required to increase with a larger air gap if the same output power is desired for dynamic charging applications.

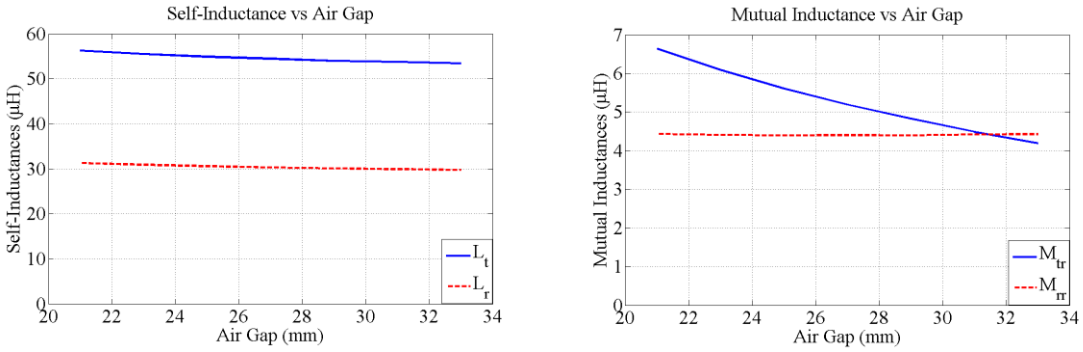

(a) (b)

Figure 4.13: (a) Self-inductances and (b) Mutual inductances with air gap variation.

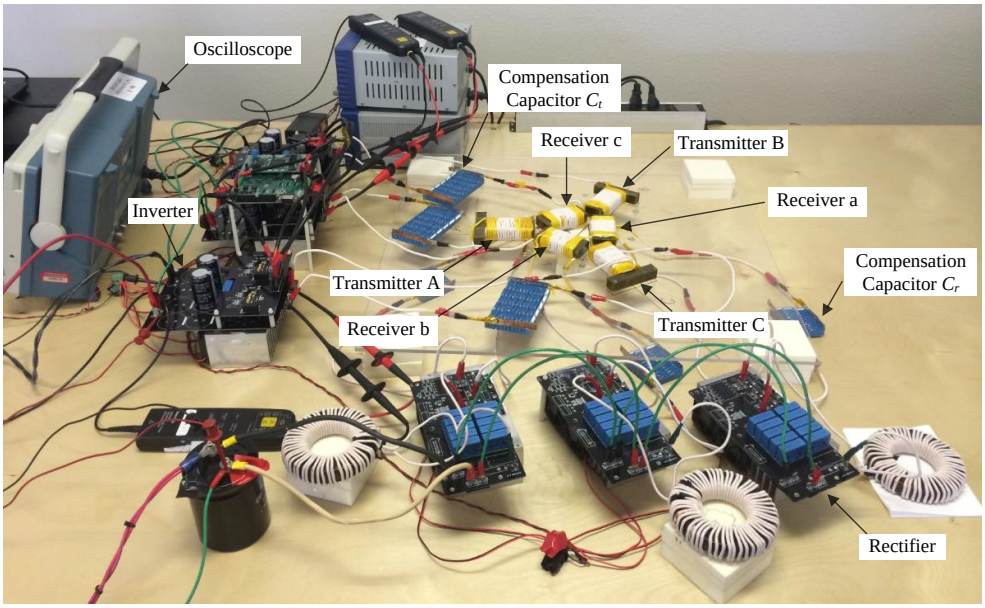

Figure 4.14: Experimental setup.

The three-phase wireless charging system is built as shown in Figure 4.14. Since the purpose of the experiment is to verify the proposed concept, three full-bridge inverters and three full-bridge rectifiers are selected for power conversion due to the convenience in lab. However, a three-phase inverter and a three-phase rectifier, which have competitive volumes with the single-phase ones, will be designed and chosen for practical applications. Experiments are conducted from DC power source to DC electronic load. Constant resistance (CR) mode and constant voltage (CV) mode of the DC electronic load are chosen to emulate a rechargeable battery. In this chapter, the selected constant resistances and voltage are 8 Ω, 12 Ω, 16 Ω, 20 Ω, and 110 V. Voltage and current waveforms when output power is 1.0 kW and resistance is 12 Ω are given in Figure 4.15. The input current i_{tA} in transmitter A lags its input voltage u_A by 18°, which ensures that the current is sufficient to charge the parasitic capacitors of the MOSFETs. Zero voltage switching is achieved and the switching losses and noises are reduced.

Experimental results on system power and efficiency in ambient air condition are shown in Figure 4.16. The three-phase wireless charging system is able to deliver 1.0 kW from

transmitters to receivers. As the resistance varies in Figure 4.16(a), the efficiency is maximized at 92.41%. Furthermore, it is demonstrated in Figure 4.16(b) that the system transfers 1.0 kW at DC-DC efficiency of 92.41% when the output voltage is constant at 110 V. Experiments under water and seawater conditions, in which multiple bottles of water or seawater are placed along the coils, are also separately conducted. The differences of the results among ambient air, water, and seawater conditions are very minor, which are shown in Figure 4.17. The proposed concept is thus verified by experiment.

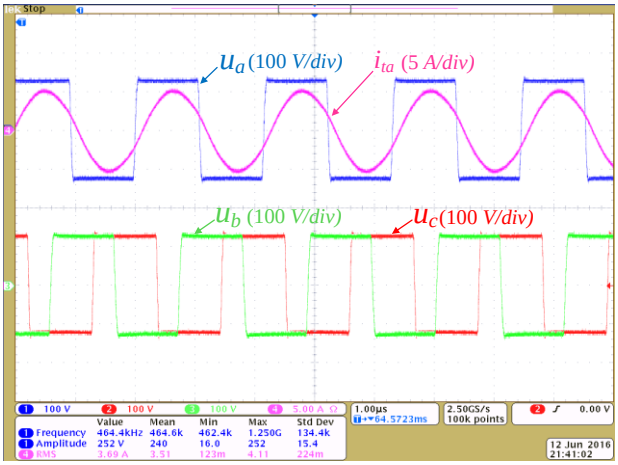

Figure 4.15: Waveforms at P_{out} = 1.0 kW and CR = 12 Ω.

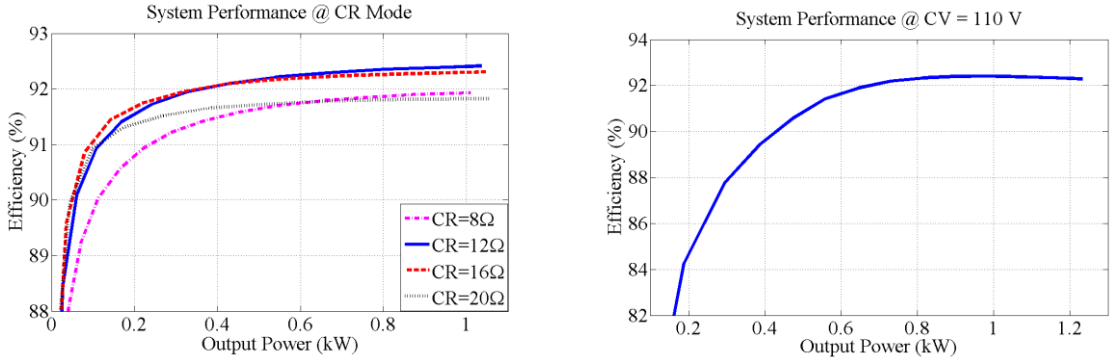

(a) (b)

Figure 4.16: System performance at (a) CR mode and (b) CV mode in ambient air condition.

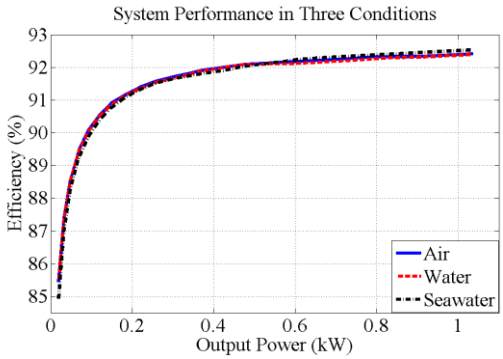

Figure 4.17: System performance in three conditions.

4.5 Conclusions

In this chapter, a three-phase wireless charging system for lightweight AUVs is proposed and analyzed. 3-D FEA simulations are performed to show the generated magnetic field by the proposed three-phase coil structure is concentrated in the coil structure and out of the AUV's hull, which has fewer adverse effects on the existing electronics devices in the AUV. Circuit analysis and compensation methods to achieve resonance are presented. A three-phase wireless charging system is designed and built for experiment. It is demonstrated that the system successfully delivers 1.0 kW with a DC-DC efficiency of 92.41% at 465 kHz, which verifies the proposed design.

This chapter is based on the following accepted paper. As the first author, I proposed the coil structure, performed finite element analysis, conducted the experiment, and drafted the paper. T. Kan, R. Mai, P. P. Mercier, and C. Mi, "Design and Analysis of a Three-Phase Wireless Charging System for Lightweight Autonomous Underwater Vehicles," . *IEEE Trans. Power Electron.*, 2017. [in press]

Chapter 5

Rotation-Resilient Coil Design for AUVs

5.1 Introduction

Chapter 4 proposed a wireless charging system with a hull-compatible three-phase coil structure, studied the magnetic field distributions, and demonstrated that the concentrated magnetic field had less impact on the instrumentation within the AUV. Moreover, a prototype was built and tested, demonstrating 1.0 kW of power transfer at a DC-DC efficiency of 92.41%. However, the system was very sensitive to rotational misalignment and thus would require an advanced mechanical positioning system, which would increase overall deployment cost. This chapter proposes a hull-compatible coil structure with a reversely wound receiver to improve the system performance during rotational misalignment between the transmitter and receiver coils. Finite element analysis is applied to verify the mutual inductance of the proposed coil structure is minimally affected during rotational misalignment. A prototype of the wireless charging system with the proposed coil structure is built and the experiment is conducted. It is demonstrated by the simulation and experimental results that the wireless charging system with the proposed coil structure has superior performance on rotational misalignment over the previous three-phase coil structure in Chapter 4.

5.2 Coil Design

A. Ideal Coil Design

The winding configuration and geometry of coils in a wireless power transfer system are of great importance, as they determine the power transfer performance and the magnetic field

pattern. In order to improve the system performance on rotational misalignment, a rotational-resilient ideal coil structure with a reversely wound receiver is proposed as shown in Figure 5.1(a). It consists of three identical transmitters and one receiver that is composed of two cores. The three transmitters are excited by three alternating currents with the same magnitude and frequency, but 120° out of phase. The receiver is divided into two parts connected in series: receiver part I and receiver part II. They have the same ferrite core and the same number of turns, but their winding directions are reversed from each other. The magnetic fluxes generated by the three transmitters couple with the receiver separately and return to the respective transmitters. As a result, there are three mutual inductances between each transmitter and the receiver. Since receiver parts I and II are reversely wound, the sum of the three mutual inductances is not zero. Furthermore, as will be shown shortly, it remains relatively constant when rotational misalignment occurs. Figure 5.1(b) gives the overview of the simulation model, in which the three transmitters with water-resistant design are placed in seawater and the receiver is fixed within the AUV's hull. The hull is made of fiberglass and has an outer diameter of 200 mm.

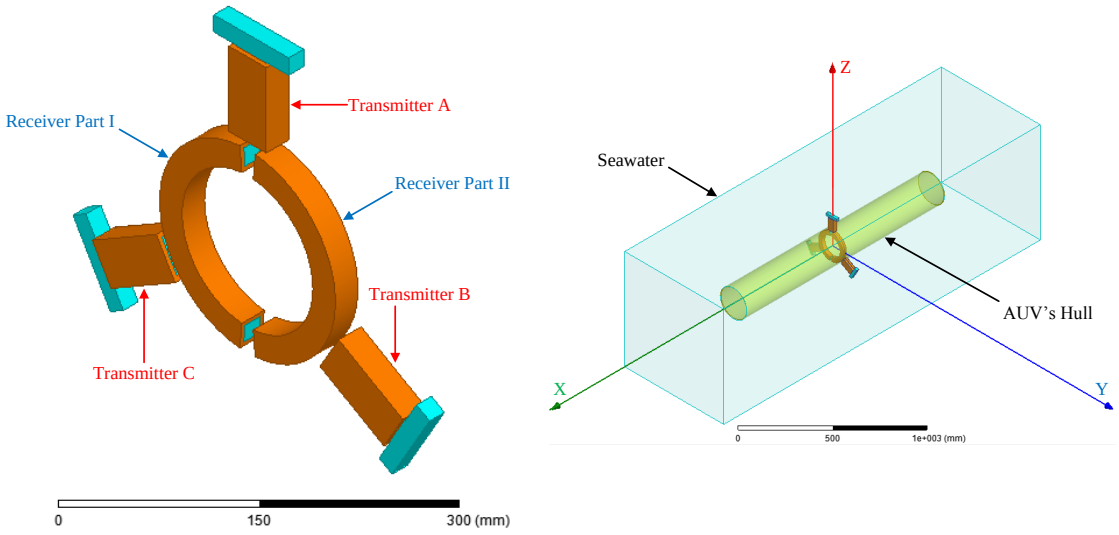

(a) (b)

Figure 5.1: Overview of (a) proposed ideal coil structure and (b) simulation model.

Simulation studies on rotational misalignment are conducted to verify the proposed ideal coil structure. Concurrently, a simulation model of the previous three-phase coil structure with three receivers in Chapter 4 is built and the system performances on the rotational misalignment are compared. In order to make a fair comparison, the seawater, the hull, and the transmitters are the same for both models. The magnitudes of the transmitter currents and the output powers are also the same. The only difference is in the receiver: the proposed ideal coil structure employs one receiver with two reversely wound parts, while the previous one uses three separate receivers. However, the number of turns of the receiver coil in the proposed ideal coil structure is the same as the total number of turns of the three receivers in the previous coil structure.

Power relies on the mutual inductance between the transmitter and the receiver to be transferred, thus, the mutual inductances are compared. For each receiver, there are three mutual inductances and the sum of the three mutual inductance vectors determines the power transferability. The equivalent mutual inductance M_{eq} is defined as the magnitude of the sum of the three mutual inductance vectors for each receiver and expressed as

$$M_{\text{eq}} = \left| M_{\text{AR}} \cdot e^{j\cdot 0} + M_{\text{BR}} \cdot e^{-j\cdot\frac{2\cdot\pi}{3}} + M_{\text{CR}} \cdot e^{-j\cdot\frac{4\cdot\pi}{3}} \right| \tag{5.1}$$

Where M_{AR} stands for the mutual inductance value between Transmitter A and the receiver, and likewise, M_{BR} and M_{CR}. For the proposed coil structure, the total mutual inductance, M_{tot}, is the equivalent mutual inductance, M_{eq}. For the previous coil structure with three receivers, the total mutual inductance, M_{tot}, is the sum of the three equivalent mutual inductances.

Rotational misalignment is depicted in Figure 5.2, in which the transmitters rotate counterclockwise while the respective positions of the three transmitters are fixed. For the proposed ideal coil structure, when the system is fully aligned, M_{AR} reaches its maximum while M_{BR} and M_{CR} are small. Power thus mainly relies on M_{AR} to be transferred. As the rotational

misalignment increases from 0° to 30°, M_{AR} and M_{BR} decrease while M_{CR} increases. Here, power mostly relies on M_{AR} and M_{CR} to be transferred. As the rotational misalignment continues increasing to 60°, M_{CR} goes up to the maximum and power primarily relies on M_{CR} to be transferred, which is the same with the fully aligned case. For the previous coil structure, the total mutual inductance decreases from the maximum to the minimum when the rotational misalignment increases from 0° to 60° and goes up to the maximum as the rotational misalignment increases to 120°.

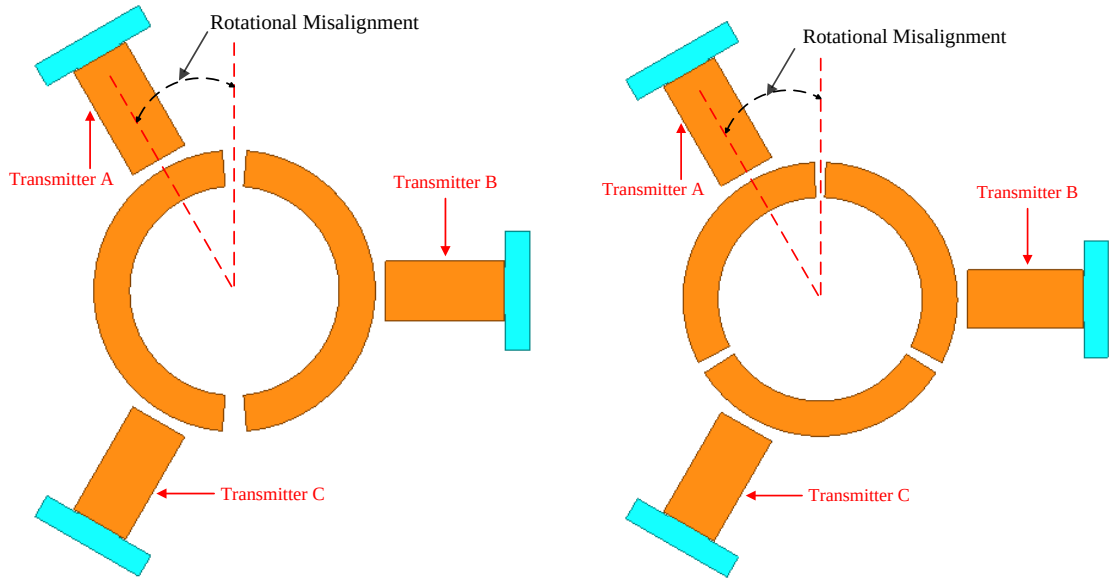

(a) (b)

Figure 5.2: Rotational misalignments in (a) proposed ideal coil structure and (b) previous coil structure.

Simulations with rotational misalignments are conducted and the total inductances are compared in Figure 5.3. In the fully aligned condition, the total mutual inductance of the proposed ideal coil structure is smaller than that of the previous coil structure. It is because power mainly relies on M_{AR} to be transferred while M_{BR} and M_{CR} are small. As the rotational misalignment increases from 0° to 120°, the total mutual inductance of the proposed coil structure is almost constant while that of the previous coil structure decreases from its maximum

to 25% of the maximum value, and increases back to its maximum. If the rated powers of the two coil structures are both 1.0 kW, the output power of the proposed ideal coil structure remains 1.0 kW while that of the previous coil structure changes from 1.0 kW to 250 Watts as the rotational misalignment varies from 0° to 120°.

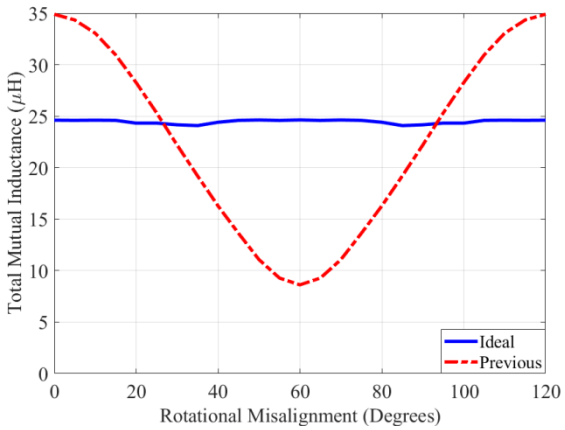

Figure 5.3: Total mutual inductances over rotational misalignment for proposed ideal coil structure and the previous coil structure from Chapter 4.

B. Segmented Coil Design

In practice, it is very difficult to find two large arc-shaped ferrite cores or their substitutions for experiments. Instead, the smaller pieces of arc-shaped ferrite cores are employed in this part to minimize the difference between simulation and experiment. As shown in Figure 5.4, each part of the receiver has three segmented coils. Within the same receiver part (i.e., part I or II), the three segmented coils are wound in the same direction and connected in series. Between different parts, the winding directions are reversed. The total number of turns of the receiver in the segmented coil design is the same with that in the ideal coil design.

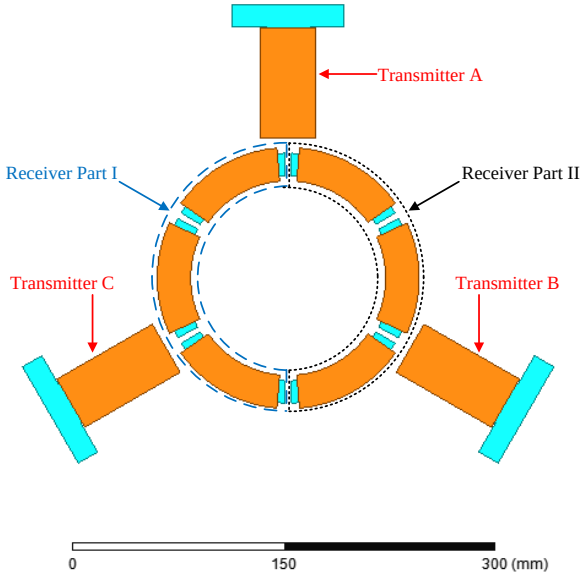

Figure 5.4: Proposed segmented coil design.

Simulations are performed on rotational misalignment and the total mutual inductance in the segmented coil design is smaller than that of the ideal coil structure due to the segmented ferrite cores with air gaps between them. As a result, the receiver's self-inductance decreases and the coupling coefficients go down. However, the segmented coil structure still has superior performance over rotational misalignment since the largest variation is only 25%. Figure 5.5 compares the nominal value of the total mutual inductance in the proposed segmented coil structure with that in the previous coil structure over rotational misalignment. If both two coil structures are nominally designed to transfer 1.0 kW, the output power of the proposed segmented coil structures ranges from 750 Watts to 1.0 kW when the rotational misalignment occurs – i.e., an output power variation of only 250 Watts. This compares favorably to the previous segmented design proposed in Chapter 4, whose output power can go as low as 250 Watts, for a total power variation of 750 Watts.

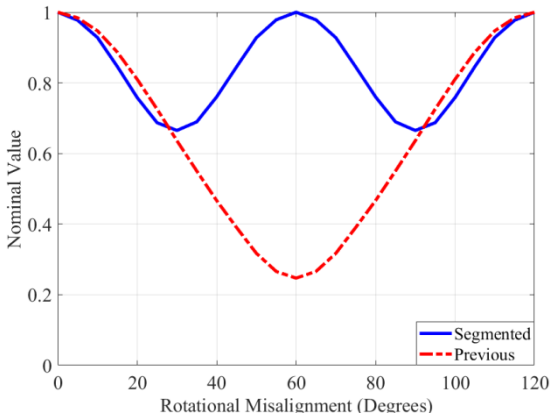

Figure 5.5: A comparison between the nominal value of the total mutual inductances in proposed segmented coil design and that in previous coil design over rotational misalignment.

C. Magnetic Field Distribution

The magnetic field distributions of the proposed coil structure in the fully aligned condition are plotted in Figure 5.6. The scales of the magnetic flux densities are the same with those in Chapter 4: 2.45×10^{-3} T at the maximum and 1×10^{-4} T at the minimum. The magnetic fields of the proposed coil structure are more divergent than those of the previous coil structure in Chapter 4, but still more convergent than the traditional coaxial coil structure. Therefore, the magnetic field distribution in the proposed coil structure is acceptable.

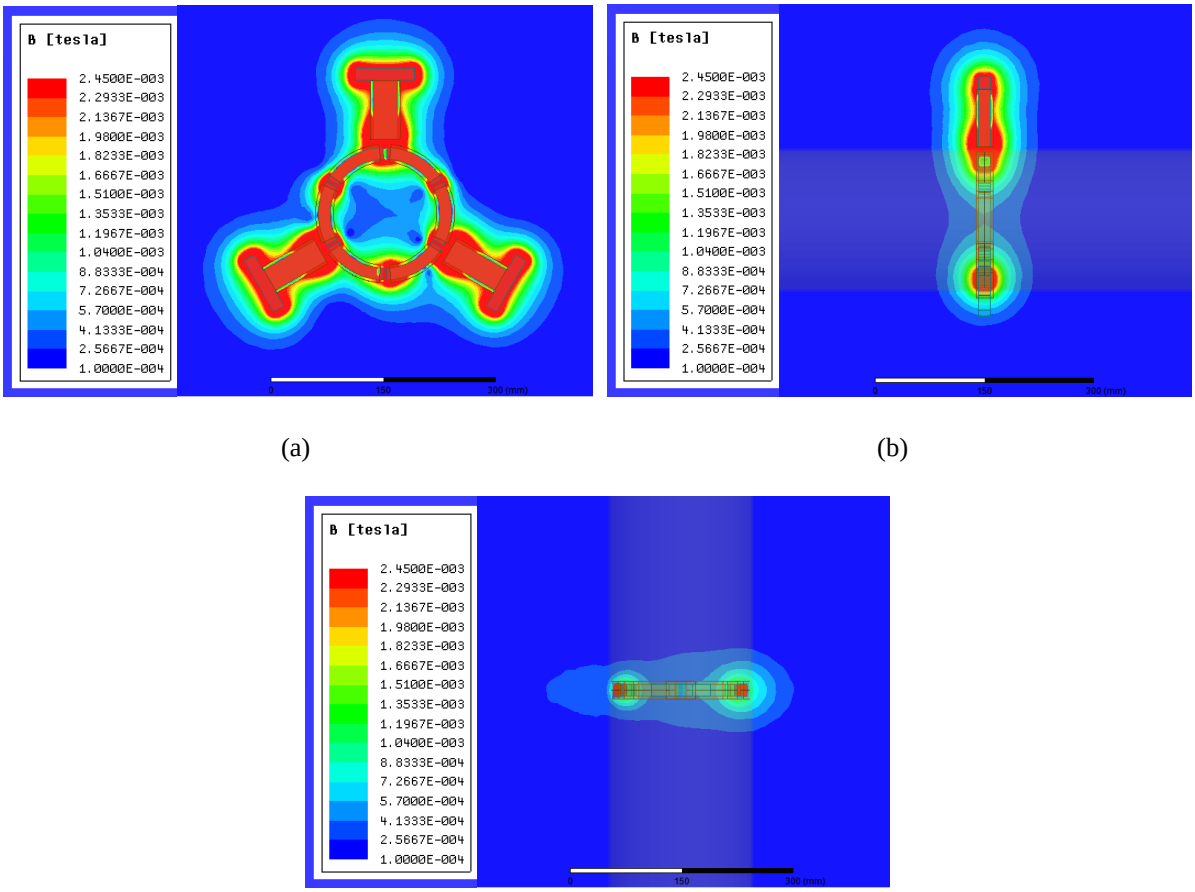

Figure 5.6: Magnetic field distributions in (a) YZ-plane, (b) ZX-Plane, and (c) XY-Plane.

Furthermore, a simulation model in ambient air condition, in which the seawater and the AUV's hull are omitted, is built and simulation studies on coil parameters and magnetic field distributions are conducted. The simulation results in ambient air condition and seawater condition are almost the same. It is because the relative permeability of seawater is very close to 1 and the seawater can be considered as air at the frequency of interest. The experimental results in Chapter 4 further demonstrate that there is almost no difference between seawater and ambient air conditions. Therefore, the following analysis and experiment will be conducted in the ambient air condition.

5.3 Circuit Analysis

Circuit analysis based on first harmonic approximation is performed from a DC power supply all the way to DC batteries on the AUV. Three full-bridge inverters are employed to generate three alternating voltages u_A, u_B, and u_C, with the same magnitude and frequency, but 120° out of phase. A full-bridge rectifier is used to convert from AC to DC. The DC batteries are considered as a load resistor R_L in the analysis since the voltage of the batteries is constant when they are charged at the desired power. Figure 5.7 shows the circuit diagram of the wireless charging system with the proposed coil structure and the equivalent series resistances of the components are ignored. On the transmitter's side, LCC compensation is selected to drive the transmitters, where the auxiliary coil resonates with the respective auxiliary capacitor, creating three currents with the same magnitude and frequency though 120° out of phase. On the receiver's side, LCC compensation is also chosen to achieve constant current charging, which is desired for charging batteries [52]-[53]. The resistor R_{eq} is the equivalent resistor of R_L.

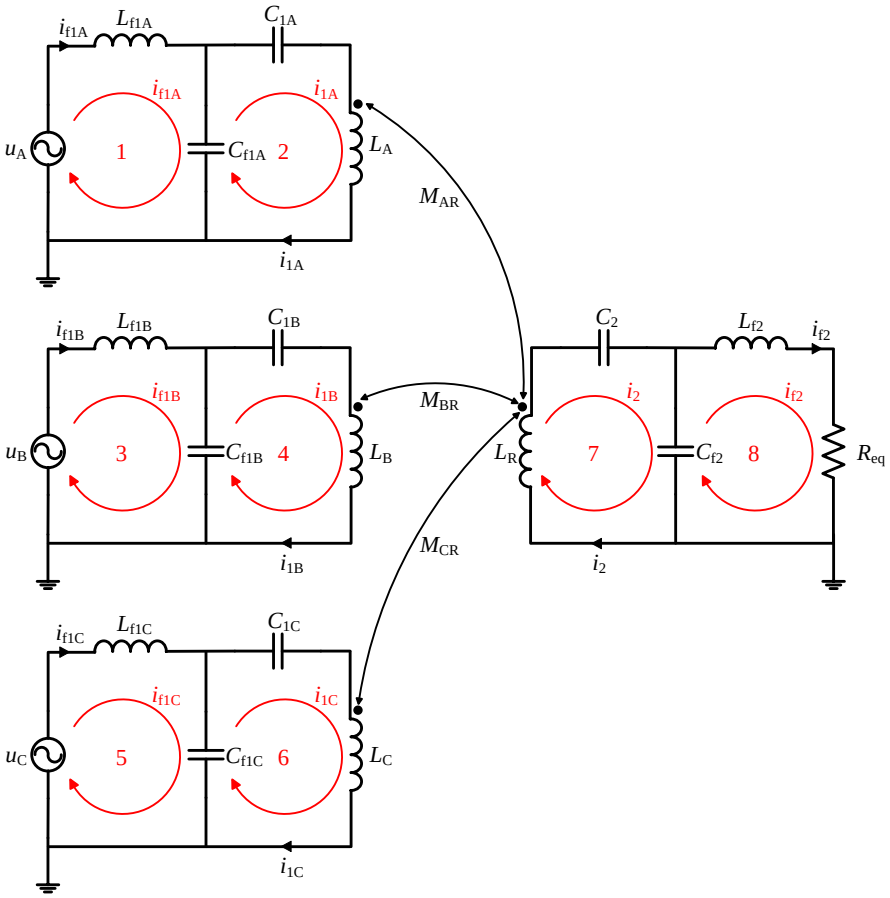

Figure 5.7: Circuit Diagram.

In Phase A, the auxiliary coil L_{f1A} is resonant with the auxiliary capacitor C_{f1A}, and the transmitter's self-inductance L_A is combined with the primary main capacitor C_{1A} to resonate with C_{f1A}, likewise for phase B and C. On receiver's side, the receiver's self-inductance L_R is cooperated with the secondary main capacitor C_2 to resonate with the secondary auxiliary capacitor C_{f2}, and the secondary auxiliary coil L_{f2} is resonant with C_{f2}. The resonant conditions can be expressed as

$$\begin{cases} j\omega L_{\mathrm{f1A}} + \dfrac{1}{j\omega C_{\mathrm{f1A}}} = 0 \\ j\omega L_{\mathrm{A}} + \dfrac{1}{j\omega C_{\mathrm{1A}}} + \dfrac{1}{j\omega C_{\mathrm{f1A}}} = 0 \\ j\omega L_{\mathrm{R}} + \dfrac{1}{j\omega C_{2}} + \dfrac{1}{j\omega C_{\mathrm{f}2}} = 0 \\ j\omega L_{\mathrm{f}2} + \dfrac{1}{j\omega C_{\mathrm{f}2}} = 0 \end{cases} \tag{5.2}$$

where ω is the angular frequency. As shown in Figure 5.7, the circuit is divided into eight meshes and mesh current method is applied to the circuit. In the resonant condition, the matrix is derived as

$$\begin{bmatrix} u_{\mathrm{A}} \\ 0 \\ u_{\mathrm{B}} \\ 0 \\ u_{\mathrm{C}} \\ 0 \\ 0 \\ 0 \end{bmatrix} = \begin{bmatrix} 0 & -\dfrac{1}{j\omega C_{\mathrm{f1A}}} & 0 & 0 & 0 & 0 & 0 & 0 \\ -\dfrac{1}{j\omega C_{\mathrm{f1A}}} & 0 & 0 & 0 & 0 & 0 & -j\omega M_{\mathrm{AR}} & 0 \\ 0 & 0 & 0 & -\dfrac{1}{j\omega C_{\mathrm{f1B}}} & 0 & 0 & 0 & 0 \\ 0 & 0 & -\dfrac{1}{j\omega C_{\mathrm{f1B}}} & 0 & 0 & 0 & -j\omega M_{\mathrm{BR}} & 0 \\ 0 & 0 & 0 & 0 & 0 & -\dfrac{1}{j\omega C_{\mathrm{f1C}}} & 0 & 0 \\ 0 & 0 & 0 & 0 & -\dfrac{1}{j\omega C_{\mathrm{f1C}}} & 0 & -j\omega M_{\mathrm{CR}} & 0 \\ 0 & -j\omega M_{\mathrm{AR}} & 0 & -j\omega M_{\mathrm{BR}} & 0 & -j\omega M_{\mathrm{CR}} & 0 & -\dfrac{1}{j\omega C_{2}} \\ 0 & 0 & 0 & 0 & 0 & 0 & -\dfrac{1}{j\omega C_{2}} & R_{\mathrm{eq}} \end{bmatrix} \cdot \begin{bmatrix} i_{\mathrm{f1A}} \\ i_{\mathrm{1A}} \\ i_{\mathrm{f1B}} \\ i_{\mathrm{1B}} \\ i_{\mathrm{f1C}} \\ i_{\mathrm{1C}} \\ i_{2} \\ i_{\mathrm{f2}} \end{bmatrix} \tag{5.3}$$

Three alternating voltages u_{A}, u_{B}, and u_{C} have the same magnitude of U. Moreover, in order to simplify the calculation, the primary auxiliary coils L_{f1A}, L_{f1B}, and L_{f1C} are assumed to be exactly the same and equal to L_{f1}. Similarly, the primary auxiliary capacitors have the same value of C_1. By solving (5.3), the currents are obtained as

$$\begin{bmatrix} i_{\mathrm{f1A}} \\ i_{\mathrm{1A}} \\ i_{\mathrm{f1B}} \\ i_{\mathrm{1B}} \\ i_{\mathrm{f1C}} \\ i_{\mathrm{1C}} \\ i_{2} \\ i_{\mathrm{f2}} \end{bmatrix} = \begin{bmatrix} \dfrac{R_{\mathrm{eq}} M_{\mathrm{AR}} U \cdot [(2M_{\mathrm{AR}} - M_{\mathrm{BR}} - M_{\mathrm{CR}}) + j \cdot \sqrt{3}(M_{\mathrm{BR}} - M_{\mathrm{CR}})]}{2\omega^2 L_{\mathrm{f1}}^2 L_{\mathrm{f2}}^2} \\ -j\dfrac{U}{\omega L_{\mathrm{f1}}} \\ \dfrac{R_{\mathrm{eq}} M_{\mathrm{BR}} U \cdot [(2M_{\mathrm{AR}} - M_{\mathrm{BR}} - M_{\mathrm{CR}}) + j \cdot \sqrt{3}(M_{\mathrm{BR}} - M_{\mathrm{CR}})]}{2\omega^2 L_{\mathrm{f1}}^2 L_{\mathrm{f2}}^2} \\ \dfrac{(1 + j \cdot \sqrt{3}) \cdot U}{2\omega L_{\mathrm{f1}}} \\ \dfrac{R_{\mathrm{eq}} M_{\mathrm{CR}} U \cdot [(2M_{\mathrm{AR}} - M_{\mathrm{BR}} - M_{\mathrm{CR}}) + j \cdot \sqrt{3}(M_{\mathrm{BR}} - M_{\mathrm{CR}})]}{2\omega^2 L_{\mathrm{f1}}^2 L_{\mathrm{f2}}^2} \\ \dfrac{(\sqrt{3} + j \cdot 1) \cdot U}{2\omega L_{\mathrm{f1}}} \\ \dfrac{R_{\mathrm{eq}} U \cdot [(2M_{\mathrm{AR}} - M_{\mathrm{BR}} - M_{\mathrm{CR}}) + j \cdot \sqrt{3}(M_{\mathrm{BR}} - M_{\mathrm{CR}})]}{2\omega^2 L_{f1} L_{f2}^2} \\ \dfrac{U \cdot [\sqrt{3}(M_{\mathrm{BR}} - M_{\mathrm{CR}}) - j \cdot (2M_{\mathrm{AR}} - M_{\mathrm{BR}} - M_{\mathrm{CR}})]}{2\omega L_{\mathrm{f1}} L_{\mathrm{f2}}} \end{bmatrix} \tag{5.4}$$

Therefore, the output power can be calculated as

$$P_{\mathrm{o}} = \left|i_{\mathrm{f2}}\right|^2 \cdot R_{\mathrm{eq}} = \frac{R_{\mathrm{eq}} U^2 \cdot \left(M_{\mathrm{AR}}^2 + M_{\mathrm{BR}}^2 + M_{\mathrm{CR}}^2 - M_{\mathrm{AR}} M_{\mathrm{BR}} - M_{\mathrm{BR}} M_{\mathrm{CR}} - M_{\mathrm{CR}} M_{\mathrm{AR}}\right)}{\omega^2 L_{\mathrm{f1}}^2 L_{\mathrm{f2}}^2} \tag{5.5}$$

If the power loss from the inverter and the rectifier is ignored and only the first harmonic is considered, according to [43], the output power from DC power supply to DC batteries is

$$P_{\mathrm{o}} = \frac{8U_{\mathrm{in}} U_{\mathrm{o}}}{\pi^2 \omega L_{\mathrm{f1}} L_{\mathrm{f2}}} \cdot \sqrt{M_{\mathrm{AR}}^2 + M_{\mathrm{BR}}^2 + M_{\mathrm{CR}}^2 - M_{\mathrm{AR}} M_{\mathrm{BR}} - M_{\mathrm{BR}} M_{\mathrm{CR}} - M_{\mathrm{CR}} M_{\mathrm{AR}}} \tag{5.6}$$

5.4 Experiment

Experiments are conducted to verify the proposed coil structure. Due to the difficulty of getting arc-shaped ferrite magnets at the frequency of interest, ferrite bars are employed for receiver's core in the coil prototype. The simulation model of the coil prototype is shown in Figure 5.8 and the simulations on rotational misalignment are performed in ambient air condition. Since 60° is the minimum period, the rotational misalignment changes from 0° to 60° in both simulation and experiment. A coil prototype is built based on the simulation model and the

mutual inductances between the three transmitters and the receiver are measured during rotational misalignment. The total mutual inductance is calculated and compared with that in the simulation. The results are summarized in Figure 5.9, which shows that measurements are well-matched to the simulations. As the rotational misalignment increases from 0° to 60°, the total mutual inductance decreases from its maximum value 10 μH to its minimum value 5 μH, and then increases back to 10 μH. In the prototype, the largest variation is approximately 50% and the variation can be minimized by using customized large or small segmented arc-shaped ferrite magnets in future work.

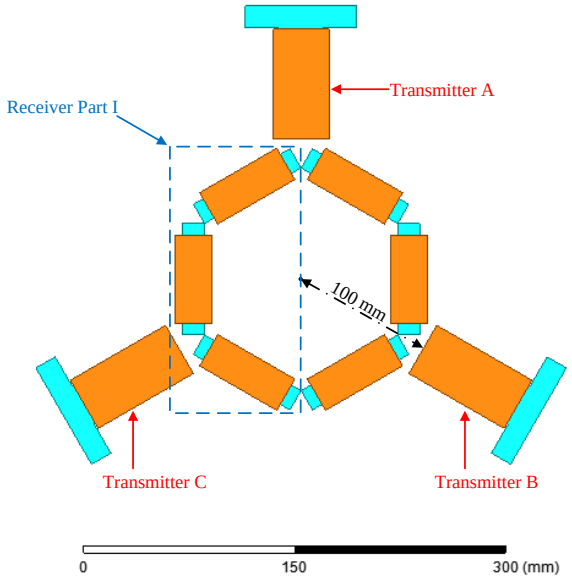

Figure 5.8: Simulation model of the coil prototype.

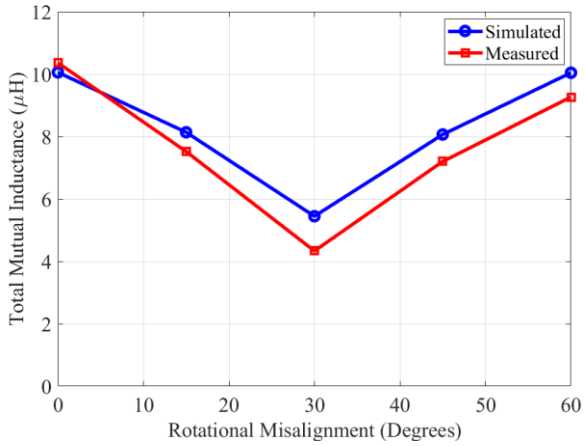

Figure 5.9: Simulated and measured results of the total mutual inductances.

According to the circuit analysis in Section 5.3, a three-phase wireless charging system using double-sided LCC compensation topology is built as shown in Figure 5.10. Five rotational misalignments are selected: 0°, 15°, 30°, 45°, and 60°. Both the input DC voltage and the DC voltage of the electronic load are fixed at 110V. The switching frequency is 472 kHz. The waveforms at 0° and 30° are shown in Figure 5.11 and the system performance on the output power and the DC-DC efficiency over different rotational misalignments are plotted in Figure 5.12. When the system is fully aligned, it delivers 745 Watts at a DC-DC efficiency of 86.19%. As rotational misalignment increases from 0° to 30°, the output power drops to 321 Watts since the total mutual inductance goes down to 4.33 μH. The efficiency decreases to 76.24%. This decrease occurs because the total mutual inductance decreases and more harmonics appear in the system, which can be seen from Figure 5.11(b). The experimental result in the worst rotational misalignment is still good by comparing to the previous coil structure in Chapter 4. If the previous coil structure is designed to transfer 745 Watts when it is fully aligned, it will only deliver 187 Watts at most based on the simulation results in Section 5.2. As the rotational misalignment continues increasing to 60°, both the output power and efficiency go up. As can be seen from the experimental results, the wireless charging system with the proposed coil structure

is more immune to rotational misalignment than the design in Chapter 4. Moreover, if arc-shaped ferrite magnets are customized in the future, system performance could be further improved.

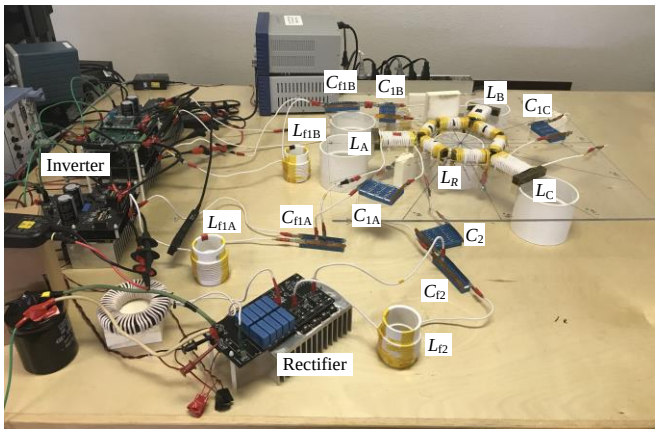

Figure 5.10: Experiment setup of a wireless charging system with proposed coil structure.

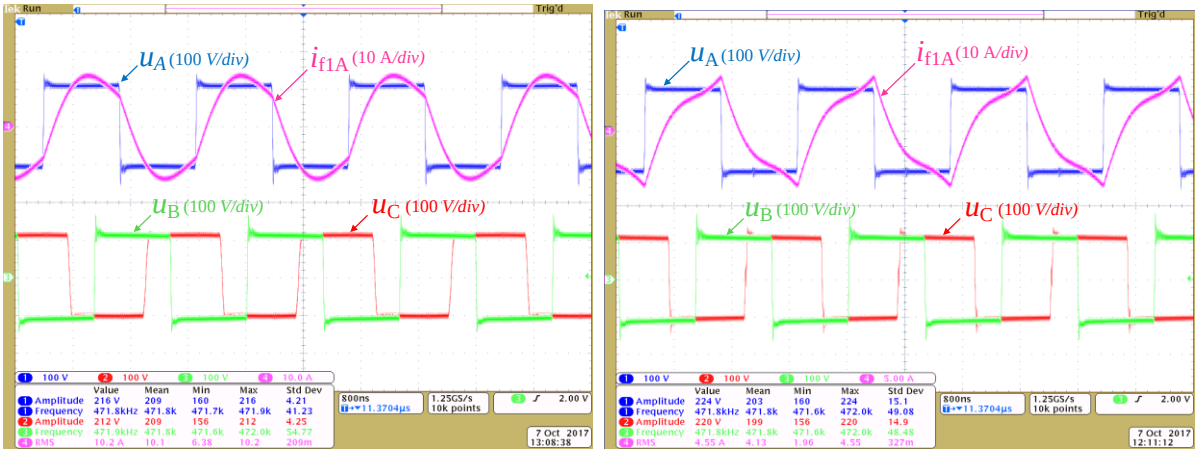

(a) (b)

Figure 5.11: Waveforms when (a) system is fully aligned and (b) rotational misalignment is 30°.

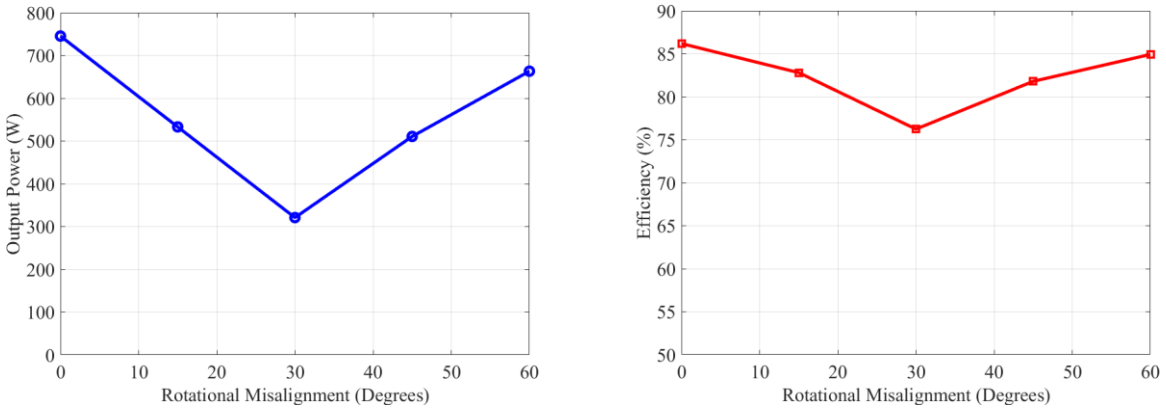

(a) (b)

Figure 5.12: Experimental results on (a) output power and (b) DC-DC efficiency over rotational misalignment.

5.5 Conclusions

A rotational-resilient wireless charging system with a two-part reversely wound receiver has been proposed in this chapter. By reverse winding, the system performance on rotational misalignment is significantly improved, especially when large arc-shaped ferrite cores are employed. Finite element analysis has been conducted to verify the proposed idea and the circuit analysis has been performed. A prototype of the wireless charging system with the proposed coil structure has been built and experimental results demonstrate that the output power on rotational misalignment is continuous with a maximum of 745 Watts and a minimum of 321 Watts. Furthermore, if customized arc-shape magnets are employed, the system output power can be even more constant during rotational misalignment.

This chapter is based on the following accepted paper. As the first author, I proposed the coil structure, performed finite element analysis, conducted the experiment, and drafted the paper. T. Kan, Y. Zhang, Z. Yan, P. P. Mercier, and C. Mi, "A Rotation-Resilient Wireless Charging System for Lightweight AUVs," *IEEE Trans. Veh. Technol.*, 2018. [accepted]

Chapter 6

Conclusions and Future Work

6.1 Conclusions

This dissertation introduces four coil designs based on the applications of wirelessly charging EVs and lightweight AUVs. The FEA tool ANSYS MAXWELL is employed to verify the designs. Concurrently, specific compensation methods are presented respectively to maximize power transfer and minimize the VA rating of the power source. In addition, detailed design procedures are given and prototypes are built to validate the proposed ideas.

For EV wireless charging systems using LCC compensation topology, this dissertation addresses two integration methods: one for bipolar coils and the other for unipolar coils. Also, a detailed design method on improving system efficiency is also developed. With the proposed integration methods, the systems are compact and highly efficient, which are verified by experimental results. Both systems can transfer 3.0 kW at a DC-DC efficiency of 95.5% at fully aligned condition. Furthermore, system performances on misaligned cases has been compared, demonstrating that the system with the integration method for unipolar coils has competitive performance in fully aligned and door-to-door misaligned conditions while superior performance on front-to-rear and vertical misalignments.

For lightweight AUV wireless charging systems, this dissertation proposes two hull-compatible coil designs: one is a three-phase coil structure and the other is a rotation-resilient coil structure. The three-phase coil structure consists of three transmitters and three receivers, constituting a three-phase magnetic field which is concentrated within the AUV or out of AUV's

hull. Thus, the instrumentations within the AUV are less adversely affected. A wireless charging prototype with the proposed three-phase coil structure is built to transfer 1.0 kW at 92.41% DC-DC efficiency. The rotation-resilient coil structure employs three transmitters and one two-part reversely wound receiver, significantly improving the system performance over rotational misalignment. FEA has been performed to demonstrate the total mutual inductance is relatively constant over rotational misalignment. A wireless charging prototype with ferrite bars is built to validate the output power is continuous with a maximum of 745 Watts and a minimum of 321 Watts when rotational misalignment occurs.

The main contributions of this dissertation are to propose four coil designs based on applications of wireless charging EVs and lightweight AUVs. For EV wireless charging systems with LCC compensation topology, the integrated coil design makes the systems more compact and increases the power densities; for lightweight AUV wireless charging systems, the three-phase coil design generates concentrated magnetic field and the instrumentations within the AUV are less interfered, and the rotation-resilient coil design significantly improve the system performance over rotational misalignments.

6.2 Future Work

The further work of EV wireless charging systems will focus on three aspects: (1) optimization of ferrite plates so that minimum ferrite bars are employed to deliver the same amount of power with competitive efficiency; (2) further study of the integrated compensated coils in order to improve the EMI performance; (3) designing a foreign object detection system by employing arrays of auxiliary coils and adjust the threshold values according to the magnetic field generated by main coils and compensated coils.

The future work of AUV wireless charging systems includes (1) optimization of circuit parameters in order to improve the system efficiency and (2) downsizing the power converters and minimizing the numbers of transistors used in system.

Bibliography

[1].H. Hertz, *Dictionary of Scientific Biography*. New York, NY, USA: Scribner, vol. VI, 1970, pp. 340 -349.

[2].N. Tesla, "Apparatus for transmitting electrical energy," U.S. Patent 1 119 732, Dec. 1914.

[3].W. C. Brown, "The history of power transmission by radio waves," *IEEE Trans. Microw. Theory Tech*., vol. MTT-32, no. 9, pp. 1230-1242, Sep. 1964.

[4].J. Garnica, R. A. Chinga, and J. Lin, "Wireless power transmission: from far field to near field," *Proceedings of the IEEE*., vol. 101, no. 6, pp. 1321-1331, Apr. 2013.

[5].A. Kurs *et al*. "Wireless power transfer via strongly coupled magnetic resonances," *Science*, vol. 317, no. 5834, pp. 83-86, Jul. 2007.

[6].R. Wu, W. Li, H. Luo, J. K. O. Sin, and C.P. Yue, "Design and characterization of wireless power links for brain-machine interface applications," *IEEE Trans. Power Electron*., vol. 29, no. 10, pp. 5462-5471, Jan. 2014.

[7].D. Ahn and P.P. Mercier, "Wireless power transfer with concurrent 200 kHz and 6.78 MHz operation in a single transmitter device," *IEEE Trans. Power Electron*., vol. PP, no. 99, pp. 1-13, Sep. 2015.

[8].M. Budhia, G. A. Covic, and J.T. Boys, "Design and optimization of circular magnetic structures for lumped inductive power transfer systems," *IEEE Trans. Power Electron*., vol. 26, no. 11, pp. 3096-3018, Apr. 2011.

[9].H. Takanashi, Y. Sato, Y. Kaneko, S. Abe, and T. Yasuda, "A large air gap 3 kW wireless power transfer system for electric vehicles, " in *Energy Conversion Congress and Exposition (ECCE), 2012 IEEE*, 2012, pp. 269-274.

[10].M. Budhia, J.T. Boys, G. A. Covic, and C. Huang, "Development of a single-sided flux magnetic coupler for electric vehicle IPT charging systems," *IEEE Trans. Ind. Electron*., vol. 60, no. 1, pp. 318-328, Sep. 2011.

[11].T. Nguyen, S. Li, W. Li, and C.C. Mi, "Feasibility study on bipolar pads for efficient wireless power chargers," in *Proc. IEEE Appl. Power Electron. Conf. Expo.*, 2014, pp. 1676-1682.

[12].Z. Pantic, S. Bai, and S. Lukic, "ZCS LCC-compensated resonant inverter for inductive-power-transfer application, " *IEEE Trans. Ind. Electron*., vol. 58, no. 8, pp. 3500-3510, Sep. 2010.

[13].S. Li, W. Li, J. Deng, T. D. Nguyen, and C.C. Mi, "A double-sided LCC compensation network and its tuning method for wireless power transfer," *IEEE Trans. Veh. Technol.*, vol. 64, no. 6, pp. 2261-2273, Aug. 2014.

[14].W. Li, H. Zhao, S. Li, J. Deng, T. Kan, and C. C. Mi, "Integrated LCC compensation topology for wireless charger in electric and plug-in electric vehicles ," *IEEE Trans. Ind. Electron.*, vol. 62, no. 7, pp. 4215-4225, Dec. 2014.

[15].J. Deng, W. Li, T. D. Nguyen, S. Li, and C. C. Mi, "Compact and efficient bipolar coupler for wireless power chargers: design and analysis," *IEEE Trans. Power Electron.*, vol. 30, no. 11, pp. 6130-6140, Mar. 2015.

[16].J. Deng, W. Li, S. Li, and C. C. Mi, "Magnetic integration of LCC compensated resonant converter for inductive power transfer applications, " in *Energy Conversion Congress and Exposition (ECCE), 2014 IEEE*, 2014, pp. 660-667.

[17].A. Pevere, R. Petrella, C. C. Mi, and S. Zhou, "Design of a high efficiency 22 kW wireless power transfer system for EVs fast contactless charging stations," in *Proc. IEEE Elect. Vehic. Conf., (IEVC)*, pp. 1-7, 2014.

[18].J. Lee and B. Han, "A bidirectional wireless power transfer EV charger using self-resonant PWM," *IEEE Trans. Power Electron.*, vol. 30, no. 4, pp. 1784-1787, Apr. 2015.

[19].C. Park, S. Lee, G. Cho, and C. T. Rim, "Innovative 5-m-off-distance inductive power transfer systems with optimally shaped dipole coils," *IEEE Trans. Power Electron.*, vol. 30, no. 2, pp. 817-827, Mar. 2014.

[20].F. Lu, H. Zhang, H. Hofmann, and C. C. Mi, "A high efficiency 3.3 kW loosely-coupled wireless power transfer system without magnetic material, " in *Energy Conversion Congress and Exposition (ECCE), 2015 IEEE*, 2015, pp. 2282-2286.

[21].S. Li, W and C. C. Mi, "Wireless power transfer for electric vehicle applications," *IEEE J. Emerg. Sel. Topics in Power Electron.*, vol. 3, no. 1, pp. 4-17, Mar. 2015.

[22].C. C. Mi, G. Buja, S. Y. Choi, C. T. Rim, "Modern advances in wireless power transfer systems for roadway powered electric vehicles", *IEEE Trans. Ind. Electron.*, vol. 63, no. 10, pp. 6533-6545, Oct. 2016.

[23].G. A. Covic, J. T. Boys, "Modern trends in inductive power transfer for transportation applications", *IEEE J. Emerg. Sel. Topics Power Electron.*, vol. 1, no. 1, pp. 28-41, May 2013.

[24].Z. Bi et al., "A review of wireless power transfer for electric vehicles: prospects to enhance sustainable mobility", *Appl. Energy*, vol. 179, pp. 413-425, Oct. 2016.

[25].S. Y. Choi, J. Huh, W. Y. Lee, J. G. Cho, C. T. Rim, "Asymmetric coil sets for wireless stationary EV chargers with large lateral tolerance by dominant field analysis", *IEEE Trans. Power Electron.*, vol. 29, no. 12, pp. 6406-6419, Dec. 2014.

[26].C. Park, S. Lee, S. Y. Jeong, G.-H. Cho, and C. T. Rim, "Uniform power I-type Inductive power transfer system with DQ-power supply rails for on-line electric vehicles," *IEEE Trans. Power Electron*., vol. 30, no. 11, pp. 6446–6455, Nov. 2015.

[27].W. Zhang, J. C. White, C. C. Mi, "Loosely coupled transformer structure and interoperability study for EV wireless charging systems", *IEEE Trans. Power Electron.*, vol. 30, no. 11, pp. 6356-6367, Nov. 2015.

[28].A. Khaligh, S. Dusmez, "Comprehensive topological analysis of conductive and inductive charging solutions for plug-in electric vehicles", *IEEE Trans. Veh. Technol.*, vol. 61, no. 11, pp. 3475-3489, Aug. 2012.

[29].Z. U. Zahid et al., "Modeling and control of series–series compensated inductive power transfer system", *IEEE J. Emerg. Sel. Topics Power Electron.*, vol. 3, no. 1, pp. 111-123, Mar. 2015.

[30].Y. Li, R. Mai, L. Lu, Z. He, "Active and reactive currents decomposition based control of angle and magnitude of current for a parallel multi-inverter IPT system", *IEEE Trans. Power Electron.*, vol. 32, no. 7, pp. 1602-1614, Feb. 2017.

[31].X. Zhang, T. Kan, C. You, and C. Mi, "Modeling and Analysis of AC Output Power Factor for Wireless Chargers in Electric Vehicles," *IEEE Trans. on Power Electron.*, vol. 32, no. 2, pp. 1481–1492, Feb. 2017.

[32].U. K. Madawala, M. Neath, and D. J. Thrimawithana, "A power-frequency controller for bidirectional inductive power transfer systems," *IEEE Trans. Ind. Electron*., vol. 60, no. 1, pp. 310-317, Jan. 2014.

[33].A. M. Bradley, M. D. Feezor, H. Singh, and F. Yates Sorrell, "Power systems for autonomous underwater vehicles," *IEEE J. Ocean. Eng.*, vol. 26, no. 4, pp. 526–538, 2001.

[34].M. D. Feezor, F. Y. Sorrell, and P. R. Blankinship, "An interface system for autonomous undersea vehicles," *IEEE J. Ocean. Eng.*, vol. 26, no. 4, pp. 522-525, 2001.

[35].T. McGinnis, C. P. Henze, and K. Conroy, "Inductive power system for autonomous underwater vehicles," in *OCEANS* , 2007, pp. 1-5, 29 Sep. - 4 Oct. 2007.

[36].Z. Li, D. Li, L. Lin, and Y. Chen, "Design considerations for electromagnetic couplers in contactless power transmission systems for deep-sea applications," *Journal of Zhejiang University SCIENCE C.*, vol. 11, no. 10, pp. 824-834, Sep. 2010.

[37].J. Shi, D. Li, and C. Yang, “Design and analysis of an underwater inductive coupling power transfer system for autonomous underwater vehicle docking applications, ” *Journal of Zhejiang University SCIENCE C*., vol. 15, no. 1, pp. 51-62, Jan. 2014.

[38].T. Kojiya, F. Sato, H. Matsuki, and T. Sato, “Automatic power supply system to underwater vehicles utilizing non-contacting technology,” in *Proc. Oceans MTTS/IEEE Techno-Ocean*, vol. 4. Nov. 2004, pp. 2341–2345.

[39].Z. Cheng, Y. Lei, K. Song, C. Zhu, "Design and loss analysis of loosely coupled transformer for an underwater high-power inductive power transfer system", *IEEE Trans. Magn.*, vol. 51, no. 7, pp. 1-10, Jul. 2015.

[40].Z. Yan, K. Zhang, H. Wen, and B. Song, “Research on characteristics of contactless power transmission device for autonomous underwater vehicle,” in Proc. OCEANS, 2016, pp. 1-5.

[41].A. Kamineni, G.A. Covic, and J. T. Boys, “Analysis of coplanar intermediate coil structures in inductive power transfer systems,” *IEEE Trans. Power Electron*., vol. 30, no. 11, pp. 6141-6154, Nov. 2015.

[42].W. Zhang and C. C. Mi, “Compensation topologies for high power wireless power transfer systems,” *IEEE Trans. Veh. Technol.*, vol. 65, no. 6, pp. 4768-4778, June. 2016.

[43].R. L. Steigerwald, “A comparison of half-bridge resonant converter topologies,” *IEEE Trans. Power Electron*., vol. 3, no. 2, pp. 174-182, Apr. 1998.

[44].F. Musavi, W. Eberle, and W. G. Dunford, “A high-performance single-phase bridgeless interleaved PFC converter for plug-in hybrid electric vehicle battery chargers,” *IEEE Trans. Ind. Appl.* vol. 47, no. 4, pp. 1833-1843, July-Aug. 2011..

[45].Q. Zhu, L. Wang, and C. Liao, “Compensate capacitor optimization for kilowatt-level magnetically resonant wireless charging system,” *IEEE Trans. Ind. Electron*., vol. 61, no. 12, pp. 6758-6768, Dec. 2014.

[46].Q. Zhu, Y. Guo, L. Wang, C. Liao, and F. Li, “Improving the misalignment tolerance of wireless charging system by optimizing the compensate capacitor,” *IEEE Trans. Ind. Electron.*, vol. 62, no. 8, pp. 4832-4836, Aug. 2015.

[47].Bloom MA, Niu G, Krishnamurthy M. Design considerations for wireless electric vehicle charging. In: 2013 IEEE transportation electrification conference and expo (ITEC). IEEE; 2013. p. 1-6.

[48].S. Y. R. Hui, W. Zhong, and C. K. Lee, “A critical review of recent progress in mid-range wireless power transfer,” *IEEE Trans. Power Electron*., vol. 29, no. 9, pp. 4500-4511, Sept. 2014.

[49].H. H. Wu, A. Gilchrist, K. D. Sealy, and D. Bronson, "A high efficiency 5 kW inductive charger for EVs using dual side control," *IEEE Trans. Ind. Informat*., vol. 8, no. 3, pp. 585-595, Aug. 2012.

[50].Budhia M, Covic G, Boys J. A new IPT magnetic coupler for electric vehicle charging systems. In: IECON 2010 - 36th annual conference on IEEE industrial electronics society. IEEE; 2010. p. 2487-92.

[51].C. Park, S. Lee, G. Cho G-H, and C. T. Rim "Innovative 5-m-off-distance inductive power transfer systems with optimally shaped dipole coils," *IEEE Trans. Power Electron*., vol. 30, no. 2, pp. 817-827, Feb. 2015.

[52].T. Kan, T. D. Nguyen, J. C. White, R. K. Malhan, and C. Mi, "A new integration method for an electric vehicle wireless charging system using LCC compensation Topology: Analysis and Design," *IEEE Trans. Power Electron*., vol. 32, no. 2, pp. 1638–1650, Feb. 2017.

[53].T. Kan, F. Lu, T. D. Nguyen, P.P. Mercier, and C. Mi, "Integrated coil design for EV wireless charging systems using LCC compensation topology," *IEEE Trans. Power Electron*., vol. PP, no. 99, pp. 1-11, Jan. 2018.

[54].C. Wang, G. A. Covic, and O. H. Stielau, "Power transfer capability and bifurcation phenomena of loosely coupled inductive power transfer systems," *IEEE Trans. Ind. Electron*., vol. 51, no. 1, pp. 148-157, Feb. 2004.

[55].J. L. Villa, J. Sallán, J. F. S. Osorio, and A. Llombart, "High-misalignment tolerant compensation topology for ICPT systems," *IEEE Trans. Ind. Electron*., vol. 59, no. 2, pp. 945-951, Feb. 2012.

[56].J. Sallán J, J. L. Villa, A. Llombart, and J. F. Sanz, " Optimal design of ICPT systems applied to electric vehicle battery charge," *IEEE Trans. Ind. Electron*., vol. 56, no. 6, pp. 2140-2149, June 2009.

[57].Z. U. Zahid et al., "Modeling and control of series-series compensated inductive power transfer system," *IEEE J. Emerg. Sel. Topics in Power Electron.*, vol. 3, no. 1, pp. 111-123, Mar. 2015.

[58].K. Colak, E. Asa, M. Bojarski, D. Czarkowski, and O.C. Onar, "A novel phase-shift control of semibridgeless active rectifier for wireless power transfer," *IEEE Trans. Power Electron*., vol. 30, no. 11, pp. 6288–6297, Nov. 2015.

[59].H. Hao, G. A. Covic, and J. T. Boys, "An approximate dynamic model of LCL-T-based inductive power transfer power supplies," *IEEE Trans. Power Electron*., vol. 29, no. 10, pp. 5554–5567, Oct. 2014.

[60].N. Hasan, H. Wang, T. Saha, and Z. Pantic, “A novel position sensorless power transfer control of lumped coil-based in-motion wireless power transfer systems,” In 2015 IEEE energy conversion congress and exposition (ECCE). IEEE; 2015. p. 586-93.

[61].B. X. Nguyen et al., “An efficiency optimization scheme for bidirectional inductive power transfer systems,” *IEEE Trans. Power Electron*., vol. 30, no. 11, pp. 6310–6319, Nov. 2015.

[62].B. Hesterman, "Analysis and modeling of magnetic coupling," *Denver Chapter, IEEE Power Electronics Society. Colorado,* 2007.

[63].M. Lin, D. Li, and C. Yang, “Design of an ICPT system for battery charging applied to underwater docking systems*,” Ocean Engineering*, vol. 145, no. 16, pp. 373-381, Nov. 2017.

[64].C. T. Ross, “A conceptual design of an underwater vehicle*,” Ocean Engineering*, vol. 33, no. 16, pp. 2087-2104, Nov. 2006.